Mapping Global Environmental Change Under Current Conditions and Projected Future Climate Scenarios with Machine Learning

A Dissertation Presented for the

Doctor of Philosophy

Degree

The University of Tennessee, Knoxville

Hannah Rubin

May 2025

Acknowledgements

First, I would like to thank my advisor, Dr. Joshua Fu, for his guidance and support. This work would not have been possible without him. His patience, commitment to quality, and work ethic have provided an outstanding example of how to conduct good scientific research.

I would like to thank my committee members, Dr. Forrest Hoffman, Dr. Peter Thornton, Dr. Edward Yu, and Dr. Jia Xing. Their comments and suggestions greatly improved the quality of this research.

I am also thankful for the other members of our research group, both past and present: Leyuan Zhang, Rong-You Chien, CP Kuo, Cheng-En Yang, Matthew Tipton, G. Andrew Ferrada, and Valeria Campos. I appreciate the insightful discussions and camaraderie.

Abstract

Anthropogenic climate change is the greatest threat our world faces. Because the impacts of climate change are linked to location, mapping is a meaningful way to convey results. I map 3 different phenomena and investigate methodological improvements and the associated uncertainty of acid deposition, heat waves, and soil organic carbon. My research on acid deposition updates the 2010 global budget for reactive nitrogen and sulfur components, improving the results of models from the second phase of the United Nation's Task Force on Hemispheric Transport of Air Pollution (HTAP-II). My analysis is a step towards the World Meteorological Organization's goal of global products for mapping harmful air pollution. Acid deposition is also relevant to the future climate; one potential response to climate change is stratospheric aerosol injection (SAI), where sulfur dioxide is injected into the stratosphere to block incoming solar radiation. I use outputs from the Geoengineering Model Intercomparison Project (GeoMIP) to track sulfur deposition from SAI through comparison with historical climate and two future Shared Socioeconomic Pathways (SSPs). My research emphasizes the lack of agreement between models and the importance of resolving these conflicts. The most common and recognizable climate change indicators are those related to temperature. However, most studies rely on a single dynamically downscaled model or an ensemble of statistically downscaled models. My work evaluates future heat wave risk in the US with an ensemble of dynamically downscaled models and an ensemble of statistically downscaled models. My results emphasize the importance of state-of-the-science modeling techniques for fine-resolution, domain-specific climate projections. In order to mitigate climate change, decarbonizing many industries will need to be a priority. A requirement of this work is an understanding of baseline soil organic carbon (SOC), before it is modified. My research focuses on SOC in the US from the 1980s to the present day. I incorporate satellite imagery, climatic and land use variables, and apply machine learning methods to produce high resolution, temporally and spatially continuous maps. Overall, my research aims to bring clarity to complex, multidimensional data through mapping techniques and thorough analysis.

Table of Contents

Chapter 1 Introduction 1
1.1 Global Environmental Change: Motivations for Research 1
Chapter 2 Global Nitrogen and Sulfur Mapping Using a Measurement-Model Fusion Approach 4
2.1 Nitrogen and Sulfur Deposition 4
2.2 Data Availability 6
2.3 Measurement Model Fusion Procedure 7
2.4 Results 10
2.5 Consistency of MMF deposition with global emission estimates. 15
2.6 Deposition over China. 17
2.7 Limitations of interpolation 17
2.8 Conclusions 20
Chapter 3 Improving Estimates of Wet Deposition in the U.S. with Measurement-Model Fusion and Machine Learning 21
3.1 Introduction 21
3.2 Methods 22
3.3 NO_3^- Deposition 24
3.4 NH_4^+ Deposition 24
3.5 Discussion 31
3.6 Conclusions 33
Chapter 4 Projected Global Sulfur Deposition with Climate Intervention 35
4.1 Climate Intervention 35
4.2 Methods and Data 37
4.3 Results 38
4.4 Model Discrepancies 38
4.5 SAI by Ecoregions 42
4.6 Discussion 46
4.7 Conclusions 53
Chapter 5 Downscaling Methods Accurately Predict Heat Wave Risk in a Changing Climate... 54
5.1 Introduction 54
5.2 Methods and Data 56

5.3 Comparison with Historical Models and Observations 58
5.4 Dynamical versus Statistical Downscaling 64
5.5 Discussion 68
5.6 Conclusions 71
Chapter 6 Mapping Long-Term Trends in Soil Organic Carbon with Machine Learning 73
6.1 Mapping Soil Organic Carbon 73
6.2 Methods and Data 73
6.3 Results 78
6.4 Discussion 87
6.5 Regional Differences 88
6.6 Land Use 89
6.7 Climate Change 92
6.8 Conclusions 93
Chapter 7 Conclusions 95
References 97
Appendix 131
Vita 154

List of Tables

Table 2.1 Sources of deposition observations 6
Table 2.2 2010 adjusted global wet and dry deposition in Tg N or Tg S. S2.1. 10
Table 3.1 Regional wet deposition averages in kg/ha/yr for 2010, as estimated by the STRF. ... 33
Table 4.1 Summary of selected CMIP6 model outputs in this work. 38
Table 6.1 Statistical description of model fit for the machine learning algorithms and the linear regression model. 79
Table 6.2 Modeled SOC values for the CONUS from recent literature. 86
Table S2.1. 2010 adjusted global wet and dry deposition in Tg N or Tg S. 131
Table S2.2. 2010 adjusted global wet and dry deposition in Tg N or Tg S. 132
Table S5.1. The six CMIP6 global climate models used in this work (Rastogi et al., 2022). 148
Table S5.2. The 8 models and observations compared in Figure 5.2. 149

List of Figures

Figure 2.1 A flowchart describes the MMF methodology implemented in this paper. 8
Figure 2.2 Total N and S deposition in 2010 using the MMF approach. 12
Figure 2.3 A comparison between HTAP II, MMF, and EMEP wet deposition fluxes in Europe results at EMEP observation sites. 13
Figure 2.4 The difference between MMF and MMM deposition with a 2.5-degree interpolation distance. 14
Figure 2.5 2010 Total N deposition in the continental USA. 14
Figure 2.6 Observed and modeled wet SO_4^{2-} deposition in the US in 2010. 16
Figure 3.1 The relationship between measured and predicted NO3- for the training (left, R2 = 0.89) and testing (right, R2: 0.89) datasets. 25
Figure 3.2 Monthly wet NO3- deposition over the CONUS in 2010, as modeled from HTAP and OMI satellite data in mg/ha. 26
Figure 3.3 The difference in monthly wet NO3- deposition over the CONUS in 2010 between the RF model estimated wet deposition and an estimate from an IDW map of NADP's NTN wet deposition measurements in mg/ha. 27
Figure 3.4 The relationship between measured and predicted NH4+ for the training (left, R2 = 0.92) and testing (right, R2: 0.92) datasets. 28
Figure 3.5 Monthly wet NH4+ deposition over the CONUS in 2010, as modeled from HTAP and OMI satellite data in mg/ha. 29
Figure 3.6 The difference in monthly wet NH4+ deposition over the CONUS in 2010 between the RF model estimated wet deposition and an estimate from the NADP's NTN wet deposition maps in mg/ha.. 30
Figure 4.1 Global dry S (both SO2 and SO_4^{2-}) deposition flux from historical estimates and three future climate scenario projections, SSP2-4.5, SSP5-8.5, and G6sulfur. 39
Figure 4.2 Projected A) annual and B) monthly precipitation and wet sulfur (SO_2 and SO_4^{2-}) deposition from UKESM1-0-LL, CESM2-WACCM, and CNRM-ESM2-1 during the historical time period (1980-2020) and under G6 Sulfur, SSP2-4.5, and SSP5-8.5 conditions (2020-2100). 40

Figure 4.3 The percent change from SSP2-4.5 to G6Sulfur for CESM2-WACCM and UKESM1-0-LL SO2 and SO_4^{2-} deposition by ecoregion, calculated as a difference in total deposition in Tg-S/yr.. 44
Figure 5.1 A comparison of historic heat waves during 1980–2019 to projected heat waves from 2020–2059. 59
Figure 5.2 Maximum daily temperature in the US, from 1980–2019. 62
Figure 5.3 Seasonal maximum temperature difference by decade. 65
Figure 5.4 Heatwave characteristics by percentile threshold and window. 66
Figure 5.5 Diurnal temperature range over time. 69
Figure 6.1 Farm Resource Regions, from the USDA. 79
Figure 6.2 A) Mean SOC (kg/m2) from 1990-2022 in the top 30 cm of soil. B) The slope of the trendline in SOC stocks from 1990 – 2022 by pixel. 80
Figure 6.3 Changes in annual SOC stocks by farm resource region. 82
Figure 6.4 SOC stocks by land cover category in the CONUS, averaged from 1990-2022. 84
Figure 6.5 Annual percentage of SOC stocks contained in land areas with maximum temperatures greater than the 95th percentile of the maximum temperature from 1990-2022 (red), with maximum temperatures less than the 95th percentile of the maximum temperature from 1990-2022 (pink), with annual precipitation greater than the 95th percentile of the annual precipitation from 1990-2022 (dark blue), and with annual precipitation less than the 95th percentile of the annual precipitation from 1990-2022 (light blue). 85
Figure S2.1 A world map showing the regions used to calculate the totals presented in Table 2.1 131
Figure S2.2. Observed and modeled wet NH4+ deposition in the US in 2010. 133
Figure S2.3. Observed and modeled wet NO3- deposition in the US in 2010. 133
Figure S2.4. The difference between MMF and MMM deposition with a 1-degree interpolation distance.. 134
Figure S2.5. The difference between MMF and MMM deposition with a 5-degree interpolation distance. 134
Figure S2.6. The difference between aggregated PRISM precipitation (1.9x1.9 degree) and modeled CAM-chem precipitation (1.9x1.9 degree) over the US in 2010. 135

Figure S2.7. Modeled wet NO_3 deposition in January 2010 from the STRF model…………………..135
Figure S4.1. The trajectory of the G6Sulfur scenario. Copied from GeoMIP at Rutgers University 136
Figure S4.2. Historical and projected A) G6Sulfur, B) SSP2-4.5, and C) SSP5-8.5 dry SO2 and SO42- deposition flux. 137
Figure S4.3. Precipitation flux from G6Sulfur GCM projections. 139
Figure S4.4. Projected total S deposition (wet SO2, wet SO42-, dry SO2, dry SO42-) from each G6Sulfur model averaged over 20-year slices. 139
Figure S4.5. The percent change from SSP5-8.5 to G6Sulfur for CESM2-WACCM and UKESM1-0-LL SO2 and SO42- deposition by ecoregion, calculated as a difference in total deposition in Tg-S/yr. 140
Figure S4.6. Percent of total land area by ecoregion for CESM2-WACCM............................. 141
Figure S4.7 Ecoregion 3 (deciduous needleleaf forests) in orange and 8 in pink (woody savannas) according to the A) CESM-WACCM and B) UKESM1-0-LL IGBP ecoregion maps. 142
Figure S4.8 The difference in precipitation flux from 2020-2040 to 2080-2100 under G6 Sulfur according to the A) CESM-WACCM and B) UKESM1-0-LL IGBP models. 143
Figure S4.9. The difference in precipitation flux from 2020-2040 to 2080-2100 under G6 Sulfur according to the CESM-WACCM and UKESM1-0-LL models by IGBP ecoregion. 144
Figure S5.1. Study Area: The Conterminous US (CONUS). 144
Figure S5.2. Predicted start day of the longest and hottest heat wave by threshold and window for each year in the US. 145
Figure S5.3. Average annual maximum temperature trends in the US. 146
Figure S5.4. Average annual minimum temperature trends in the US. 147
Figure S6.1 A) Locations of the training dataset (80%). B) Locations of the validation dataset (20%)... 150
Figure S6.2. Variable importance in the random forest model. 151
Figure S6.3. The fit of the random forest model... 151
Figure S6.4. The change in annual SOC (kg/m2) in CONUS regions experiencing a wildfire, one year before the fire, one year after the fire, the year of the fire, and 5 years after the fire. 152

Figure S6.5. The percentage of farmland in each USDA farm resource region under intensive tilling for all crops for 8 select years.. 153

Chapter 1 Introduction

1.1 Global Environmental Change: Motivations for Research

Global environmental change is the outcome of processes that operate on multiple spatial and temporal scales and have far-reaching consequences planetary, ecosystem, and human health (Vitousek, 1992). While such change has always been occurring because the Earth is not a static system, the specific phenomenon of anthropogenic climate change dates only to the industrialization of the mid-19th century when the burning and extraction of fossil fuels began on a large scale (Abram et al., 2016). Anthropogenic climate change is speeding up the rate of change of long-term processes (Lohmann et al., 2021) and having devastatingly fast impacts on the ecosystems and humans at risk from climate-related disasters.

Because the impacts of climate change are inextricably linked to location and environment, mapping is a particularly meaningful way to convey results and explore data. However, maps of non-static climate variables can often be misleading or incomplete due to the lack of ground-based observations in many regions, the difficulty of spatially interpolating in complex environments, and lack of uncertainty metrics. My research focuses on mapping techniques specifically for climate data – multidimensional, global time series of various environmental variables that are rapidly evolving due to the amount of carbon dioxide in the atmosphere. I map 3 different phenomena and investigate methodological improvements and the associated uncertainty of 1) acid deposition, 2) heat waves, and 3) soil organic carbon at varying time scales, all fundamentally related to global environmental change and climate impacts.

First, acid deposition. Carbon dioxide is not the only emission of concern related to anthropogenic climate change. While not a greenhouse gas, global reactive nitrogen (N) deposition has more than tripled since 1860 and is expected to remain high due to food production and fossil fuel consumption (Vishwakarma et al., 2023). And global sulfur emissions have been decreasing worldwide over the last 30 years, but many regions are still experiencing unhealthily high levels of deposition (X. Ge et al., 2023). My work updates the 2010 global deposition budget for reactive nitrogen and sulfur components with new regional wet deposition measurements from Asia, improving the ensemble results of eleven global chemistry transport models from the second phase of the United Nation’s Task Force on Hemispheric Transport of Air Pollution (HTAP-II). This study will demonstrate that a global measurement-model fusion approach can improve N and S deposition model estimates at a regional scale, with sufficient availability of observations. This analysis represents a step forward toward the World Meteorological Organization's goal of global fusion products for accurately mapping harmful air pollution deposition, eventually using machine learning and satellite imagery to fill gaps in regions that do not have observations.

Even with immediate global policy implementation, the impacts of climate change will continue to worsen over the next decades (IPCC, 2022). One potential response is stratospheric aerosol injection (SAI), where sulfur dioxide particles are released into the stratosphere to block incoming solar radiation and slow warming with the aim of giving the world more time to implement carbon reduction strategies (Crutzen, 2006). Sulfate aerosols have a lifetime of several years in the stratosphere but eventually they will be deposited back onto Earth's surface (Visioni et al., 2020). While sulfate is an important nutrient for many ecosystems, high concentrations can cause acidification, eutrophication, and a loss of biodiversity (Larssen & Carmichael, 2000). I will use model outputs from the Geoengineering Model Intercomparison Project (GeoMIP) to track the impacts of sulfur deposition from SAI to ecoregions through comparison with historical climate and two future Shared Socioeconomic Pathway (SSP) scenarios. My research emphasizes the lack of agreement between models and the importance of resolving these conflicts in order to improve our understanding of SAI impacts for future climate decision-making.

Secondly, heat waves. Perhaps the most common and recognizable climate change indicators are those related to temperature and the increase in daily averages over the last 50 years (Matthew Ballew et al., 2023; US EPA, 2015c). Heat waves are both common and deadly and as such measuring them provides an important metric to understanding climate change's impact on human and environmental health. The association between heat waves and mortality, morbidity, and ecosystem stress is well-established and as our world continues to warm, heat waves will become more frequent, more intense, and lengthier (IPCC, 2022). However, in order to project future heat wave trends and the human and environmental impacts, most studies rely on either coarse-resolution climate models, which are not sufficient for regional analysis, a single dynamically downscaled model, which is computationally intensive and potentially biased, or an ensemble of statistically downscaled models, which may not be as accurate for modeling future conditions. My work will evaluate projected future heat wave risk to the US on a regional scale with both an ensemble of 6 dynamically downscaled models and an ensemble of 6 statistically downscaled models. My results emphasize the need for urgent preparations for a hotter future climate and the importance of state-of-the-science modeling techniques for fine-resolution, domain-specific climate projections.

And finally, soil organic carbon. In order to mitigate climate change with or without geoengineering, decarbonizing many industries will need to be a priority. One such is aviation, which has contributed about 4% of the total global warming to date through a variety of mechanisms (Klöwer et al., 2021; D. S. Lee et al., 2021). In the US, the Federal Aviation Administration (FAA) is funding research into methods of making sustainable aviation fuel (SAF). Making SAF involves growing and managing biofuel crops on a large scale. In order to determine site suitability and management practices, a model, POLYSIS (https://bioenergymodels.nrel.gov/models/37/), is required to simulate the agriculture sector and project resource allocation. One of the important inputs is high quality maps of soil organic carbon (SOC), as a baseline for agricultural productivity. My research focuses on mapping SOC in the US from the 1980s to the present day and elucidating long term trends in SOC. I will incorporate satellite imagery as well as multiple climatic land use variables and apply machine learning methods to produce high resolution, temporally and spatially continuous maps of SOC dynamics in the US. Overall, my research aims to bring clarity to complex, multidimensional data through mapping techniques and thorough analysis.

Chapter 2 Global Nitrogen and Sulfur Mapping Using a Measurement-Model Fusion Approach

A version of this chapter has been published as:

Rubin, H. J., Fu, J. S., Dentener, F., Li, R., Huang, K., and Fu, H.: Global nitrogen and sulfur deposition mapping using a measurement–model fusion approach, Atmos. Chem. Phys., 23, 7091–7102, https://doi.org/10.5194/acp-23-7091-2023, 2023.

2.1 Nitrogen and Sulfur Deposition

Atmospheric nitrogen and sulfur deposition from human activities related to the use of fossils and land use have significant implications for ecosystem and human health. Elevated levels of nitrogen and sulfur can lead to eutrophication (Anderson et al., 2008; Heisler et al., 2008), changes in carbon sequestration (Kicklighter et al., 2019; de Vries et al., 2009; Zhu et al., 2020), loss of biodiversity (C. M. Clark et al., 2013; Dise & Stevens, 2005), and acidification (Bowman et al., 2008). While sulfur deposition is expected to decrease over the next 80 years (Lamarque et al., 2013), it will remain a serious hazard in many emerging economies. For instance, sulfur deposition in East Asia peaked in 2006 (Lu et al., 2010) but is still high enough to be concerning, especially in natural and semi-natural regions (Doney et al., 2007; X. S. Luo et al., 2014). Oxidized nitrogen (NO_y) and reduced nitrogen (NH_x), together called reactive nitrogen (Nr), and oxidized sulfur (SO_x) deposition occur as wet and dry processes (Dentener et al., 2006). Wet deposition is measured at hundreds of locations in Europe, North America, and Asia, but dry deposition is harder to measure and is often instead derived from ambient concentrations and modeled deposition velocities (W. Xu et al., 2015). For example, dry deposition is inferred from continuous concentration measurements combined with modeled dry deposition velocities at a few locations in North America (US EPA, 2015a) and Asia (Asia Center for Air Pollution Research, 2021).

The United Nations Economic Commission for Europe's Task Force on Hemispheric Transport of Air Pollution (HTAP) is an international effort to improve the understanding of air pollution transport science with emissions models. The second phase of HTAP was launched in 2012. Tan et al. (2018) used the multi-model mean (MMM) of 11 HTAP II chemistry transport models to estimate the sulfur and nitrogen deposition budgets for 2010. Significant uncertainty remained due to a lack of station measurements, especially in East Asia, a large contributor to the overall budget. Tan et al. (2018) compared Acid Deposition Monitoring Network in East Asia (EANET) (Acid Deposition Monitoring Network in East Asia, 2021) measurements to the MMM output but there were very few measurements in East Asia and all were located along the southeastern coast. In contrast, the highest emissions and modeled deposition were inland and north, making it challenging to evaluate model performance.

Combining measurements and model estimates in a “measurement-model fusion” (MMF) approach has the advantage of retaining the broad spatial coverage of models while accurately matching observations. Generally speaking, MMF takes model estimates of concentrations or fluxes for a region and modifies them based on in-situ point measurements to force the model towards the observed values (Labrador et al., 2020). One global MMF approach for wet deposition combined measurements with HTAP I ensemble model values for 2000-2002 (Vet et al., 2014) where model estimates filled empty grid cells lacking a 3-year observed mean. Another MMF approach in North America (Atmospheric Deposition Analysis Generated from optimal Interpolation from Observations, “ADAGIO”) used observed concentrations to adjust predicted concentrations from the Global Environmental Multiscale-Modelling Air Quality and Chemistry (GEM-MACH) model (D. Schwede et al., 2019). Recent work in the US (D. B. Schwede & Lear, 2014; Y. Zhang et al., 2019) incorporates Community Multiscale Air Quality (CMAQ) model output and precipitation data generated by the Parameter-elevation Regressions on Independent Slopes Model (PRISM, https://prism.oregonstate.edu/, Accessed: 10/01/22), as well as observations using inverse distance weighting to create total deposition (“TDep”, https://nadp.slh.wisc.edu/committees/tdep/#tdep-maps) maps that are publicly available.

More details of the MMF approach are described in Fu et al. (2022) as they lay out a roadmap for future work, following the World Meteorological Organization’s Global Atmosphere Watch Program (WMO GAW) and the intended role of the MMF Global Total Atmospheric Deposition (MMF-GTAD) project. This study updates Tan et al.’s (2018) global S and N deposition budgets using a variation of the TDep methodology (D. B. Schwede & Lear, 2014) to merge NH_x, NO_y, and SO_x modelled gridded deposition fluxes results with deposition fluxes derived from observations of NO_3^-, NH_4^+, and SO_4^{2-} in precipitation and precipitation amounts The main purpose of this study is to demonstrate the viability of a straightforward but globally applicable MMF approach, while remaining consistent with previous work that provided datasets for impact assessments for various communities. This approach is an important intermediate step towards the WMO’s goal of reliable deposition products to aid decision-making. I will update the 2010 deposition budgets using MMF to combine the broad spatial coverage of a model with accurate in-situ measurements.

2.2 Data Availability

All data are from 2010, reported monthly with sources summarized in **Table 2.1**. Wet deposition measurements (NO_3^-, NH_4^+, and SO_4^{2-}) from the US's National Trends Network (NTN) and Atmospheric Integrated Research Monitoring Network (AIRMoN) are available through the National Atmospheric Deposition Program (NADP (NADP, 2021), http://nadp.slh.wisc.edu/NTN/). Measurements were filtered for completeness and quality, following Schwede and Lear (2014). Sites without a full year of measurements or with quality tags indicating collection issues were not included, resulting in 247 observations in the US. Dry deposition generated values are available from the Clean Air Status and Trends Network (CASTNET(US EPA, 2015a) at 84 locations. CASTNET uses an inferential method to calculate dry deposition fluxes as a product of surface concentration and modeled dry deposition velocity. Nitrogen and sulfur wet deposition measurements and dry deposition estimates throughout Canada are recorded by the Canadian Air and Precipitation Monitoring Network (CAPMoN (Environment and Climate Change Canada, 2017) and are available through the National Atmospheric Chemistry (NAtChem) database (https://donnees.ec.gc.ca/data/air/monitor/).

Table 2.1 Sources of deposition observations

Name	Source	Number of Observation Sites	Region	Value
NTN, AIRMoN	NADP	247	USA	wet deposition
CASTNET	NADP	84	USA	dry deposition
CAPMoN	NAtChem	27	Canada	wet and dry deposition
EMEP	EMEP	86	Europe	wet deposition
China Scientific Study	Li et al. 2019	407	China	wet deposition
EANET	EANET	47	East Asia	wet and dry deposition
IDAF	INDAAF	1	Niger	wet deposition

Dry deposition estimates from CAPMoN are calculated by multiplying atmospheric concentration and deposition velocity. There were 27 sites with a full year of quality checked data for 2010.

The European Monitoring and Evaluation Programme (EMEP (EMEP, 2021; Tørseth et al., 2012), http://ebas-data.nilu.no/) provides records of precipitation chemistry (NO_3^-, NH_4^+, and SO_4^{2-}) and precipitation depths for Europe. There were 86 sites with a full year of quality checked data in 2010.

In China, a multi-year nationwide field study, including some of these NNDMN data, was compiled by Li et al. (2019). Daily NO_3^-, NH_4^+, and SO_4^{2-} site measurements (in mg/L) were averaged for 2010 for each of the 407 site locations with complete records by multiplying the concentration by the precipitation recorded at that same site (in mm) and then aggregating to produce annual precipitation-weighted deposition (Sirois, 1990). For a wider Asian region, EANET (Asia Center for Air Pollution Research, 2021, https://www.eanet.asia/) wet and dry deposition and precipitation data are available at 47 sites.

The International Global Atmospheric Chemistry (IGAC) Deposition of Biogeochemically Important Trace Species (DEBITS) Africa (IDAF) program (Adon et al., 2010; Galy-Lacaux et al., 2014) has NH_4^+ and NO_3^- precipitation concentrations on the International Network to Study Deposition and Atmospheric Chemistry in Africa (INDAAF (Institut National des Sciences de l'Univers, 2021)) website (https://indaaf.obs-mip.fr/) for one site in Niger. All measurements were converted to mg-N (or S) /m^2/yr.

2.3 Measurement Model Fusion Procedure

Global yearly wet and dry NO_3^-, NH_4^+, and SO_4^{2-} deposition observations (for wet deposition) or estimates derived from near-surface concentrations and modelled deposition velocities for dry deposition) were combined with the respective HTAP II model average grid cell estimates, using model output interpolated to common 1 degree x 1 degree (1º x 1º) grid cells (**Figure 2.1**). For example, wet NO_3^- deposition observations are combined with the wet NO_3^- modeled deposition in the nearest HTAP II MMM grid cell to the observation, where observations exist. Dry deposition values (NO_3^-, NH_4^+, and SO_4^{2-}) from CASTNET and an inverse-distance weighted 1º x 1º gridded dataset was created based on the distance from each observation to the center of the nearest HTAP II model grid cell. Inverse-distance weighting (IDW) was selected as the most

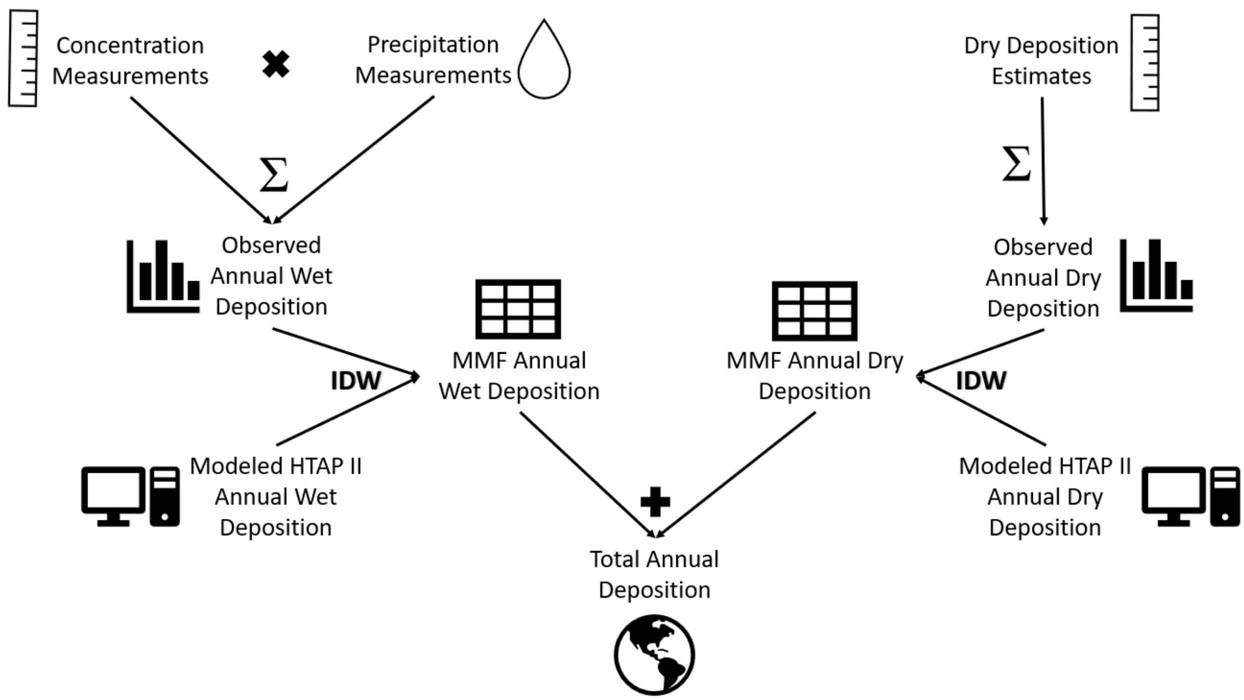

Figure 2.1 A flowchart describes the MMF methodology implemented in this paper.

straight forward to implement method to introduce MMF on a global scale while remaining consistent with previous work (D. B. Schwede & Lear, 2014).

The weighting function was calculated as

$$\left(1 - \frac{distance}{max\ distance}\right)^2 \tag{1}$$

following Schwede and Lear's (D. B. Schwede & Lear, 2014) approach for the TDep product, where "distance" is the distance between the site location and the center of the HTAP II model grid cell nearest to that sampling site location, within a maximum distance of 2.5º (approximately 280 km at middle latitudes). The choice of the maximum distance is a crucial parameter for the inverse distance weighting method in MMF. Prior analysis (e.g. Tan et al. 2018b) has shown that gaseous and particulate sulfur and nitrogen emissions can travel several hundreds of kilometers, before being deposited, although there is likely to be a large variation of transport distances due to regional differences in chemistry, meteorological conditions, transport patterns and removal processes. These processes interact with spatially heterogeneous emissions. Since there will not be a single distance that captures the heterogeneity of all processes at play, we present here a base case using a 2.5º interpolation distance, and two sensitivity cases reducing the distance to 1º and increasing it to 5º, respectively. The 5º distance can be seen as an upper limit for the distance where deposition observations can constrain deposition. The output values of the weighting function at each observation location are then multiplied by the observed deposition. For the center of every HTAP II model grid cell near that site, the modeled deposition is multiplied by 1 minus the value of the weighting function. Consequently, if there are no observations near the model grid cells, the cell value remains the same. The two grid values ([weighting function times observed deposition] and [1-weighting function times modeled deposition]) are added together to give the value of the MMF estimate. This has the effect of modifying the HTAP II grid values only in locations where there are observations within the maximum interpolation distance.

The MMF gridded surfaces were then summed by species along with the remaining unchanged HTAP II gridded surfaces that lacked in-situ measurements to create total N and S deposition gridded surfaces (e.g., the MMF wet and dry SO_4^{2-} gridded surfaces were added to the HTAP II wet and dry SO_2 gridded surfaces to get total S deposition). The MMF wet deposition surfaces include measurements from Europe, Asia, and North America, and the dry deposition MMF surfaces include estimates from the USA and Asia (see section 2)

2.4 Results

The total global NH_x deposition in 2010 increased from 54.0 Tg-N (from HTAP II models) to 54.9 Tg-N (**Table 2.2**). Combined with a NO_y deposition of 59.6 Tg-N (from a modeled HTAP II 59.3 Tg-N), the total global deposition is adjusted to 114.5Tg-N (from 113 Tg-N), an increase by 1 %. While the IDW tends to decrease the depositions over the continents, an increase is calculated over coastal regions and open oceans using the 2.5x2.5 maximum distance. Total S deposition is adjusted to 88.91 Tg-S (**Table 2.2**), an increase by 6.5 % from the HTAP II model prediction of 83.5 Tg-S (**Figure 2.2B**). Regional changes greater than or equal to 10% are bolded and italicized.

Tan et al. (2018) report that their MMM underestimates the high observations of total N deposition at some EMEP stations in Europe. We find that the 2.5º interpolation value for European wet N deposition (8.0 Tg) is increased by 12.5% relative to the MMM surface (7.1 Tg), although the distance to the observations remains high (**Figure 2.3**). **Figures 2.4, S2.4 and S2.5** show the difference between HTAP-II MMM and MMF nitrogen and sulfur deposition in North America, Europe, and Asia in mg/m^2 with different interpolation distances. As the interpolation distance increases, locations with a single measurement that is very different from the model will influence the surrounding grid cells to be higher than the model. This effect is in particular pronounced for sulfur deposition in Southeast Asia (**Figure 2.4 B3**) where the MMF procedure increases deposition by up to 250 mg/m^2 relative to the MMM values.

The spatial distribution is slightly different, with more deposition in coastal areas in the MMF estimate (**Table 2.2**). Tan et al. (2018) report that the HTAP II MMM overestimates NO_3^- wet deposition in North America, but underestimates NH_4^+ deposition. We find that the MMF interpolated deposition slightly improves these estimates, although the spatial distribution is very similar with the MMM (**Figures 2.2, 2.5**). The largest change for S deposition (comparing MMM and MMF) is in grid cells classified as ocean because of an increase in East and Southeast Asia deposition which mostly occurs in areas classified as ocean due to the small island size relative to the coarse spatial resolution of the models. We note that, ocean cells were classified as such if they were located further than 1º from the mainland; therefore, any islands smaller than 1º were counted as the ocean.

Table 2.2 2010 adjusted global wet and dry deposition in Tg N or Tg S. MMM indicates Tan et al.'s 2018 multi-model mean and MMF is this measurement-model fusion work with a 2.5º interpolation distance. The 1º and 5º interpolation distance results are shown in Tables S2.1 and S2.2. Coastal means deposition on sea within 1 degree of the coastline. RBU is an abbreviation for Russia, Belarus, and Ukraine. Open ocean does not include near-land "coastal" waters. The regions can be seen in the world map in Figure S2.1. Regional changes greater than or equal to 10% are bolded and italicized.

	Non-Coastal		Coastal		Non-Coastal		Coastal		Non-Coastal		Coastal	
	MMM	MMF	MMM	MMF	MMM	MMF	MMM	MMF	MMM	MMF	MMM	MMF
Region	**Total NH_x**				**Total NO_y**				**Total SO_x**			
North America	3.40	3.66	0.40	***0.31***	4.40	4.50	0.80	***0.94***	4.70	**5.67**	1.30	***1.69***
Europe	2.50	2.68	0.80	***1.14***	2.60	2.42	1.20	***1.75***	2.70	2.50	1.50	***3.18***
South Asia	8.60	8.60	1.00	1.00	3.60	3.60	0.70	0.70	3.70	3.70	1.00	1.00
East Asia	6.70	6.49	1.00	1.04	8.30	6.90	2.20	***2.45***	11.20	11.89	2.90	***4.10***
Southeast Asia	3.20	***2.22***	1.60	***2.12***	1.90	***1.60***	1.40	1.44	2.40	***0.81***	2.80	***0.56***
Australia	0.40	0.40	0.40	0.40	0.60	0.60	0.40	0.40	1.00	1.00	1.50	1.50
North Africa	0.70	0.70	0.20	0.20	1.40	1.40	0.40	0.40	1.00	1.00	0.50	0.50
Sub-Saharan Africa	3.40	3.40	0.40	0.40	4.70	4.70	0.60	0.60	2.70	2.70	0.70	0.70
Middle East	0.50	***0.38***	0.10	0.10	1.40	1.31	0.30	0.30	1.70	***3.18***	0.60	0.60
Central America	1.40	1.40	0.60	0.60	1.20	1.20	0.80	0.80	1.40	1.40	1.40	1.40
South America	3.80	3.80	0.30	0.30	3.40	3.40	0.30	0.30	2.40	2.40	0.60	0.60
RBU	1.80	***1.18***	0.30	***0.08***	2.40	***1.36***	0.50	0.47	3.60	***5.10***	0.90	***1.17***
Central Asia	0.50	***0.32***	0.00	0.00	0.60	0.55	0.00	0.00	1.20	***1.88***	0.10	0.10
Antarctica	0.10	0.10	0.00	0.00	0.10	0.10	0.00	0.00	1.40	1.40	0.00	0.00
Continental	37.00	35.33	7.10	7.69	36.70	33.64	9.70	10.55	41.00	44.63	15.60	***17.10***
Open Oceans	9.90	11.86			12.90	15.43			26.90	27.18		
Global	46.90	47.19	7.10	7.69	49.60	49.07	9.70	10.55	67.90	71.81	15.60	***17.10***

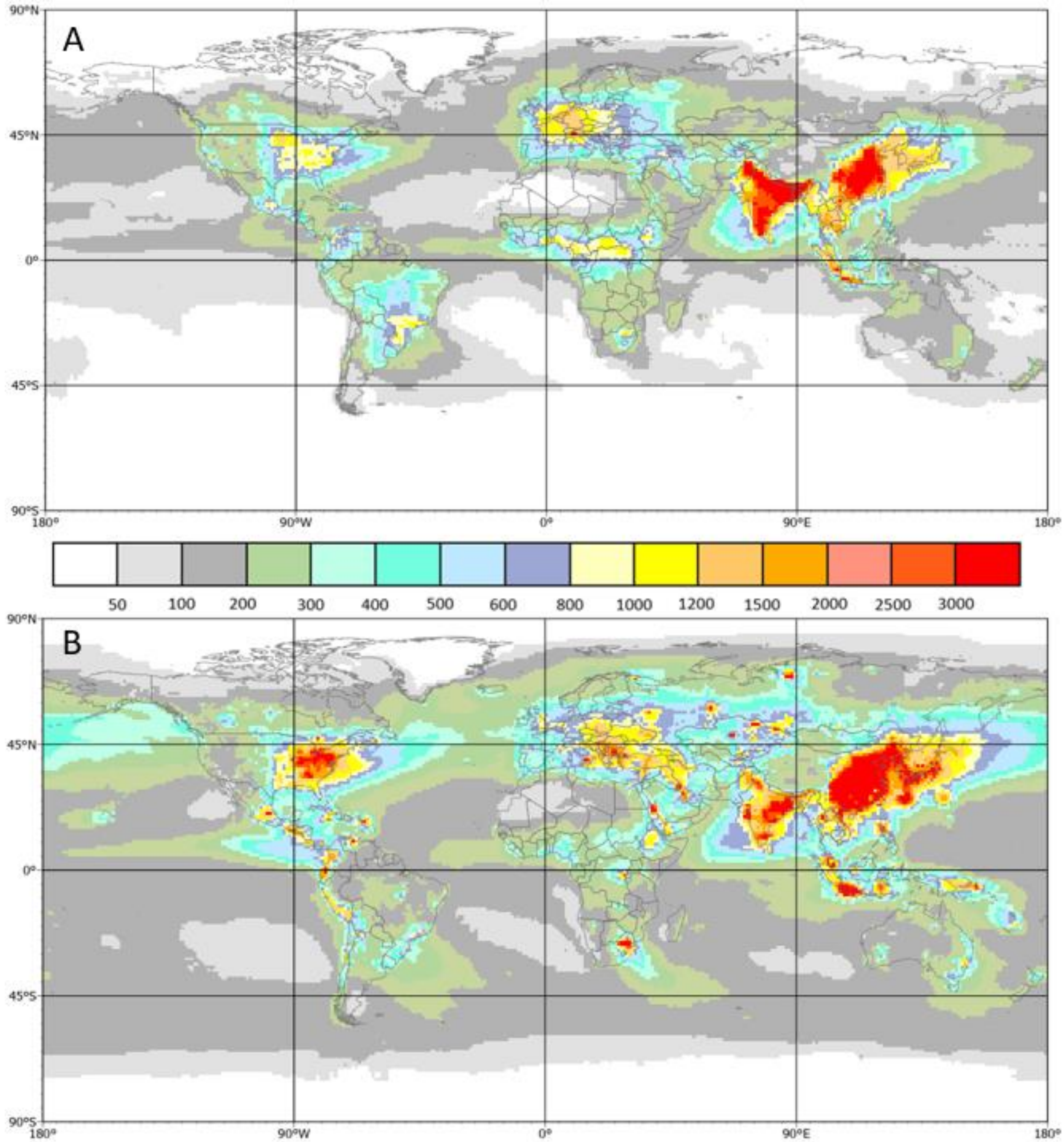

Figure 2.2 Total N and S deposition in 2010 using the MMF approach. A) Total annual N deposition (mg N/m2), the sum of wet and dry NO3- and NH4+ after applying the MMF approach, as well as HTAP II gridded surfaces of dry deposition of NH3, HNO3, and NO2 with no MMF

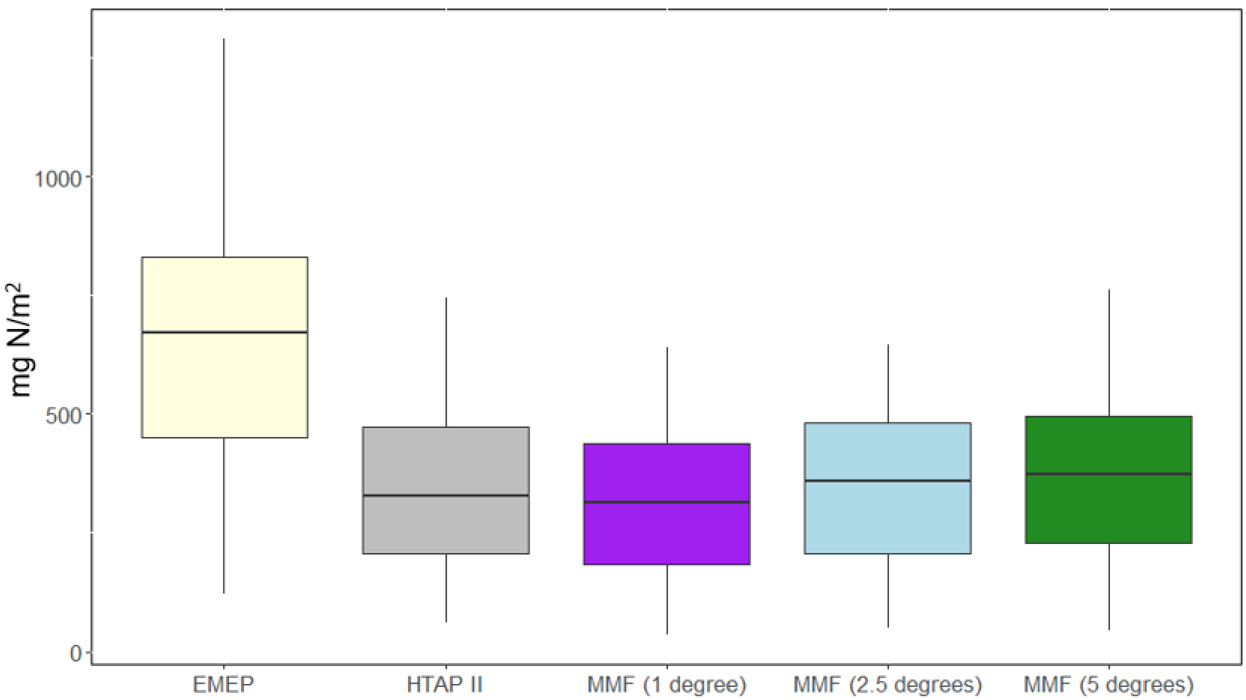

Figure 2.3 A comparison between HTAP II, MMF, and EMEP wet deposition fluxes in Europe results at EMEP observation sites. A boxplot shows the distribution of EMEP, HTAP II, and MMF modeled wet reactive nitrogen deposition (NH_x and NO_y) results at each EMEP observation sites. A boxplot shows the distribution of EMEP, HTAP II, and MMF modeled wet reactive nitrogen deposition (NH_x and NO_y) results at each EMEP observation location. Three different interpolation distances are compared using MMF, 1 degree, 2.5 degrees, and 5 degrees.

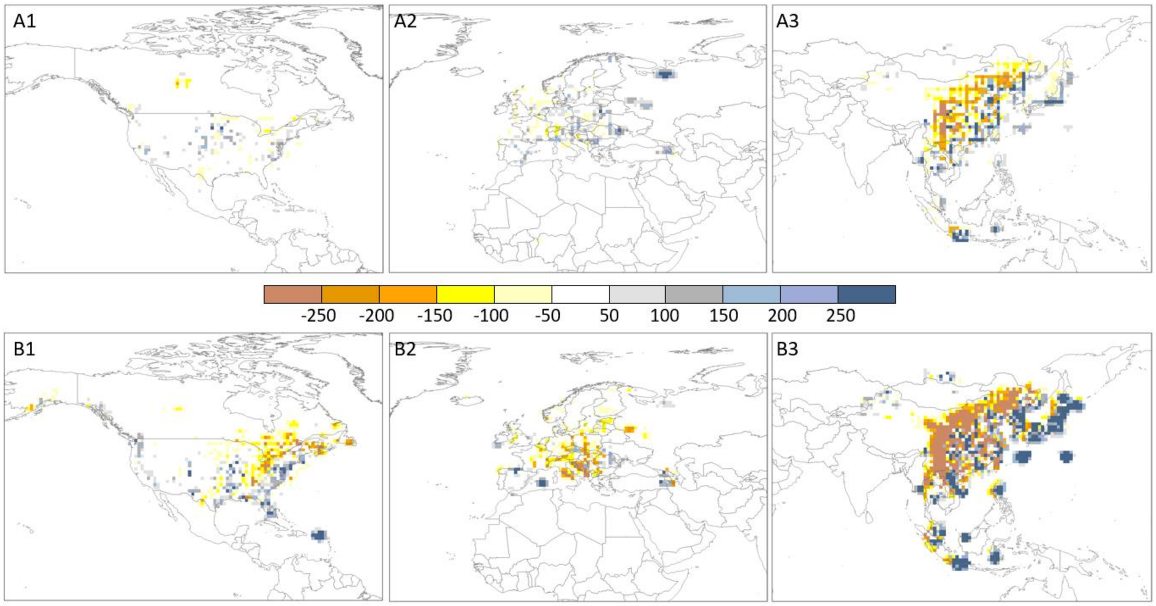

Figure 2.4 The difference between MMF and MMM deposition with a 2.5-degree interpolation distance. A) MMF minus MMM reactive nitrogen deposition in North America (A1) Europe (A2) and East Asia (A3) in mg N/m2. B) MMF minus MMM sulfate deposition in North America (B1) Europe (B2) and East Asia (B3) in mg S/m^2. Results for other interpolation distances are shown in Figures S11 and S12, respectively.

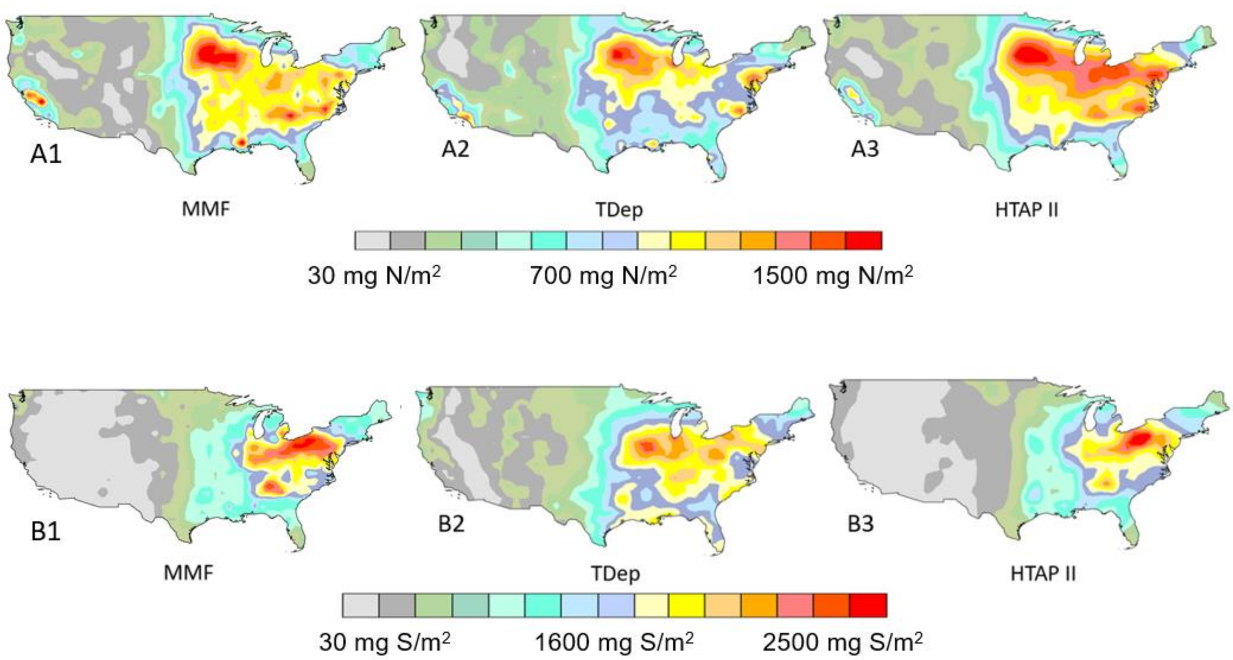

Figure 2.5 2010 Total N deposition in the continental USA A) Total N is modeled with 1) MMF (this work), 2) TDep annual map available from the NADP and 3) Tan et al.'s 2018 MMM. B) 2010 SO_x wet deposition in the US as modeled with 1) MMF (this work), 2) TDep annual map available from the NADP, and 3) Tan et al.'s 2018 multi-model mean HTAP II output.

There are spatial differences between an aggregated 1º x 1º version of the original TDep map of nitrogen deposition for the United States as available from the NADP (**Figure 2.5 A2**), the HTAP II (**Figure 2.5 A3**) deposition produced by Tan et al. (2018) corresponding to the same area, and the deposition map produced in this work (**Figure 2.5 A1**). A similar pattern is seen in the map of SO_4^{2-} deposition (**Figure 2.5 B1; 2.5 B3; 2.5 B3**). While the TDep maps have been aggregated to the 1x1 degree resolution of the HTAP fields, there is still different regional variation in the deposition patterns in the TDep maps than the HTAP II maps. In particular, TDep is capturing higher west coast values that HTAP II does not while showing lower values in the Midwest/New York/Pennsylvania region.

The R^2 value for the linear regression between MMF wet SO_4^{2-} and observed wet SO_4^{2-} in the US is 0.64 (**Figure 2.6**). The R^2 value for the linear regression between the HTAP II wet SO_4^{2-} and observed SO_4^{2-} is 0.0.60, and 0.89 for the linear regression between the TDep wet SO_4^{2-} and observed SO_4^{2-} (**Figure 2.6**). This means that TDep is better reproducing the NADP/NTN measurements and their spatial differences, whereas the MMF fields remain more similar to the HTAP II ensemble model output. The higher TDep R^2 value likely occurs because of the finer mesh (12 km) used in the TDep product, the closer proximity to individual stations as compared to HTAP II used in the MMF approach, and the ability of the regional model to capture gradients. In principle, emissions should be the same but in global models they are averaged over larger areas. All three datasets produce similar values to the measured wet SO_x deposition at the NADP/NTN sites (**Figure 2.6**). The NH_4 and NO_3 wet deposition values are shown in Figures S2.2 and S3, and have much lower correlations (for all three interpolation distances), with an R^2 of 0.1 for NO_3 and 0.53 for NH_4 at a 2.5º weighted distance.

2.5 Consistency of MMF deposition with global emission estimates.

Geddes et al. (2017) used satellite observations to report global NO_y emissions of 57.5 Tg-N/yr in 2010, similar to the 60.4 Tg-N emissions reported by HTAP II. This matches well with the total global MMF-derived NO_y deposition (58.1 Tg-N). HTAP II ammonia emissions were 59.3 Tg-N, slightly lower than the MMF NH_3 and NH_4+ deposition of 62.3 Tg-N. The total MMM sulfur emissions for 2010 were 90.7 Tg S, very similar to the MMF sulfur deposition of 88.9 Tg-N.

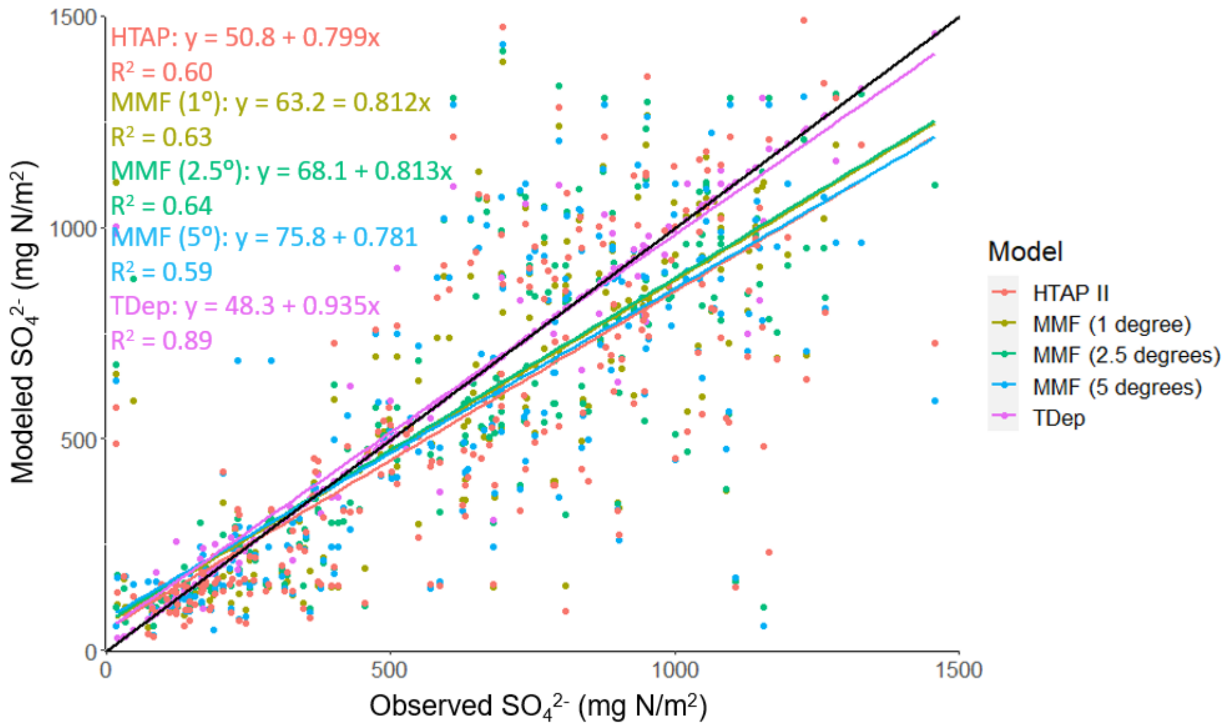

Figure 2.6 Observed and modeled wet SO_4^{2-} deposition in the US in 2010. Each NADP/NTN wet deposition measurement and the associated HTAP II, TDep, or MMF NH_x wet deposition modeled value, with all values shown together in A. The black line is the 1:1 line. Similar plots are shown in Figures S2.2 and S2.3 for wet NO_3 and wet NH_4.

2.6 Deposition over China.

A promising data set of wet deposition measurements (NO_3^-, NH_4^+, and SO_4^{2-}) in China is available through the National Nitrogen Deposition Monitoring Network (NNDMN (Wen Xu et al., 2019)). It is comparable to other regional measurements (Wen et al., 2020). However, these data only exist for a fraction of 2010 (from September onwards) for a few sites; rather than use partial data to represent an entire year, these sites were not included in this study. Research in China (L. Liu et al., 2020) analyzed the spatial pattern of N deposition by combining satellite - observations with NNDMN deposition measurements (Wen Xu et al., 2019); they found a 2012 average of 18.21 kg N ha^{-1} for China? Additional work combining the GEOS-Chem (http://acmg.seas.harvard.edu/geos/) model with satellite observations and surface measurements reports the average annual deposition from 2008-2012 as 16.4 Tg-N with 10.2 Tg-N from NH_x and 6.2 Tg-N from NO_y (Zhao et al., 2017). The averages reported by these studies are consistent with this study (16.9 kg ha^{-1} yr^{-1}) despite the difference in year and spatial resolution. The spatial pattern of N deposition in 2010 (**Figure 2.2A**) also remains similar to that of previous decades (Jia et al., 2014), with high deposition in eastern China and low deposition over the Tibetan Plateau. This pattern is confirmed in 2006 and 2013 (Qu et al., 2017).

2.7 Limitations of interpolation

As seen in Table 2.2, the largest difference between MMM and MMF is found in coastal regions and particularly the open ocean. While MMF does give improved deposition estimates by incorporating in-situ measurements, it is worth considering the scale of the model. Observations of deposition are probably not everywhere representative for a 1º or larger resolution and observations of precipitation may also not be homogenous in all directions at that scale, especially over heterogeneous terrain. So, for example, the coarse resolution of the model, even with added measurements is likely not accurately capturing gradients between coastal and inland deposition. While higher resolution precipitation values are available in some regions (e.g., PRISM in the US), there is still a dearth of both wet and dry deposition measurements. Even on the North American continental scale, Schwede et al. (2011) showed that partially overlapping dry deposition estimates from CASTNET (USA) and CAPMoN (Canada)can be very different, despite using similar methodologies. This adds uncertainty to the dry deposition data (though there are very few dry deposition estimates included in this study) and emphasizes the importance of understanding deposition velocity model methodology.

The differences between the TDep, MMM, and MMF gridded deposition (**Figure 2.5**) are clearly visible in the center of the US. While the general patterns of deposition are similar for the three products, the magnitude of deposition in the aggregated TDep dataset (1º x 1º) is higher in the eastern US and lower in the western US than either of the other two deposition fields. This difference is likely due to the precipitation dataset used to calculate wet deposition. The MMF deposition is based on the MMM dataset; therefore, both utilize the same precipitation dataset, from a combination of 11 global models. However, TDep wet deposition is produced by multiplying PRISM precipitation data and an interpolated gridded surface dataset of wet NH_4^+ concentrations. PRISM is a reanalysis product designed to interpolate precipitation in particularly complex landscapes using weather radar and rainfall gauge observations, though it is not identical to observations because it used long-term averages as predictor grids (M. Zhang et al., 2018). It captures much more localized variation in precipitation due to geographical variations which are not captured in the lower resolution global precipitation models used in the HTAP II MMM (J. Tan et al., 2018). To illustrate this, we compare PRISM to the available Community Atmosphere Model with Chemistry (https://www2.acom.ucar.edu/gcm/cam-chem, "CAM-Chem"), which was one of the models in the HTAP II ensemble. Subtracting the CAM-Chem precipitation output over the US from aggregated PRISM precipitation shows that CAM-Chem greatly underestimates precipitation volume in the US in 2010 (**Figure S2.6**). We note, however, that this comparison does not take differences in precipitation frequency between the model and observations into account. This matters because if the difference in precipitation volume comes from a few large magnitude storms, it will not influence the overall wet deposition values much. This is a good example of the differences that occur when comparing global and regional climate models and serves to emphasize the importance of resolving spatial and temporal scales. The total deposition within the US borders is similar for the MMF, HTAP II, and aggregated TDep gridded surfaces; however, the spatial distribution is different.

MMF and MMM deposition distributions are similar because MMF is based on HTAP II. Likewise, the MMF results are similar to the TDep values at observation locations because, despite the difference in precipitation, both utilize the same NADP/NTN measurements to constrain the models. The key difference between MMF, when compared to MMM, is that measurement locations are not centered in each 1º x 1º grid cell; therefore, the center of each grid cell (the value compared to the observation, by interpolation to the station location) will not exactly equal the measured deposition but will instead be equal to the measurements weighted proportionally to distance from the centroid. This means that the graphical comparison of Figure 2.6 is showing the actual measurement locations and 3 different model results with some meaningful influence from measurements that are nonetheless unique values, except in the very rare instance that the measurement corresponds exactly to the center of a grid cell. Figure 2.6 shows a stronger correlation for SO_4^{2-} than Figures S2.2 and S2.3 do for the nitrogen species. This could be related to the relatively shorter timescales of NO_y and NH_x in the atmosphere. The relatively coarse resolution of the global models cannot deal with these gradients, so the shorter timescales are reflected in the observations which are therefore less representative for the larger grid scales of the models.

TDep maps of North American nitrogen deposition created with Schwede and Lear's methodology (2014), using IDW, are widely in use and freely available from the NADP. The sensitivity analysis demonstrates that as the interpolation distance increases, the influence of the observations on the HTAP II grid increases, smoothing some of the artifacts that can occur using a small interpolation distance (**Figures 2.6, S2.2, S2.3**). In this respect it is worth mentioning that the original TDep dataset for North America used a maximum distance of 30 km plus half the cell size of PRISM (2.07 km). While it is not entirely clear how this distance was determined, operational factors such as the station density and the grid size of the regional model are likely important factors. In contrast, the maximum distances explored in this study are much larger (1º, 2.5º, 5º) and are more adapted to the grid size of the current generation of global atmospheric chemistry transport models, and considerations of transport distances of atmospheric components. From my analysis there is no obvious better weighting distance that improves the comparison with observations. An adaptive distance weighting that considers the expected gradients between the observation point and the remote model grid could be explored as a way forward.

However, there are strong limitations associated with using IDW (Sahu et al., 2010), and other interpolation methods such as kriging or geographically weighted regression could provide smoother surfaces with fewer artifacts. IDW makes the assumption that the observations are unbiased and so it forces an exact fit of the mapped surface to the observations. This is unlikely to be true due to measurement errors so IDW is instead imposing the biases and noise from the measurements onto the mapped output. Other approaches do not make the same assumption and can therefore avoid these artifacts. IDW is a fast and flexible interpolation method, but it does not minimize error and can produce inaccurate results in regions with sparse measurements and large sub-grid variability. This problem is relevant to much of the world. The lack of measurement sites globally is a hindrance that can be alleviated by including information obtained from satellite remote sensing (Walker et al., 2019). Future work should also investigate methods such as kriging or various machine learning techniques with spatial information to avoid these limitations.

These results from measurement-model fusion are important because previous methods on a global scale have relied primarily on models (J. Tan et al., 2018; Vet et al., 2014). They compare their results with measurements, of course, in order to demonstrate the model capabilities but they do not explicitly incorporate point measurements into the final product. My results serve to emphasize that global models are adequately simulating deposition (in terms of total deposition budgets) but that the regional discrepancies between models and measurements can still be quite large; and measurement-model fusion helps to ameliorate this without changing the fundamental model parameters and processes that actually capture the overall deposition reasonably well.

2.8 Conclusions

Sulfur and nitrogen deposition remain a serious concern for human and ecosystem health. We update the 2010 deposition budgets using measurement-model fusion to combine the broad spatial coverage of a model with accurate in-situ measurements. The total nitrogen deposition budget is recalculated to 114.50 Tg-N and the sulfur budget is recalculated to 88.91 Tg-N, representing about a 1% and 6.5% increase, respectively, from the modelled values. This work emphasizes the necessity of combining models with observations wherever possible, to better capture regional patterns and to inform policy and decision-making. Future work to improve measurement-model fusion should investigate more advanced MMF methods to avoid the limitations associated with IDW such as surface artifacts and high error in regions with sparse measurements. It could also incorporate satellite remote sensing derived concentrations to improve model estimates where in-situ measurements are not available, but a careful error analysis is needed to avoid spurious results.

Chapter 3 Improving Estimates of Wet Deposition in the U.S. with Measurement-Model Fusion and Machine Learning

3.1 Introduction

Atmospheric reactive nitrogen (N) deposition from human activities such as industry and agriculture have significant implications for ecosystem and human health (Bobbink et al., 2010). Elevated levels of nitrogen and sulfur deposition can lead to a range of negative consequences such as eutrophication (Anderson et al., 2008; Heisler et al., 2008), changes in carbon sequestration (Kicklighter et al., 2019; de Vries et al., 2009; Zhu et al., 2020), loss of biodiversity (C. M. Clark et al., 2013; Dise & Stevens, 2005), and soil acidification (Bowman et al., 2008). These impacts on human and ecosystem health are directly tied to many of the United Nations (UN)'s Sustainable Development Goals (SDGs)(Elder & Zusman, 2016; World Meteorological Organization, 2021): reaching zero hunger (SDG 1) by increasing production yields, reducing premature mortality from poor air quality (SDG 3), providing clean water by reducing pollutants (SDG 6), managing aquatic resources and reducing acidification (SDG 14), and preserving terrestrial biodiversity (SDG 15) (World Meteorological Organization, 2021). The World Meteorological Organization (WMO) aims to meet the United Nation's 2030 Agenda for Sustainable Development by coordinating global climate science initiatives. In order for the WMO and individual communities to make informed decisions regarding sustainability, high-quality regional maps of deposition and an effective methodology for ongoing monitoring are necessary. That does not exist in much of the world due to the lack of long-term measurements. While measurement-model fusion can help to improve model estimates of deposition (Rubin et al., 2023), much of the world does not have consistent, long-term measurements from monitoring networks available to fuse with model outputs. The addition of satellite data can help expand coverage even as it introduces more complexity (Geddes & Martin, 2017). Because satellites measure the total column density of the portion of the Earth they observe, it is necessary to have some method of inferring deposition at the surface level from the entire column. Recent efforts to estimate wet sulfur deposition from OMI SO_2 columns combined monthly precipitation, in situ deposition measurements and a statistical model of the scavenging ratio by geographic region (L. Liu et al., 2021). This straightforward approach emphasizes the importance of both precipitation and seasonality in calculating wet deposition but is perhaps too narrowly focused to be immediately applicable to other study regions. Another approach with satellite-based wet NH_4^+

deposition estimates in China used GEOS-Chem, a 3-D chemistry transport model to calculate the ratio between atmospheric concentration and wet deposition (X. Y. Zhang et al., 2018). This method, however, results in coarse-resolution output - 2° by 2.5° - which does not improve upon the HTAP II horizontal resolution. Instead, we follow an approach adapted from research on estimating $PM_{2.5}$ concentrations with satellite-based aerosol optical depth (AOD) in China (Chen et al., 2018; Guan et al., 2023; Wei et al., 2019). The space-time random forest model explicitly incorporates spatial and temporal information to improve model performance and leverage the broad spatial coverage of satellite measurements without explicitly needing to develop a statistical relationship between column density and ground-level concentration.

With the eventual goal of improving global coverage, we combine satellite-based measurements of NO_2 and NH_3 total column values with ground-based measurements and model estimates of wet NO_3^- and wet NH_4^+ deposition. We use a space-time random forest to estimate deposition across the entire CONUS, an area that is well-studied with enough ground-based measurements available to assess performance.

3.2 Methods

My approach uses measurements from the Ozone Measuring Instrument (OMI) onboard the Aura satellite to map wet NO_3^- deposition. OMI is a nadir-viewing spectrometer onboard NASA's Aura Satellite. It was launched in 2004 and has a 16-day repeat cycle in a sun-synchronous orbit. OMI provides NO_2 total column values with a 13 km x 24 km spatial resolution. Monthly level 3 NO_2 total column density measurements from OMI were retrieved for 2010. OMI is a nadir-oriented ultraviolet-visible spectrometer onboard the Aura satellite which was launched in 2004 (Levelt et al., 2006). Column density is calculated via a principal component analysis algorithm from the National Aeronautics and Space Administration (NASA) (C. Li et al., 2013). Total column density values are in Dobson units (DUs, /km^2 1 DU = 2.69 × 10^{26} molecules).

I also use measurements from the Infrared Atmospheric Sounding Interferometer (IASI) to map wet NH_4^+ deposition. IASI is a Fourier Transform Spectrometer onboard the MetOP-A, -B, and -C satellites. MetOP-A was launched in 2006. The IASI swath width is 48.3°, corresponding to 2 x 1100 km on the ground. IASI provides near-global coverage twice a day. Monthly daytime NH_3 columns from IASI are available from the AERIS IASI portal (https://iasi.aeris-data.fr/). It is a level 3 product, converted from a calculation of the hyperspectral range index (HRI) with a neural network (Clarisse et al., 2018; Whitburn et al., 2016).

Global monthly precipitation for 2010 is available from the Tropical Rainfall Measuring Mission (TRMM) Precipitation Radar, a satellite that operated from 1997 to 2015 (NASA, 2011) in a low inclination orbit from 40N to 40S latitude. A 0.25º x 0.25º grid of average 2010 precipitation in mm was downloaded from the National Aeronautics and Space Administration (NASA)'s EarthData portal.

Total cloud cover is available as the National Centers for Environmental Prediction – Department of Energy Atmospheric Model Intercomparison Project version II (NCEP-DOE AMIP-II) reanalysis (Kanamitsu et al., 2002). Monthly cloud cover is estimated at 2.5° resolution from 1979 to 2024.

Land cover is from the North American Land Change Monitoring System (NALCMS, https://www.mrlc.gov/data/north-american-land-change-monitoring-system), a collaborative initiative between the USGS, Natural Resources Canada (NRCan), the National Institute of Statistics and Geography (INEGI), the National Commission for the Knowledge and Use of Biodiversity, and the National Forestry Commission. NALCMS provides 30m land cover products from 2005 onwards with 19 different classifications.

Monthly averaged NH_4^+ and NO_3^- wet deposition measurements are available from the National Atmospheric Deposition Program (NADP)'s National Trend Network (NTN). Measurements were filtered for completeness, resulting in 1692 observations from 200 sites.

Random forest models, as described in Breiman's work are widely used in remote sensing studies (Belgiu & Drăguţ, 2016; B. Guo et al., 2021; Rubin et al., 2021). The model builds independent decision trees with a goal of minimizing bias by selecting samples with replacement and then takes the average of probabilities from each tree to classify a new sample (Breiman, 2001). We used the randomForest package in R (R Core Team, 2022) to train a random forest on a randomly selected 60% of the data, leaving the remaining 40% for validation. We explicitly included space-time information, following the approach describe by Guam et al. (Guan et al., 2023).

I also constructed maps of NO_3^- and NH_4^+ using inverse-distance weighting (IDW) based only on NTN measurements for the CONUS. Currently, the NADP only has publicly available annual maps but the monthly measurements are available so for a more meaningful comparison I constructed monthly maps using a similar though more basic methodology to the NADP's approach (D. B. Schwede & Lear, 2014). IDW has known issues, such as creating artifacts and not performing well in regions with large amounts of variability (Rubin et al., 2023), but it enables us to compare my results at a more meaningful timescale.

3.3 NO_3^- Deposition

Figure 3.1 shows the performance of the space-time random forest (STRF) with a training dataset (60% split) and validation dataset (40% split). The mean absolute error (MAE) for the validation data is 0.08 kg/ha and the root mean square error (RMSE) is 0.14 kg/ha. While the STRF does struggle to accurately predict higher measurements of NO_3^-, it performs well at the lower end of the range where most of the measurements are concentrated. Applying the STRF algorithm to the CONUS to essentially downscale the HTAP II estimates of wet NO_3^- deposition results in a 0.1° resolution gridded map for the CONUS for each month of 2010, shown in **Figure 3.2**. Deposition is highest in the Midwest during the winter and early spring (~ 3 mg/ha) and then declines throughout the summer and fall, although there remain some hotspots in the Southwest in July and August (~2 mg/ha). The spatial pattern of high concentrations in the Midwest and particularly low concentrations on the west coast match the NADP's map of wet nitrate deposition for 2010. This can be seen in **Figure 3.3**, which shows the difference between my map of NO_3^- and the NADP's data, mapped with IDW. In January and February, my deposition estimates are lower than the NADP's data by 1 mg/ha in the Midwest and higher by 1 mg/ha in the Ohio Valley region. My map overestimates wet NO_3^- deposition in northeastern Montana in April by 3 mg/ha but tends to underestimate by less than 1 mg/ha for the rest of the country.

3.4 NH_4^+ Deposition

Figure 3.4 shows the performance of the space-time random forest (STRF) with a training dataset (60% split) and validation dataset (40% split) for NH_4^+ wet deposition. The mean absolute error (MAE) for the validation data is 0.03 kg/ha and the root mean square error (RMSE) is 0.06 kg/ha. Applying the STRF algorithm to the CONUS to essentially downscale the HTAP II estimates of wet NH_4^+deposition results in a 0.1° resolution gridded map for the CONUS for each month of 2010, shown in **Figure 3.5**. Deposition is highest in the Midwest during the spring (~ 1.5 mg/ha) and then declines throughout the summer and fall, although the spatial pattern remains consistent. The spatial pattern of high concentrations in the Midwest and particularly low concentrations in the West and Northeast match the NADP's map of wet

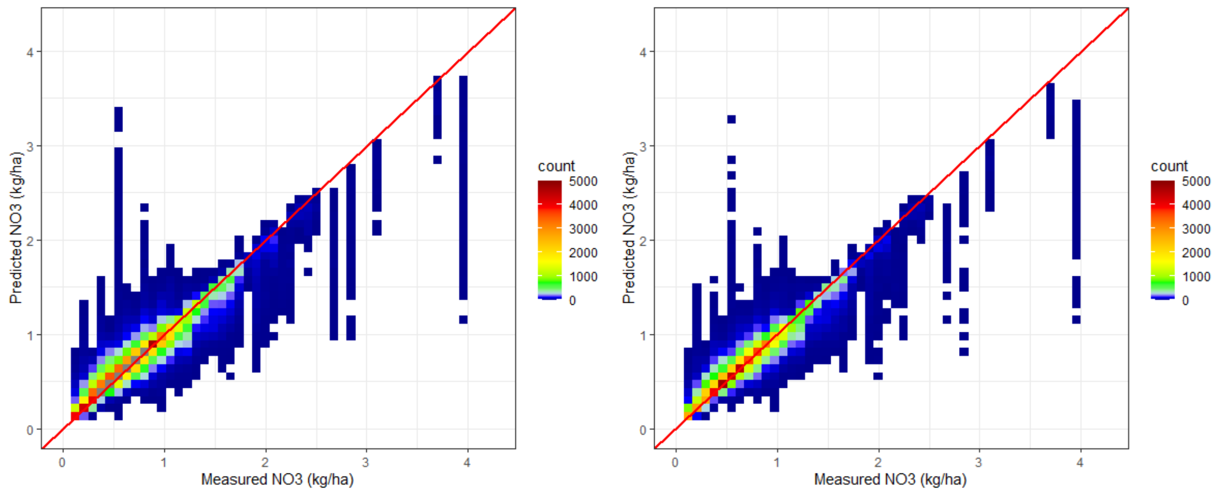

Figure 3.1 The relationship between measured and predicted NO3- for the training (left, R2 = 0.89) and testing (right, R2: 0.89) datasets.

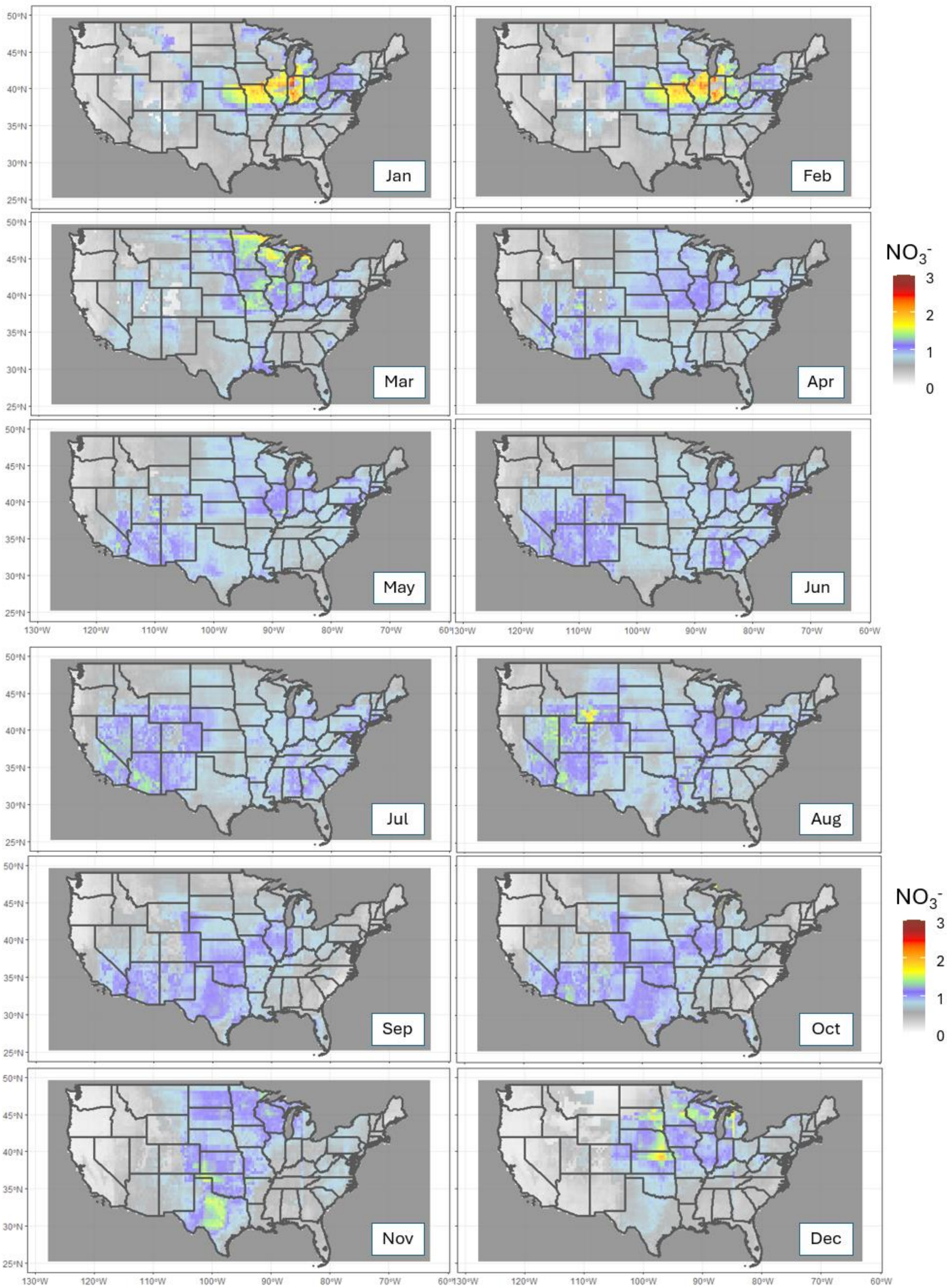

Figure 3.2 Monthly wet NO3- deposition over the CONUS in 2010, as modeled from HTAP and OMI satellite data in mg/ha.

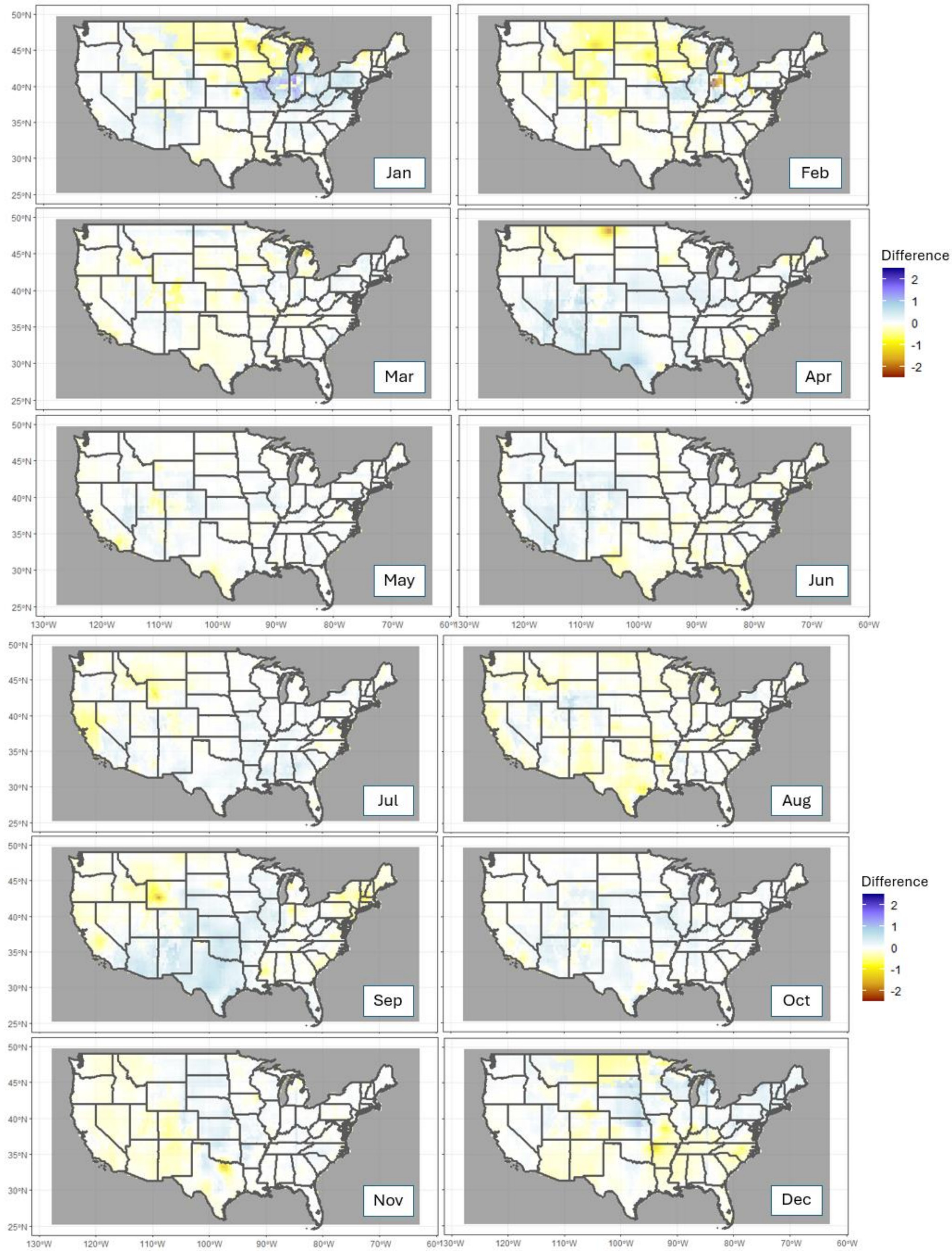

Figure 3.3 The difference in monthly wet NO3- deposition over the CONUS in 2010 between the RF model estimated wet deposition and an estimate from an IDW map of NADP's NTN wet deposition measurements in mg/ha.

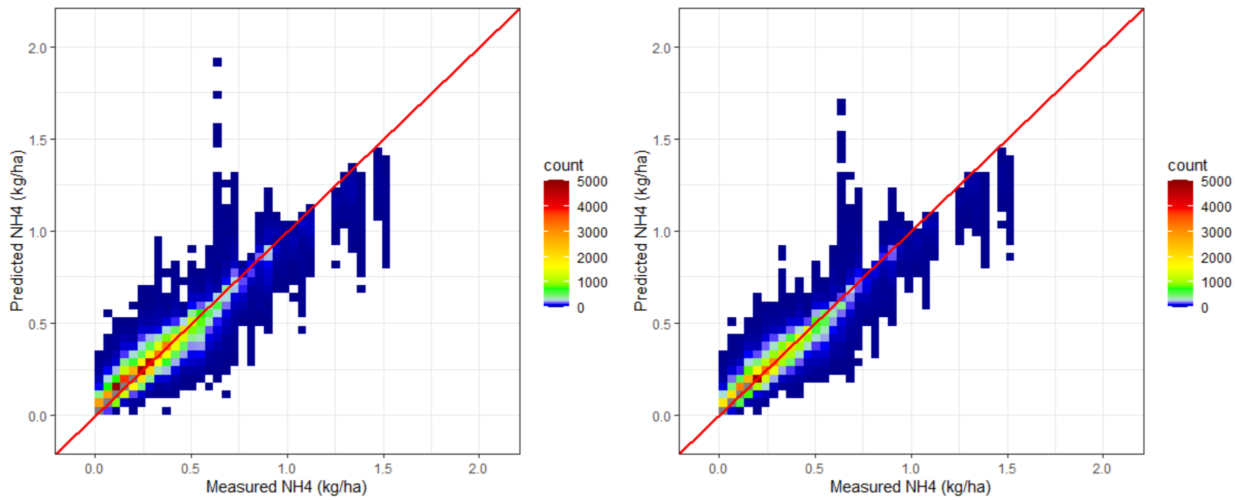

Figure 3.4 The relationship between measured and predicted NH4+ for the training (left, R2 = 0.92) and testing (right, R2: 0.92) datasets.

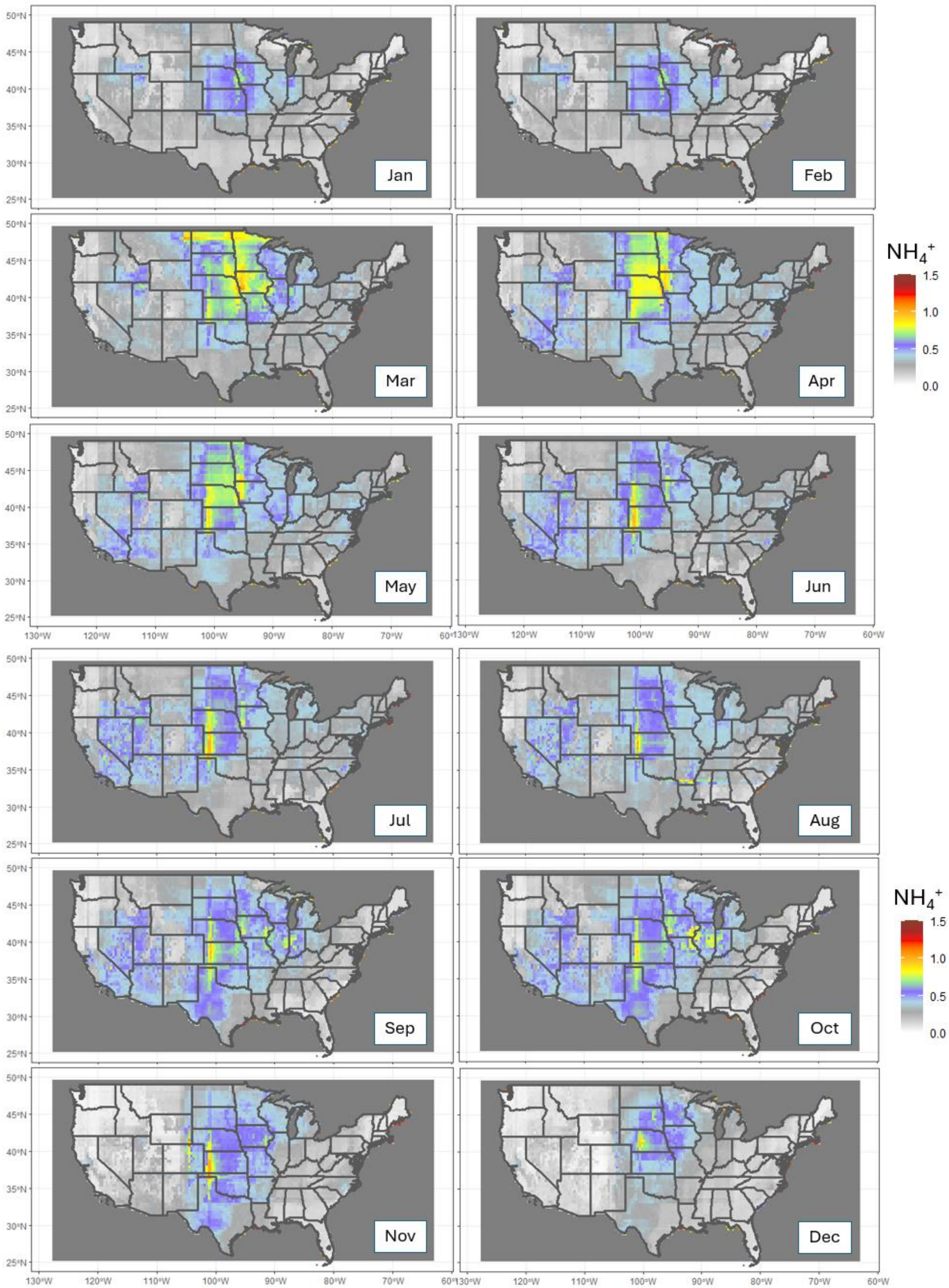

Figure 3.5 Monthly wet NH4+ deposition over the CONUS in 2010, as modeled from HTAP and OMI satellite data in mg/ha.

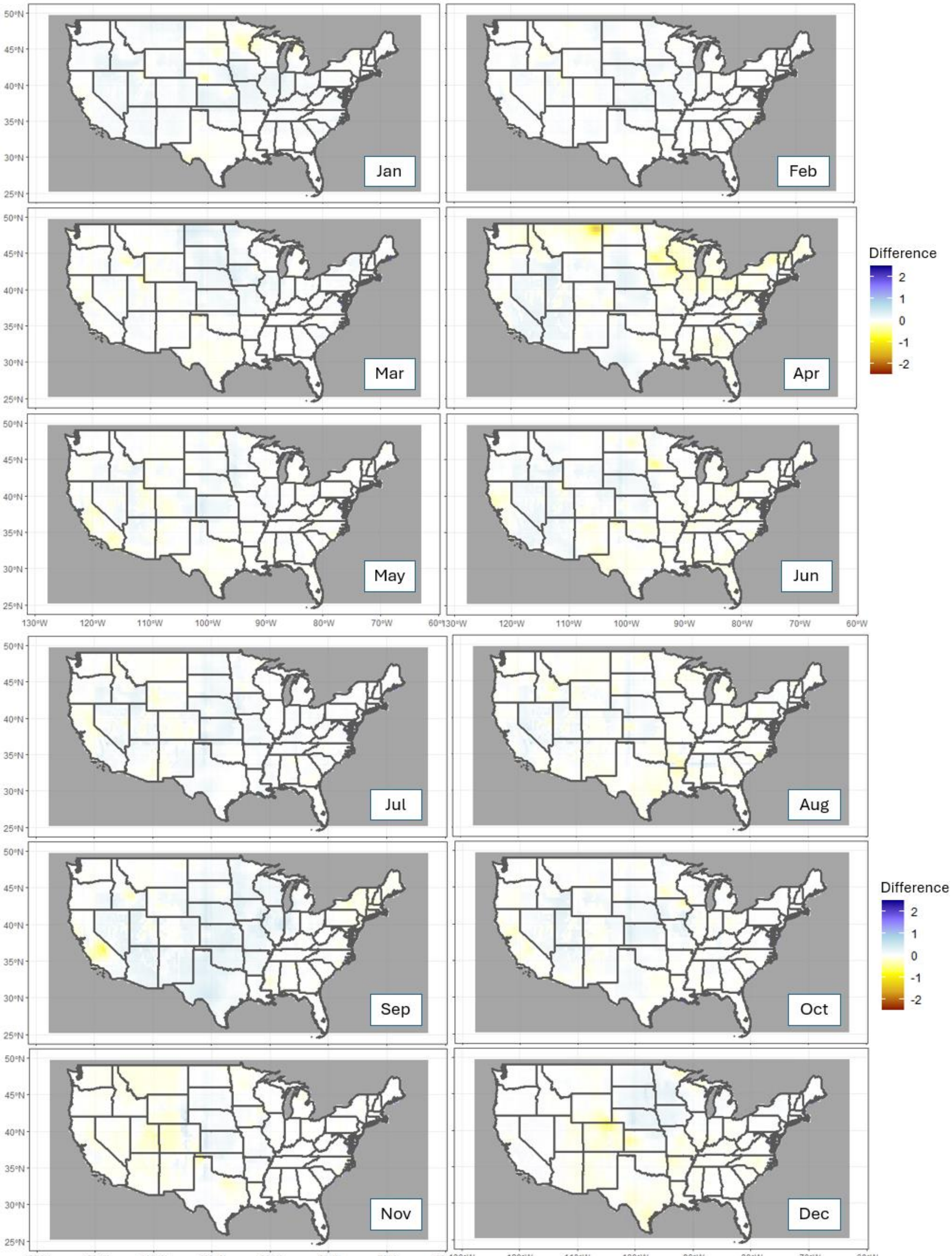

Figure 3.6 The difference in monthly wet NH4+ deposition over the CONUS in 2010 between the RF model estimated wet deposition and an estimate from the NADP's NTN wet deposition maps in mg/ha. Regional averages as estimated by the STRF are shown in Table 3.1.

ammonium deposition for 2010. This can be seen in **Figure 3.6**, which shows the difference between my map of $NH_4^+$and the NADP's data, mapped with IDW. For most of the CONUS for the majority of the year, the difference between my map of NH_4^+ and the NADP's IDW data is less than 1 mg/ha. However, in northeastern Montana in April, my maps overestimate deposition by 2 mg/ha.

3.5 Discussion

The most important variables for the STRF prediction are space, time, and elevation, which is also what Guan et al. (2023) found in their $PM_{2.5}$ study with a space-time random forest model. While these variables should not be important in a mechanistic model of wet deposition and ideally, we would be able to predict deposition from satellite data without needing the date and location of the ground-based measurements, the model explicitly relies on them as a proxy for information that cannot easily be measured and therefore incorporated into the model. Some studies have shown that precipitation amounts increase with elevation in mountainous regions (Daly et al., 2008) while the concentration of solutes like NH_4^+ and NO_3^- decreases (Latysh & Wetherbee, 2012), resulting in no apparent linear relationship between the two (Clow et al., 2015). However, the fact that the STRF does heavily depend on elevation means that there is a useful non-linear relationship between deposition and elevation.

The STRF predicts slightly higher NO^{3-} deposition than the NADP maps in much of the Southwest, by less than 1 kg/ha/month, but lower deposition elsewhere, particularly on the west coast (less than 1 kg/ha/month) and the northern Midwest (between 1 and 2 kg/ha/month). Some of these differences where NADP projects higher values are driven by a lack of OMI satellite data for those regions, such as North and South Dakota in January and February. These data gaps are due to a combination of cloud cover and other factors that mean the pixels do not pass quality assurance checks and cannot be used for analysis.

Satellite data products inherently contain uncertainty because of interference from the atmosphere and the difficulty in separating the desired measurement from noise. Regions at higher elevations or with unusual surface conditions may have systematic errors in deposition measurements due to the principal component analysis retrieval method (Fioletov et al., 2016; Yan et al., 2016). Additionally, cloudiness is a concern. Particularly cloudy regions may only have a few observations available over the entire year for 2010, meaning the annual average is biased by clear, sunny days and does not account for rainy days when wet deposition may be higher. This is called clear-sky bias (Geddes et al., 2012; Krotkov et al., 2016; McLinden et al., 2014). We make an effort to correct for this bias by including cloud cover as a predictor variable in the STRF but we cannot simulate data that do not exist on particularly cloudy days, potentially leading to a small but systematic underestimation in some regions. For example, January 2010 is shown in **Figure S3.1** and there are no OMI measurements over parts of the Upper Midwest and Rocky Mountains, so the original HTAP II grid is unchanged in those locations. This could be due to errors in the satellite processing other than cloudiness. For example, the systematic removal of negative values from the satellite columns during pre-processing yields a bias towards higher values. The negative values are an error and cannot be used since there is no way to interpret a negative average deposition over a particular region, but these negative values could potentially correspond to very low deposition values that are improperly processed. Another consideration is that IASI is known to be less reliable during temperature inversions and wintertime, though the reanalysis dataset that we use does have temperature corrections from the boundary layer to account for this issue. It is important to note that *in situ* measurements also have biases and while they are used as ground truth data here, they also include some uncertainty. For example, if a measurement is lower than the detection limit, it may be corrected to reflect the detection limit, rather than the actual measurement value which is unknown.

Recent work using CMAQ to model NO_3^- deposition found that the highest wet deposition from 2002-2017 occurred in the Upper Midwest (7.83 kg/ha/yr), Ohio Valley (10.44 kg/ha/yr), and the Northeast (9.79 kg/ha/yr) (Benish et al., 2022). They also estimated wet NH_4^+ deposition in the CONUS and found the highest values in the Ohio Valley (3.59 kg/ha/yr), the Upper Midwest (3.76 kg/ha/yr), and the South (2.74). These values are slightly lower than my estimates, particularly in the Upper Midwest (**Table 3.1**). This is likely due to the MMF procedure where grid cells that do not have corresponding satellite measurements instead are filled in by the original HTAP II model estimates. These locations are primarily in the Upper Midwest in the winter months. Other work modeling long-term trends of inorganic N with WRF-CMAQ also finds similar values to mine, although their ecoregion divisions do not correspond exactly to the same climate divisions (Y. Zhang et al., 2018).

At the CONUS level, compared to the HTAP II estimate of wet NO_3^- deposition for 2010 of 4.13 kg/ha, the STRF estimate corrects the large underestimation to 8.89 kg/ha/yr, similar to the

Table 3.1 Regional wet deposition averages in kg/ha/yr for 2010, as estimated by the STRF.

Region	Wet NO_3^-	Wet NH_4^+
Northeast	8.43	2.39
Northwest	4.83	2.30
Northern Rockies	8.40	4.37
Southeast	7.83	2.33
South	9.80	4.17
Southwest	9.82	3.60
Ohio Valley	11.56	4.13
Upper Midwest	10.81	5.00
West	7.15	3.38

NTN-IDW estimate of 8.46 kg/ha/year. The STRF wet NH_4^+ deposition estimate also corrects the large overestimation from the HTAP II grids from 13.61 kg/ha/yr to 3.67 kg/ha/yr, very similar to the NTN-IDW estimate of 3.21 kg/ha/yr for the CONUS.

Still, the average values mask the large seasonal changes in wet deposition that correspond with agricultural cycles (L. Zhang et al., 2012). Agriculture accounts for the majority of both nitrous oxide and ammonia emissions in the US (US EPA, 2015b), which eventually become deposition. This means that the seasonal timing of deposition should follow immediately after soil management practices that increase emissions, such as fertilization. In the Midwest, this is typically early spring, which corresponds well with the peak of ammonium deposition (**Figure 3.5**). However, winter deposition peaks in the Midwest are primarily composed of NO_3^-, which is likely due to the lack of crop demand for N, the large amount of precipitation and runoff, and subsequent high levels of nitrification on farm systems (Fenn et al., 2003). It could also be related to OMI retrieval errors over snow (O'Byrne et al., 2010).

3.6 Conclusions

The STRF is a promising new method of incorporating satellite data into existing models of wet deposition and expanding the regions with measurements available to correct the model. The seasonal patterns of wet N deposition in 2010 are well reproduced and my estimates are similar to those of prior studies that require intensive modeling and gridded datasets that are not available for much of the world. My approach relies instead on machine learning to combine the global HTAP II model estimates with satellite data. These efforts demonstrate good performance over a wide, geographically diverse region and suggest that machine learning and satellite data have a critical role to play in improving global maps as well.

Chapter 4 Projected Global Sulfur Deposition with Climate Intervention

4.1 Climate Intervention

Anthropogenic climate change is the most pressing global challenge we face today and the widespread harmful impacts to humans and ecosystems are being felt worldwide (IPCC, 2022; Scheffers et al., 2016). While scientists have warned for decades that it is essential to decrease carbon dioxide (CO_2) inputs to the atmosphere to mitigate climate change (d'Arge et al., 1982; Schultz & Kasting, 1997), current pledges to reduce emissions are not adequate to even maintain warming at two degrees Celsius above historical temperatures (Robiou du Pont & Meinshausen, 2018; Tollefson, 2019). A variety of responses will therefore be needed to slow warming, in addition to reducing emissions and adapting to the future warmer climate. This may include climate intervention (National Research Council, 2015). Climate intervention approaches fall into one of two categories: removing CO_2 from the atmosphere or modifying the way solar radiation is reflected by the atmosphere (Shepherd, 2012). While CO_2 removal will likely be part of a portfolio of responses to climate change, it may not be enough due to the costs of scaling CO_2 utilization (Hepburn et al., 2019). The most commonly researched method of altering the atmosphere's radiative budget is stratospheric aerosol injection (SAI) (Crutzen, 2006; Lawrence et al., 2018; W. Smith & Henly, 2021) using aircraft-based delivery (Tracy et al., 2022).

SAI is extremely controversial in part because it is a global intervention without clear policy frameworks or a governing body in charge of the decision to deploy, and in part because it calls into question both our duties and our rights towards the natural world and other humans. Studies disagree about the magnitude and impacts of disruptions to precipitation and temperature that it would cause (Brendan Clark et al., 2023; P. Irvine et al., 2019; P. J. Irvine & Keith, 2020; Kortetmäki & Oksanen, 2023). SAI is one of the only geoengineering options with the technological availability to feasibly deploy globally within a politically relevant timeframe (Britta Clark, 2023). SAI implementation costs are also relatively inexpensive compared to the cost of mitigating temperature warming to less than 1.5 degrees Celsius or the costs of unmitigated climate change (W. Smith & Wagner, 2018). Decreasing radiative forcing does not address the fundamental issue of the high concentration of greenhouse gases in the atmosphere, but it would allow more time for the world to reduce and stabilize emissions in the very near term. While it should not distract from the work of actually reducing emissions on a global scale or developing carbon removal technology, SAI remains a viable stopgap measure and ought to be investigated thoroughly from a modeling perspective (Long & Shepherd, 2014; Y. Xu et al., 2020).

There is a growing body of scientific research on global temperature and precipitation patterns that may be altered by SAI (P. Irvine et al., 2019; P. J. Irvine & Keith, 2020; Walker Lee et al., 2020), similar to the way volcanic aerosols alter radiation (Gu et al., 2003), but other environmental variables are less well constrained. Sulfate deposition is of particular interest because sulfur dioxide (SO_2) injected into the stratosphere will quickly produce sulfate aerosols. Atmospheric sulfur deposition is an important part of many biogeochemical cycles (Pye et al., 2020; Tjiputra et al., 2016). However, when exceeding critical loads, sulfur can have harmful impacts on both human and ecosystem health. SAI takes place in the stratosphere, not the troposphere, but there are interactions between the two and the aerosol particles will settle to the surface within a few years (Visioni et al., 2020).

One study comparing GEOS-Chem and ULAQ-CCM found that sulfur deposition will increase when sulfate geoengineering is deployed (Visioni et al., 2018). Currently, 125 Tg of SO_2 is emitted into the atmosphere annually from anthropogenic sources, although this is trending down (Aas et al., 2019). To maintain the global temperature at 1.5º C above the historical average with SAI, about 29 Tg of additional SO_2 would be required annually by the end of the century, although this amount depends on injection strategy and deployment (Niemeier & Timmreck, 2015; Visioni et al., 2021). The sulfur deposition would also be impacted by unmitigated climate change as increased greenhouse gases in the atmosphere react with the hydrological cycle (Tracy et al., 2022). It is important to determine where the sulfur deposition will end up and over what time frame both with and without SAI.

The Climate Model Intercomparison Project Phase 6 (CMIP6) is organized by the World Climate Research Program (WCRP)'s Working Group of Coupled Modeling (WGCM) to coordinate climate model experiments worldwide, using common protocols, climate forcings, and output formats to provide future climate projections (Eyring et al., 2016). The newest iterations of the CMIP models are based on a possible climate outcome from a Representative Concentration Pathway (RCP) between 1.9 and 8.5 W/m^2 of radiative forcing matched with a Shared Socioeconomic Pathway (SSP 1-5) (O'Neill et al., 2016). The SSPs describe the potential social development that might in the future occur based on factors like population size, education, energy demand, and other non-climate factors (Riahi et al., 2017). The Geoengineering Model

Intercomparison Project (GeoMIP, **Figure S4.1**) is a suite of climate model experiment designs built on CMIP6 simulations to address geoengineering as a response to climate change (B. Kravitz et al., 2015; Ben Kravitz et al., 2011). The G6sulfur scenario includes stratospheric sulfate aerosol injection to reduce net forcing from SSP5-8.5 to SSP2-4.5. SSP5 combined with RCP8.5 is often referred to as the "worst-case" climate scenario for our world, with 8.5 W/m^2 of radiative forcing and socioeconomic conditions characterized by a reliance on fossil fuels for development. SSP2-4.5 is a moderate case climate scenario with 4.5 W/m^2 radiative forcing and a middle-of-the-road approach without extreme social, economic, technological, or land use changes from historical patterns. We use the outputs of the three earth system models available from the CMIP6 archive for G6sulfur, SSP2-4.5, and SSP5-8.5 to investigate the long-term impacts of SAI on sulfur deposition.

4.2 Methods and Data

This study utilized the G6sulfur model outputs from the CMIP6 archive (available at https://esgf-node.llnl.gov/projects/cmip6) to analyze sulfur deposition changes due to SAI under climate change. Since G6sulfur is designed to reduce net radiative forcing from SSP5-8.5 to SSP2-4.5 (Visioni et al., 2021), we also retrieved model outputs from SSP5-8.5 and SSP2-4.5 for comparisons. Across the CMIP6 archive, only three models provide sulfur deposition-relevant variables—wet SO_2, dry SO_2, wet SO_4^{2-}, dry SO_4^{2-}, and precipitation flux—under the G6sulfur scenario (**Table 4.1**). Hence, we retrieved the outputs from these three models under SSP5-8.5 and SSP2-4.5 for fair comparisons. Historical outputs during 1950–2014 were also retrieved for the same models to compare with the three future scenarios. None of the models explicitly incorporate bi-directional flux for sulfur. All three models include interactive stratospheric chemistry but only UKESM1-0-LL and CESM2-WACCM include interactive aerosol microphysical schemes while CNRM-ESM2-1 uses prescribed ozone fields (Séférian et al., 2019; Simone Tilmes et al., 2022). UKESM1-0-LL and CESM2-WACCM include interactive aerosol microphysical models and inject SO_2 at specific latitudes and CNRM-ESM2-1 uses an input dataset from the GeoMIP G4 Specified Stratospheric Aerosols (G4SSA) experiment to prescribe the aerosol distribution and optical properties such that the target temperature is reached (S. Tilmes et al., 2015). Despite this, we include CNRM-ESM2 deposition variables for comparison with the other two models.

Table 4.1 Summary of selected CMIP6 model outputs in this work.

Earth System Models	*Horizontal Grid Resolution*	*Climate Scenario*			
		Historical	SSP2-4.5	SSP5-8.5	G6sulfur
CESM2-WACCM	192x288	r1p1i1f1	r1p1i1f1	r1p1i1f1	r1p1i1f2
CNRM-ESM2-1	128x256	r1p1i1f2	r1p1i1f2	r1p1i1f2	r1p1i1f2
UKESM1-0-LL	144x192	r1p1i1f2	r1p1i1f2	r1p1i1f2	r1p1i1f2

The 13 ecoregions were defined by clustering climate, soil, and topography types and fitting the categories to the International Geosphere-Biosphere Programme (IGBP) ecoregion definitions (Hargrove et al., 2006; Hargrove & Hoffman, 2004; Townshend, 1992), following Yang et al. (2020). All analysis was done with R (R Core Team 2022; available at https://www.r-project.org/) and Climate Data Operators (CDO, Schulzweida, 2021; available at https://code.mpimet.mpg.de/projects/cdo).

4.3 Results

Historically, sulfur deposition peaked on a global scale in the 1980s (S. J. Smith et al., 2004). This peak can be seen in all three ESMs in Figure S4.2, which shows historical dry deposition and future estimated dry deposition for each ESM in **Table 4.1.** Dry S is projected to decline consistently from a peak of $4.33 \times 10^{-12} \pm 1.39$ kg/m^{2}s through 2100 to $1.71 \pm 0.51 \times 10^{-12}$ kg/m^{2}s for all three G6sulfur models and to $1.41 \pm 0.28 \times 10^{-12}$ kg/m^{2}s under SSP2-4.5 and $1.47 \pm 0.32 \times 10^{-12}$ kg/m^{2}s under SSP5-8.5 projections (**Figure 4.1**) because of declining anthropogenic emissions (I. Cheng et al., 2022; K. Zhou et al., 2021).

4.4 Model Discrepancies

Figure 4.2 shows the wet deposition trends by model under G6sulfur. The three models agree well enough on dry deposition trends to ensemble them together into a multi-model mean (**Figure 4.1**), but the models do not agree on wet deposition trends. UKEMS1-0-LL projects relatively consistent wet SO_4^{2-}, around $\times 10^{-12}$ kg/m^{2}s, lower than the historical peak of the1980s ($7.55 \pm 0.06 \times 10^{-12}$ kg/m^{2}s). Wet SO_2 deposition is projected to consistently decrease from $1.23 \pm 0.17 \times 10^{-12}$ kg/m^{2}s to $9.36 \pm 0.11 \times 10^{-13}$ kg/m^{2}s by 2100 (**Figure 4.2A**). However, under

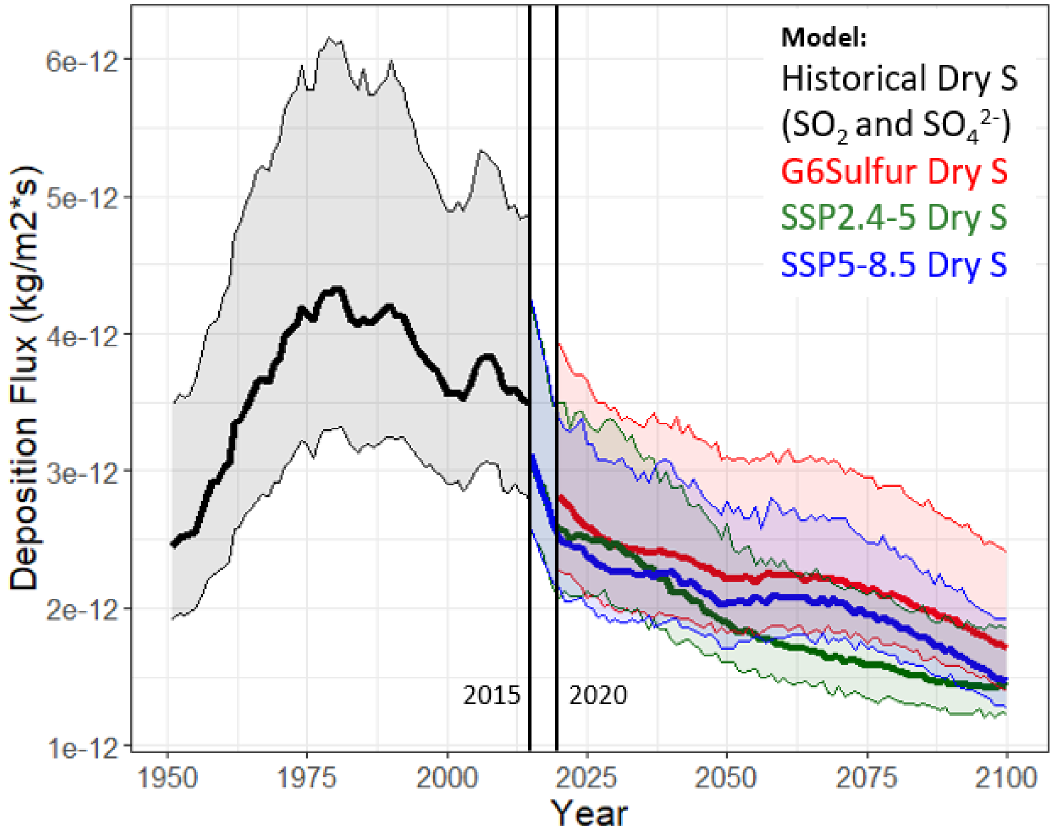

Figure 4.1 Global dry S (both SO2 and SO_4^{2-}) deposition flux from historical estimates and three future climate scenario projections, SSP2-4.5, SSP5-8.5, and G6sulfur.The solid lines represent the ensemble mean and the shaded region is the spread across models. The differences between models can be seen in Figure S4.2.

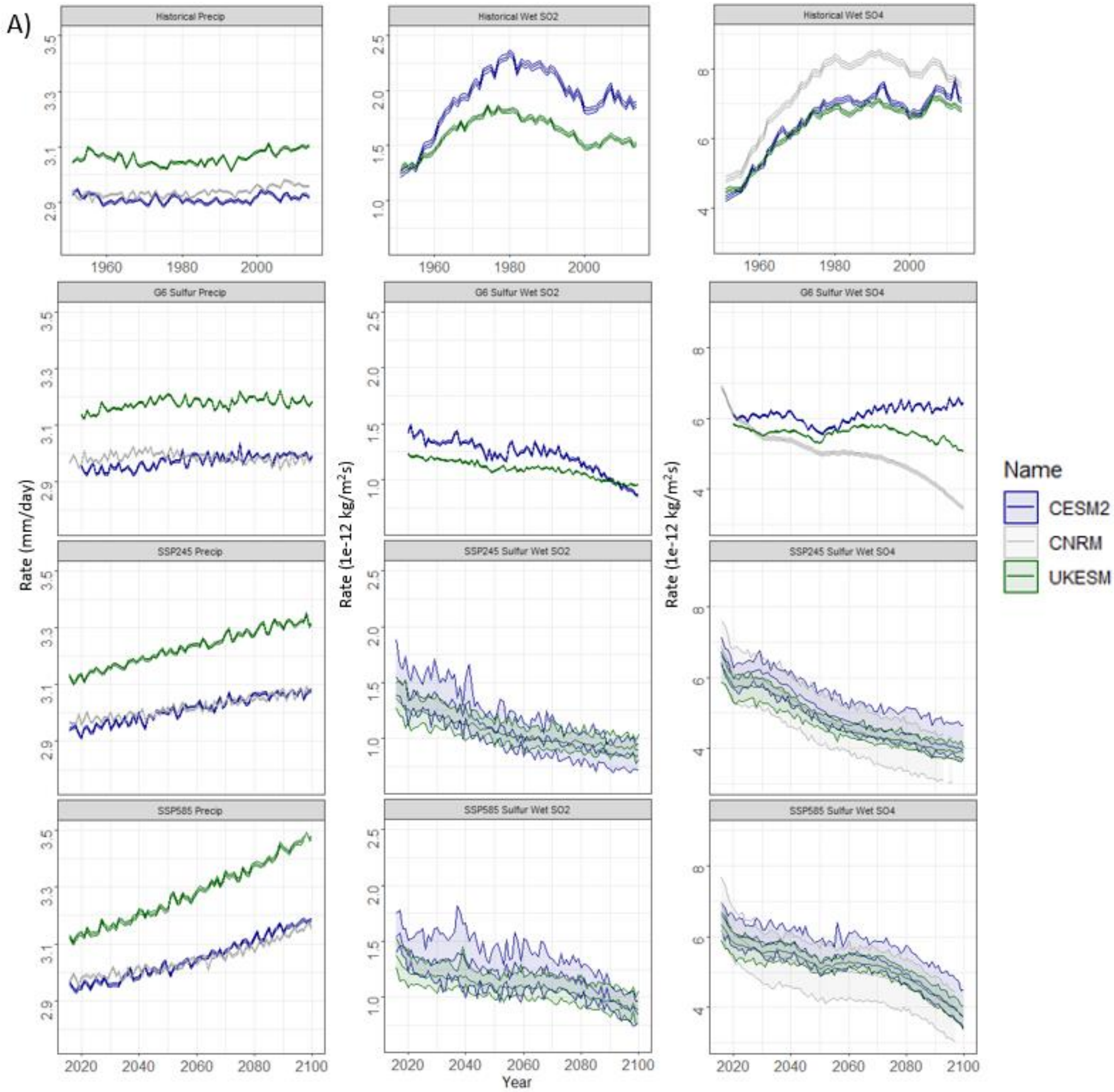

Figure 4.2 Projected A) annual and B) monthly precipitation and wet sulfur (SO_2 and SO_4^{2-}) deposition from UKESM1-0-LL, CESM2-WACCM, and CNRM-ESM2-1 during the historical time period (1980-2020) and under G6 Sulfur, SSP2-4.5, and SSP5-8.5 conditions (2020-2100).

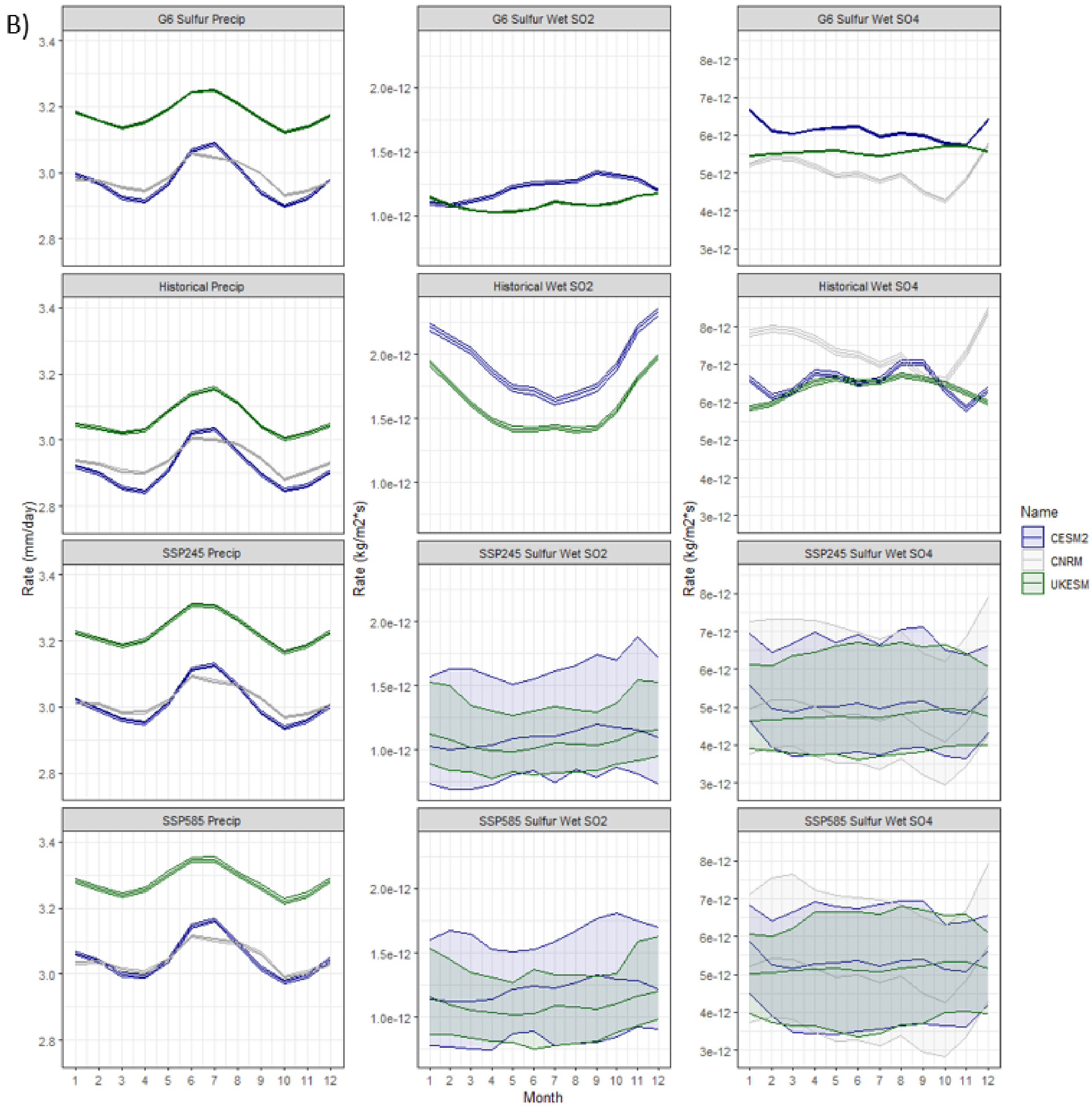

Figure 4.2 (Continued)

both SSP2-4.5 and SSP5-8.5, wet SO_2 is expected to decline from $1.36\pm0.14 \times 10^{-12}$ to $8.91\pm0.01 \times 10^{-13}$ kg/m^{2}s and $1.37\pm0.18 \times 10^{-12}$ kg/m^{2}s to $8.71\pm0.12 \times 10^{-13}$ kg/m^{2}s, respectively. Wet SO_4^{2-}, similarly, is expected to decline under the two SSP scenarios from $6.44\pm0.32 \times 10^{-12}$ to $3.86\pm0.18 \times 10^{-12}$ under SSP2-4.5 and from $3.73\pm0.34 \times 10^{-12}$ kg/m^{2}s to $6.46\pm0.39 \times 10^{-12}$ kg/m^{2}s under SSP5-8.5

In terms of seasonality, according to UKESM1-0-LL, both wet SO_4^{2-} and wet SO_2 remain constant throughout the year under G6sulfur (an average of $5.57\pm0.02 \times 10^{-12}$ kg/m^{2}s for wet SO_4^{2-} and $1.09\pm0.01 \times 10^{-12}$ kg/m^{2}s for wet SO_2), SSP2-4.5 (an average of $4.77\pm1.31 \times 10^{-12}$ kg/m^{2}s for wet SO_4^{2-} and $1.06\pm0.03 \times 10^{-12}$ kg/m^{2}s for wet SO_2), and SSP5-8.5 (an average of $5.15\pm1.38 \times 10^{-12}$ kg/m^{2}s for wet SO_4^{2-} and $1.09\pm0.03 \times 10^{-12}$ kg/m^{2}s for wet SO_2) throughout the year with a high in December/January and a low in the northern hemisphere summer season as precipitation increases from 3.12±0.08 mm/day to 3.25±0.06 mm/day. This is not consistent with historical patterns of wet SO_2 deposition which has historically declined during May-October, or with historical patterns of wet SO_4^{2-} deposition which has, on average, increased during these months (**Figure 4.2B**).

CESM2-WACCM projects a slight increase in precipitation from 2.89±1.04 mm/day in 1950 to 3.03±0.08 mm/day through 2075 (**Figure S4.3**) and a large increase in wet SO_4^{2-} deposition, with deposition dipping down below 1960s levels ($5.63\pm0.55 \times 10^{-12}$ kg/m^{2}s) until the 2050s and then increasing steadily to nearly as high as the 1980s peak ($6.59\pm0.78 \times 10^{-12}$ kg/m^{2}s) by the end of the century (**Figure 4.2B**). Wet SO_2 deposition is projected to decrease from $1.49\pm0.18 \times 10^{-12}$ kg/m^{2}s in 2020 to $8.58\pm0.95 \times 10^{-13}$ kg/m^{2}s by 2100. Under SSP2-4.5 wet SO_4^{2-} is projected to decline consistently from the 1980s peak to $3.97\pm0.04 \times 10^{-12}$ by 2100 and wet SO_2 is projected to decline to $8.36\pm1.22 \times 10^{-13}$ over the same time period.

On a seasonal basis, historically wet SO_4^{2-} has increased slightly during May-October as precipitation increases. However, under G6 Sulfur, the CESM2-WACCM model projects a slight decline during those months from $6.67\pm0.84 \times 10^{-12}$ kg/m^{2}s to $5.75\pm0.62 \times 10^{-12}$ kg/m^{2}s for SO_4^{2-} and a slight increase from $1.08\pm0.34 \times 10^{-12}$ kg/m^{2}s to $1.33 \pm0.47 \times 10^{-12}$ kg/m^{2}s for wet SO_2, as precipitation increases to 3.09±.10 mm/day from 2.89±0.07 mm/day. Under SSP2-4.5 and SSP5-8.5 wet SO_4^{2-} is projected to remain constant at $5.07\pm1.42 \times 10^{-12}$ kg/m^{2}s and $5.33\pm 1.49\times 10^{-12}$ kg/m^{2}s respectively. Precipitation increases during the northern hemisphere summer months from a low of 2.94±0.00 mm/day to 3.13±0.00 mm/day under SSP2-4.5 and 2.80±0.01 mm/day to 3.16±0.01 mm/day under SSP5-8.5.

According to the CNRM-ESM2-1 model, precipitation has historically remained constant at 2.94±0.00 mm/day from the 1950s to the present day. Under G6 Sulfur, this trend is projected to continue at 2.99±0.00 mm/day. However, under SSP2-4.5, precipitation is projected to increase to 3.09±0.00 mm/day and under SSP5-8.5, it will increase to 3.18±0.00 mm/day by 2100. All 3 scenarios project a large decline in wet SO_4^{2-} deposition from the 1980s peak of $8.49 \pm 0.88 \times 10^{-12}$ kg/m^{2}s to $3.45 \pm 0.75 \times 10^{-12}$ kg/m^{2}s for G6 Sulfur, for SSP2-4.5, and for SSP5-8.5 by 2100 (**Figure 4.2B**). Unlike the other two ESMs, CNRM-ESM2-1 historical estimates show that wet SO_4^{2-} has decreased during May-October from $8.42 \pm 0.05 \times 10^{-12}$ kg/m^{2}s to $6.58 \pm 0.01 \times 10^{-12}$ kg/m^{2}s. This pattern is consistent with G6 Sulfur projections which estimate a low of $4.26 \pm 0.05 \times 10^{-12}$ kg/m^{2}s and a high of $5.75 \pm 0.05 \times 10^{-12}$ kg/m^{2}s. Under SSP2-4.5 and SSP5-8.5 wet SO_4^{2-} deposition is relatively constant at $4.84 \pm 1.72 \times 10^{-12}$ kg/m^{2}s and $5.01 \pm 21.81 \times 10^{-12}$ kg/m^{2}s, respectively. Precipitation increases during May-October under G6 Sulfur, SSP2-4.5, and SSP5-8.5 from a low of 2.93 mm/day to a high of 3.06 mm/day and a low of 2.97 mm/day to a high of 3.09 mm/day and a low of 2.99 mm/day to a high of 3.11 mm/day, respectively. CNRM-ESM2-1 projections do not include publicly available wet SO_2.

4.5 SAI by Ecoregions

Focusing on CESM2-WACCM and UKESM1-0-LL projections (the two models with publicly available projections for both SO_2 and SO_4^{2-} deposition) by ecoregion highlights the parts of the world most likely to be impacted by excess sulfur deposition under G6Sulfur compared to climate change under SSP2-4.5 (**Figure 4.3**). The comparison between G6 Sulfur and SSP5-8.5 is shown in **Figure S4.5**.

According to the CESM2-WACCM model, SO_2 emissions under G6 Sulfur will be higher in 2020-2040 compared to SSP2-4.5 emissions and decline with each progressive decade in savannas, grasslands, and barren or sparsely vegetated lands (**Figure 4.3**). In non-marine water bodies, deciduous needleleaf forests, mixed forests, open shrublands, woody savannas, croplands/natural vegetation mosaics, and permanent snow and ice, results are more mixed, with higher emissions under G6 Sulfur in the mid-century only to decline back to or below the SSP2-4.5 emission rate by 2100. And in evergreen needleleaf forests, evergreen broadleaf forests, and croplands SO_2 emissions experience negligible change from SSP2-4.5 levels.

Figure 4.3 The percent change from SSP2-4.5 to G6Sulfur for CESM2-WACCM and UKESM1-0-LL SO2 and SO_4^{2-} deposition by ecoregion, calculated as a difference in total deposition in Tg-S/yr. and the percent change from SSP5-8.5 is shown in Figure S4.5.

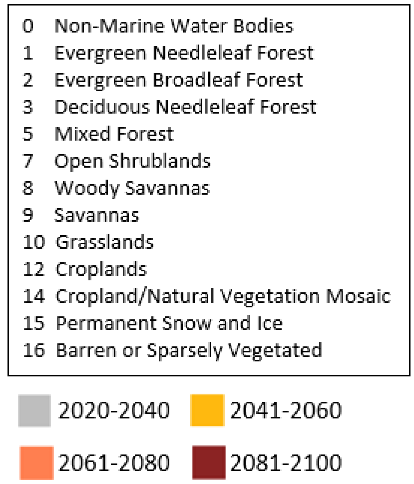

Figure 4.3 (Continued)

According to the CESM2-WACCM model, SO_4^{2-} emissions are projected to be higher from 2020-2040 under G6 Sulfur than SSP2-4.5 and decline with each progressive decade through 2100 in non-marine water bodies (from 267% to 98%), evergreen broadleaf forests (123% to 93%), mixed forests (from 170% to 113%), savannas (from 180% to 38%), grasslands (from 143% to 76%), croplands (from 134% to 82%), and barren or sparsely vegetated lands (from 136% to 51%). In deciduous needleleaf forests and open shrublands, SO_4^{2-} emissions increase mid-century relative to SSP2-4.5 (184% and 166%, respectively) only to decline to less than 100% by 2081-2100. In woody savannas, emissions are consistently higher than SSP2-4.5 emissions. In evergreen needleleaf forests emissions remain constant at 100% of SSP2-4.5 levels. And in croplands/natural vegetation mosaics and permanent snow and ice SO_4^{2-} emissions drop below 100% of the SSP2-4.5 rate mid-century only to increase to 140% and 107%, respectively, of SSP2-4.5 levels by 2081-2100.

Under G6 Sulfur, SO_2 deposition according to the CESM2-WACCM model declines relative to SSP2-4.5 levels from close to 150% to less than 100% in non-marine water bodies (from 147% to 97%), deciduous needleleaf forests (from 199% to 110%), mixed forests (from 150% to 83%), savannas (from 175% to 49%), permanent snow and ice (from 162% to 42%), and barren or sparsely vegetated lands (from 153% to 47%). In open shrublands and croplands/natural vegetation mosaics, there is no difference between G6 Sulfur and SSP2-4.5 SO_2 deposition throughout the century. Two ecoregions experience a decrease during 2041-2060 compared to SSP2-4.5 levels – from 133% to 101% in evergreen needleleaf forests and from 116% to 91% in grasslands. Other ecoregions instead will experience greater SO_2 deposition relative to SPSP2-4.5 during this time period: evergreen broadleaf forests (from 130% to 170%), woody savannas (from 140% to 190%), and croplands (from 106% to 163%).

According to the CESM2-WACCM model, SO_4^{2-} deposition is projected to be higher under G6 Sulfur than SSP2-4.5 in the 2020s and decline relative to SSP2-4.5 by 2100 in woody savannas (from 163% to 120%), savannas (from 224% to 86%), permanent snow and ice (from 179% to 90%), and barren or sparsely vegetated lands (from 149% to 87%). SO_4^{2-} emissions are projected to increase by the end of the century in non-marine water bodies (from 95% to 138%), deciduous needleleaf forests (from 99% to 170%), mixed forests (from 118% to 128%), and open shrublands (from 94% to 130%) relative to SSP2-4.5. SO_4^{2-} emissions will decline through 2061-2080 and then increase again relative to SSP2-4.5 in evergreen needleleaf forests (from 122% to

143%), grasslands (from 89% to 112%) and croplands (from 95% to 110%). In evergreen broadleaf forests, SO_4^{2-} deposition is greater relative to SSP2-4.5 levels through 2061-2080 to 144% of SSP2-4.5 deposition and then declines to 99%. In croplands/natural vegetation mosaics, SO_4^{2-} deposition declines to 86% of SSP2-4.5 deposition in 2041-2060 and then increases to 171% by 2080-2100.

According to the UKESM1-0-LL projections, SO_2 emissions will increase relative to SSP2-4.5 in woody savannas from 124% to 369% by 2081-2100. SO_2 emissions are projected to decline relative to SSP2-4.5 in non-marine water bodies (from 142% to 92%), evergreen broadleaf forests (from 146% to 84%), deciduous needleleaf forests (from 124% to 64%), mixed forests (from 128% to 100%), open shrublands (from 116% to73%), savannas (from 200% to 46%), grasslands (from 230% to 62%), and barren or sparsely vegetated lands (from 200% to 57%) throughout the century (**Figure 4.3**). Emissions are projected to remain constant at 110% of the SSP2-4.5 rate in evergreen needleleaf forests while emissions in croplands, cropland/natural vegetation mosaics and permanent snow and ice are projected to increase under G6 Sulfur to 133%, 160%, and 137% respectively, relative to SSP2-4.5 during 2041-2060 and 2061-2080 then decline back to just under 100% of SSP2-4.5 levels.

According to the UKESM1-0-LL projections, SO_4^{2-} emissions under G6 Sulfur will decline relative to SSP2-4.5 emissions in non-marine water bodies (from 206% to 84%), evergreen broadleaf forests (from 140% to 83%), mixed forests (from 145% to 92%), savannas (from 192% to 35%), grasslands (from 139% to 74%), croplands (from 148% to 80%), and barren or sparsely vegetated lands (from 145% to 45%) by the end of the century. SO_4^{2-} emissions are projected to increase relative to SSP2-4.5 in woody savannas from 134% in 2020-2040 to 359% in 2081-2100. SO_4^{2-} emissions in evergreen needleleaf forests are projected to remain constant at 105% of the SSP2-4.5 rate but emissions in deciduous needleleaf forests will increase to 152% of the SSP2-4.5 rate in 2041-2060 then decrease to 38% in 2061-2080 then increase again to 86% by 2081-2100. Open shrublands will experience an increase to 133% of SSp2-4.5 levels in 2061-2080 then a decline to 59% in the next 2 decades. SO_4^{2-} emissions in cropland/natural vegetation mosaics and permanent snow and ice decline mid-century to 96% and 57% of SSP2-4.5 levels, respectively, then increase to 135% and 106% by the end of the century.

Under G6 Sulfur, SO_2 deposition will decline in non-marine water bodies (from 138% to 80%), evergreen broadleaf forests (from 126% to 99%), 3 (from 158% to 71%), mixed forests (from

137% to 81%), open shrublands (from 80% to 91%), permanent snow and ice (from 184% to 45%), and barren or sparsely vegetated lands (from 162% to 54%) by the end of the century when compared to SSP2-4.5 SO_4^{2-} deposition. SO_2 deposition is projected to increase relative to SSP2-4.5 by mid-century in woody savannas (from 128% to 180%), savannas (from 168% to 236%), grasslands (from 115% to 167%), croplands (from 102% to 164%) and then decline below the original percentage. And SO_2 deposition is constant under G6 Sulfur at 100% of rate SSP2-4.5 rate in cropland/natural vegetation mosaics and constant at 126% of the SSP2-4.5 rate in evergreen needleleaf forests.

SO_4^{2-} deposition will increase under G6 Sulfur according to the UKESM1-0-LL projections in non-marine water bodies (from 94% to 139%), deciduous needleleaf forests (from 106% to 394%), open shrublands (from 94% to 122%), and cropland/natural vegetation mosaics (from 145% to 156%) relative to SSP2-4.5 estimates. It will decrease in savannas (from 196% to 88%), grasslands (from 152% to 112%), croplands (from 136% to 107%), permanent snow and ice (from 220% to 107%), and barren or sparsely vegetated lands (from 146% to 82%) relative to SSP2-4.5 deposition rates. Under G6 Sulfur, SO_4^{2-} deposition in evergreen broadleaf forests increases mid-century from 122% to 148% and evergreen needleleaf forests decreases from 151% to 108% mid-century then returns to 129% of SSP2-4.5 deposition by 2081-2100. Deposition in mixed forests and woody savannas decreases mid-century to 105% and 166% relative to SSP2-4.5 levels, respectively, then increases to 151% and 210%, respectively, by the end of the century.

4.6 Discussion

Past projections from CESM1-WACCM estimate a total global deposition rate of 40 Tg-S yr^{-1} in 2020, declining to 23 Tg-S yr^{-1} by 2100 under RCP8.5 (Visioni et al., 2020). However, in this study, CESM2-WACCM projects a total global deposition rate of 71.6 Tg-S yr^{-1} in 2020, increasing to 82.0 Tg-S yr^{-1} by 2100 under SSP5-8.5 and UKESM-1-0-LL projects a total global deposition rate of 65.1 Tg-S yr^{-1} in 2020, increasing to 74.5 Tg-S yr^{-1} by 2100 under SSP5-8.5. These values are more similar to historical estimates. Two other models estimate total S deposition as 76.8 Tg-S yr^{-1} and 93.3 Tg-S yr^{-1} on average for 2000-2005 GEOS-Chem and University of L'Aquila Composition-Chemistry Model (ULAQ-CCM), respectively (Visioni et al., 2018). Total global sulfur deposition in 2010 was estimated at 88.8 Tg-S (Rubin et al., 2023). Total global sulfur emissions in 2015 were around 120 Tg-S (Aas et al., 2019) with deposition presumably slightly lower (Lamarque et al., 2013; Visioni et al., 2017). Dry SO_4^{2-} and dry SO_2 deposition will continue to decline globally under G6sulfur, SSP2-4.5, and SSP5-8.5, dropping sharply throughout the 2030s and 2040s and plateauing below 1950s levels by 2100 (**Figure 4.4**). The consistency of projections between scenarios and models demonstrates that injecting sulfate into the stratosphere does not fundamentally change the mechanisms influencing dry deposition on a global scale. Similarly, increasing the radiative forcing by increasing the CO_2 in the atmosphere compared to present day conditions (as under SSP5-8.5 or SSP2-4.5) does not influence the atmospheric chemistry and material properties of the dry sulfur particles settling out of the atmosphere.

Prior research shows that decreasing radiative forcing will decrease precipitation rates in many regions, therefore decreasing the rainout of particulate matter and resulting in longer lifetimes and more exposure to particulate matter remaining in the atmosphere under lower radiative forcing scenarios (Eastham et al., 2018). Precipitation is predicted to increase under all three scenarios (**Figure S4.3**) when compared to historical conditions, although under G6Sulfur precipitation will begin to decline again by 2050. Precipitation tends to remove $PM_{2.5}$ from the atmosphere so it follows that as the frequency of rainy days decreases in some places, even as the intensity increases, dry deposition will become the more dominant process. This means that the ratio of wet to dry deposition will steadily decline as precipitation increases. Wet deposition is more efficient at removing smaller aerosols so as rates of wet deposition decline, these smaller aerosols will tend to remain in the atmosphere longer.

Although the three ESMs disagree on the magnitude and trend in wet SO_4^{2-} under G6sulfur (**Figure 4.2**), they do agree that wet SO_2 will continue its current decline. Similarly, all three ESMs project a fundamental shift in seasonal SO_4^{2-} deposition where, even as precipitation increases from May to October, deposition decreases. This trend would make sense for dry deposition; as precipitation increases, more particles are rained out and so there is less dry deposition. But for more wet deposition to occur even as precipitation decreases shows that there is a process – in this case SAI – continually adding SO_4^{2-} to the system.

The three models have different features included in the simulated stratosphere and aerosol transport and deposition. The deposition patterns by latitude (**Figure S4.4**) demonstrate that the amount of SO_2 remaining in the stratosphere varies by injection scheme. All three models have a peak in deposition at 0º, 45º, and −45º, but the magnitudes vary by model and by time period, with different latitudes experiencing either steady increasing or decreasing deposition throughout the century. This is likely because a) the amount of SO_2 needed to reach the AOD necessary to cool the planet varies between models due to different SO_2 to sulfate conversion rates (Visioni et al., 2023) by as much as 10 Tg/year, and b) even though SO_2 is supposed to remain in the stratosphere as long as possible, it will inevitably eventually precipitate. Additionally, the injection altitude will impact stratospheric heating and result in temperature and precipitation differences between models. A large part of the uncertainty in SO_4^{2-} is due to differences in the aerosol chemistry in each model, specifically the SO_2 to SO_4^{2-} conversion rate (Visioni et al., 2023).

This is because of the way solar reduction is treated in the three ESMs. All ESMs reach SSP2-4.5 by the end of the century, but their approaches differ (Simone Tilmes et al., 2022). They begin in 2020 with SSP5-8.5 emissions and then a sulfate aerosol optical depth (AOD) is added to reflect sunlight and cool the planet to reach SSP2-4.5 levels of radiative forcing. UKESM1-0-LL injects SO_2 uniformly between 10º N and 10º S between 18 and 20 km of altitude and across a single longitudinal band (0º). CESM2-WACCM injects SO_2 at the equator at an altitude of 25 km. CNRM-ESM2-1 uses an input dataset from a different GeoMIP experiment (G4SSA) to prescribe the aerosol optical depth distribution. The UKESM-1 model adjusts the AOD every decade whereas CESM2-WACCM and CNRM-ESM2 adjust every year.

This analysis of emissions and deposition by ecoregion demonstrates that the type and location of ecoregion will determine whether it receives more sulfur deposition under G6 Sulfur compared to climate change under either SSP2-4.5 or SSP5-8 (**Figure 4.3**). Visioni et al. (2020) write that according to CESM1-WACCM projections, more deposition will occur in pristine areas under G6 Sulfur compared to the historical period as long-range transport relocates the particles away from the site of emissions to mid- and high- latitudes. This poses a risk to ecoregions that are particularly sensitive to fluctuations in sulfur levels and may not be able to survive rapid changes. Critical loads are the threshold of atmospheric deposition below which ecological harm does not occur for any given ecosystem or species (Nilsson, 1988). Beyond the critical load for an ecosystem, acidification and eutrophication will occur and important biogeochemical cycles will be impacted (Driscoll et al., 2001; Galloway, 1995; Lanning et al., 2019). In US forests, the critical load for sulfur deposition can be calculated for lichen and used as an indicator of overall forest health, because lichen is particularly sensitive to air pollution

(Geiser et al., 2021; McMurray et al., 2021). One study calculates this value to be 2.7 kg S ha^{-1} y^{-1} for forested ecosystems in the US (Geiser et al., 2021), or 8.56×10^{-11} kg S/m^2s. By this measure, the only ecoregion annual averages below the critical load under both G6Sulfur and SSP2-4.5 are deciduous needleleaf forests for 2020-2100 and Croplands/Natural Vegetation Mosaic for 2061-2100. Under SSP5-8.5, the ecoregions below the critical load are deciduous needleleaf forests for 2020-2100 and Croplands/Natural Vegetation Mosaic for 2081-2100. While not all species are not as sensitive to sulfur deposition as lichens, and there is a large range in both critical loads and uncertainty in critical loads by species, forest type, and underlying soil (X. Ge et al., 2023; Pavlovic et al., 2023), the exceedance in so much of the world is concerning. It is also important not to compare a climate intervention scenario to the current climate but rather to other possible futures to understand the risks of different global actions. When compared to SSP2-4.5, G6sulfur SO_4^{2-} deposition does not decrease as quickly and in some ecoregions begins to rise again by the end of the 21st century. Emissions, on the other hand, are lower and drop faster. When compared to SSP5-8.5, emissions and deposition tend to be lower across the board, although, again, in several ecoregions, SO_4^{2-} deposition will be higher by the end of the century. These results suggest that for most of the world, both SSP2-4.5 and SSP5-8.5 are associated with lower deposition by the end of the century. Nevertheless, in the near future, the opposite is true, meaning that benefits (strictly defined as lower sulfur deposition to sensitive ecosystems) from SAI will be concentrated in the next 20 years. One important note with my analysis is that these ecoregions will likely not be located in the same locations by the end of the century due to climate change and land use change (D. Wu et al., 2015).

SO_2 emissions are higher than deposition under all three scenarios (**Figure 4.3**) but SO_4^{2-} deposition is higher than SO_4^{2-} emissions due to the atmospheric chemistry taking place as SO_2 is transformed into sulfate. Under SSP2-4.5 and SSP5-8.5 sulfate deposition decreases over time as SO_2 and sulfate emissions decrease. Even so, because G6Sulfur involves injecting sulfate directly into the stratosphere, sulfate deposition stays remarkably constant from 2015 to 2100. The fact that it does not increase rapidly or in sharp increments means that much of the injected sulfate is staying in the atmosphere to reduce radiative forcing, as intended. However, not all of it is, meaning these injections will have to continue throughout the whole time period to maintain the same level of radiative forcing impact.

The difference in location between emissions and deposition in future scenarios (**Figures 4.3**, **S4.5**) highlights the role of long-range transport in distributing sulfur from source to sink (Fisher, 1975). Much of the projected decline in both deposition and emissions is happening between the 2020–2040 time period and the 2041–2060 period. While the drop in emissions is quick, the impacts are spread between multiple ecoregions such that, with the exception of mixed forest and open shrublands, most ecoregions experience a steady decrease throughout the century. However, it is not yet known whether even this relatively slow change is tolerable by the species that are either suddenly now not receiving enough sulfur or, in the case of mixed forest and open shrubland, experience a sharp decline and then a sharp and almost equal increase within the span of 40 years. If SAI were terminated early and unexpectedly, the sulfur deposition would adjust within a year or two to the levels projected by the relevant SSP, commensurate with the level of CO_2 in the atmosphere. In some cases, this could be catastrophic.

According to the UKESM-1-0-LL projections for different ecoregions, both deciduous needleleaf forests will experience a steep spike in sulfur emissions while woody savannas experience a spike in sulfur deposition under G6 Sulfur when compared to SSP2-4.5 (**Figure 4.3**). This does not happen with the CESM-WACCM results. These ecoregions are mapped in **Figure S4.6. Figures S4.8.** and **S4.9** shows the change in precipitation expected throughout the 21st century in various ecoregions for both the CESM2-WACCM and UKESM-1-0-LL model projections; precipitation alone is not enough to account for such deposition spikes. The G6 Sulfur scenario uses SSP5-8.5 land use but transitions to SSP2-4.5 precipitation and temperature by the end of the century, causing a mismatch between ecoregion and the associated climate regime. This causes a large difference in some ecoregions that are particularly sensitive to precipitation in the UKESM-1-0-LL results.

While modeling with CMIP5 ensembles suggests reductions in precipitation in many regions from an SAI scenario (W. Cheng et al., 2019; Simpson et al., 2019), recent work with CMIP6 models points out that the precipitation effects will strongly depend on the strategy and magnitude of the climate intervention (Simone Tilmes et al., 2020); my results show an overall slight increase in precipitation (**Figure S4.3**). This suggests that the cooling effect of SAI is not enough to entirely restore pre-industrial precipitation regimes in all regions as local climate variability may mask the impact of SAI (P. Irvine et al., 2019; P. J. Irvine & Keith, 2020; Tye et al., 2022). The new patterns of precipitation in many regions may also impact nitrogen deposition and therefore carbon sequestration and nutrient availability for croplands. As of yet, no G6 Sulfur models include enough variables to determine if this is the case.

It should be noted that currently nitrogen is not included in the GeoMIP models so the effects of SAI on deposition do not include any interaction with the nitrogen cycle. Models would more closely capture reality if they were to include nitrogen deposition, particularly in regions that are known to have high emissions that will likely continue to increase (Sun et al., 2022). There is also no sulfur transport from fires.

Past work has shown that it is feasible to replicate injection strategies between models producing similar temperature responses (Visioni et al., 2023). Coordinating such efforts to include a thought-out strategy for temperature targets and injection latitudes would greatly help with comparability between future scenarios and a better understanding of the risks and benefits of SAI.

4.7 Conclusions

Although controversial, SAI is a technologically feasible method of buying time for the world to slow down climate change. As such, it is important to evaluate the climate risks and human and environmental impacts of enacting this strategy globally. This work evaluates sulfur deposition under G6sulfur and compares the projections with SSP2-4.5 and SSP5-8.5 scenarios. Our results demonstrate that the injections required to maintain G6 Sulfur conditions and mitigate warming will have non-negligible impacts on sensitive ecoregions when compared to both SSP2-4.5 and SSP5-8.5. While dry deposition will continue to decline under all 3 future scenarios, the ratio of wet to dry deposition will change under G6 Sulfur, especially on a seasonal basis as more deposition occurs even in historically drier seasons. And, importantly, the benefits from SAI are concentrated in the near future. We also point out that there are large discrepancies across models and injection strategies, meaning that sulfate deposition will depend on which strategy is chosen as well as the stratospheric dynamics and chemical processes that differ between models. This overlapping area of uncertainty contains a broad range of outcomes that is hard to sample, especially when including other interactions such as nitrogen-sulfur interactions, fire inputs, and stratosphere-troposphere interactions.

Chapter 5 Downscaling Methods Accurately Predict Heat Wave Risk in a Changing Climate

5.1 Introduction

As the Intergovernmental Panel on Climate Change (IPCC) 6th Assessment Report states, hot extremes such as heat waves will become more intense, more frequent, and lengthier due to climate change (Balbus et al., 2016; Coumou & Rahmstorf, 2012; Gao et al., 2012; Pfleiderer et al., 2019; Seneviratne et al., 2021). The societal disruption caused by heat waves exacerbates a looming health crisis driven by climate change, especially for vulnerable segments of the population – the youngest, the oldest, and the homeless (Peng et al., 2011; Philip et al., 2021). Heat waves can cause a range of health impacts: heat stress, heat exhaustion, heat stroke (Arbuthnott & Hajat, 2017), and increased risk of heart attacks, strokes, and other cardiovascular diseases (NIH, 2022; US EPA, 2016). Additionally, heat waves can cause significant financial loss from power outages and disruption to public infrastructure (Langlois et al., 2013; Mazdiyasni et al., 2017). However, while the impact of heat waves is clear (World Health Organization, 2022), the specific risks of future heat waves to the US population on a regional scale are not yet well quantified.

To study how heat waves may evolve in the future, projections made by global climate models (GCMs) provide physics-based insights. The Coupled Model Intercomparison Project Phase 6 (CMIP6) coordinates the latest generation of GCM experiments worldwide using common protocols, climate forcings, and output formats to provide intercomparable future climate predictions (Eyring et al., 2016). O'Neill et al. (2016) described the design of CMIP6 emissions scenarios that combine a Representative Concentration Pathway (RCP) with radiative forcing levels between 1.9 and 8.5 W/m^2 and a Socioeconomic Development Pathway (SSP 1-5). Among the scenarios, we consider the "worst-case" SSP5-8.5 to investigate the upper bounds of what the US could experience. RCP8.5 has been used in other studies to investigate potential climate change impacts. For instance, based on Community Earth System Model (CESM) and historic heat wave distribution, heat waves are projected to be 3.5-6.4 times more frequent by the late 2050s under RCP8.5 (Gao et al., 2012; NCAR & UCAR, 2022; Riahi et al., 2011; J. Wu et al., 2014). However, this is likely an underestimation since the reference period to calculate heat wave probability was 2002–2004, a very short and recent timeframe well after anthropogenic climate change had already modified the climate, and it relied on results from only one GCM.

Additionally, the raw spatial resolution of GCMs is coarse and cannot resolve fine-scale processes to support regional (e.g., state-level and county-level) risk assessment and decision-making (Hewitson & Crane, 1996). Suitable downscaling techniques, either dynamical or statistical, are required to refine the projection at a finer spatial resolution. Statistical downscaling uses observations of the modeled phenomenon during a reference period to build a statistical relationship and then apply it to future events (Lei Zhang et al., 2020). It is computationally inexpensive and widely used but limited only to variables with long-term historic observations. It also relies on the premise that the relationship between observed and modeled events will remain unchanged in the future, which may not hold as climate change disrupts previously consistent processes (Rastogi et al., 2022). Dynamical downscaling uses regional climate models to incorporate the effects of climate processes with respect to future emission scenarios to estimate local impacts. It is more computationally intensive and requires several sub-daily GCM output. Using a new dataset (Rastogi et al., 2022) that provides both statistically and dynamically downscaled CMIP6 outputs, we explore how regional heat waves are projected in the US by the latest GCMs and the differences due to the choice of downscaling method.

The IPCC defines a heat wave as an extreme weather event associated with climate change (Intergovernmental Panel on Climate Change, 2012). There are numerous ways to quantify heat waves according to the research purpose and domain (European Drought Observatory, 2018; Langlois et al., 2013; Lavaysse et al., 2018; Mazdiyasni et al., 2019; J. Nairn et al., 2009; J. R. Nairn & Fawcett, 2015; Raei et al., 2018; Zuo et al., 2015). The Heat Wave Duration Index (HWDI) defines a heat wave as the total period greater than five consecutive days with a maximum temperature greater than 5º C above the historical normal daily maximum temperature value (Frich et al., 2002). While it is a useful approach for exploring deviations from normal values, a fixed threshold is not applicable in all regions (Kiktev et al., 2003). The Heat Wave Magnitude Index (HWMI) defines a heat wave as at least three consecutive days where the daily maximum temperature exceeds the 90th percentile threshold of the average of a 31-day reference window during 1981-2020 (Russo et al., 2014). Researchers used a similar definition to analyze heat wave occurrences with varying numbers of consecutive days, temperature scales, thresholds, and reference windows (Fischer & Schär, 2010; M. Luo & Lau, 2020; Perkins & Alexander, 2013). Because the length of the reference window and the percentile threshold can easily be changed, we use the HWMI to reach a more comprehensive view of future heat waves by varying the percentile threshold and reference window time frame.

While we do not explicitly focus on winter heat waves in my index comparison, I still include them in my analysis rather than limiting my work to the more commonly studied summer heat waves. Because winter heat waves (or "warm spells") receive less attention compared to summer heat waves (Staddon et al., 2014), the negative side effects of warm winters can be underestimated. Biogeochemical and carbon cycles can be interrupted by these warm spells and this results in increased nitrogen leaching (Kreyling et al., 2015) and carbon loss from respiration (Z. Liu et al., 2020), which feeds into a positive feedback loop of worsening climate change. Additionally, increased glacial ablation (where warmer weather causes a rain-on-snow melting event) caused by heat waves can influence the yearly snow accumulation of the highly seasonal precipitation regime, which is a challenge for farming domestic food staples that rely on a steady water supply (Brás et al., 2021; Colucci et al., 2017; Dierauer et al., 2019; Watanabe et al., 2020).

This research aims to understand how regional heat waves, an urgent climate hazard, may evolve across the Conterminous US (CONUS) in the near-term future using a newly released dataset with downscaled CMIP6 projection. Through the comparison of heat wave indices derived from gridded meteorological observations, raw and downscaled CMIP6 GCMs, we evaluate the differences between projections due to the choice of downscaling method through the lens of heat waves. My work emphasizes the importance of fine spatial and temporal resolution for regional-scale projections and demonstrates that dynamical downscaling, though computationally intensive, can lead to more reliable results for the purpose of human health, ecosystem, crop damages, and other regionally focused impact assessments.

5.2 Methods and Data

Three gridded meteorological observation datasets are used in this study. They include:

(1) Daymet: Daymet version 4 is available through Oak Ridge National Laboratory (ORNL) Distributed Active Archive Center (DAAC) (https://daymet.ornl.gov/). It provides 1-km horizontal resolution daily gridded surface meteorological variables in North America from 1980 until the present. Daymet is produced by assimilating ground-based observations through multivariate spatial regression (M. M. Thornton et al., 2020).

Daymet has served as the reference meteorologic observation for both dynamically and statistically downscaled CMIP6 GCMs used in this study.

(2) NClimGrid: National Ocean and Atmospheric Administration (NOAA) Daily U.S. Climate Gridded Dataset (NClimGrid) aggregates measurements from the Global Historical Climatology Network-Daily (GHCN-Daily) dataset to provide daily gridded meteorological observations at 1/24° horizontal resolution across the CONUS. Similar to Daymet, the gridded dataset is also created through interpolation between station locations and over differing elevations (Vose et al., 2014).

(3) PRISM: The Parameter-elevation Relationships on Independent Slopes Model (PRISM) is another widely used gridded meteorological observation dataset. The publicly available PRISM provides 1/24° horizontal resolution daily gridded surface meteorological variables in the CONUS from 1980 until the present (Daly et al., 2008). It is available from the PRISM Climate Group at Oregon State University.

It should be noted that while these gridded meteorological observation datasets were derived from station-based observations (such as GHCN-Daily), given their different algorithm, local differences can be expected. For instance, the differences among Daymet and PRISM and other commonly used gridded datasets have been compared in prior studies(Behnke et al., 2016; Timmermans et al., 2019). To avoid biased results driven by a specific dataset, we hence calculated heat wave indices from all three datasets for the purpose of model evaluation and comparison.

For climate projections, six CMIP6 GCMs under SSP5-RCP8.5 (**Table S5.1**) were selected given their model performance (Ashfaq et al., 2022) and availability of 6-hourly data to support dynamical downscaling. Dynamical downscaling was done using the fourth version of the Regional Climate Model system (RegCM4) which relies on physics-based models and provides a large suite of physically consistent variables (Coppola et al., 2021), and it refines the horizontal resolution from GCM's original resolution (>150km) to 25km across the CONUS (Rastogi et al., 2022). A daily bias-correction was then performed on RegCM4 output using Daymet observations and it further refines the spatial resolution from 25km to 1/24º (~4km). For comparison, statistical downscaling was done using Double Bias Correction Constructed Analogs (DBCCA) which is a method that leverages empirical relationships between global climate models and observations (Maurer & Pierce, 2014; Rastogi et al., 2022; Werner &

Cannon, 2016). It provides an output at the same 1/24º (~4km) horizontal resolution for inter-comparison.

The entire CONUS was divided into nine climate regions as defined by the National Center for Environmental Information (NCEI, https://www.ncei.noaa.gov/, **Figure S5.1**). We calculated an ensemble mean of the six CMIP6 models (**Table S5.1**) using raw and downscaled outputs for both historical (1980–2019) and near-term future (2020–2059) periods for the entire study area. We then calculated the heat wave magnitude index (Russo et al., 2014) for each of the 9 regions by year and used the daily maximum temperatures during the 40-year reference period to calculate the 85th, 90th, 95th, and 97.5th percentiles with 11-, 15-, and 31-day windows. Each heat wave event was only classified as such if it lasted at least 3 consecutive days. We also calculated a multi-model mean for humidity and minimum temperature by year for each downscaling approach.

We also performed a Student's t-test to compare the difference in average daily maximum temperature in by season and downscaling method for the future time period (2020-2059) compared to the reference period (1980–2019).

5.3 Comparison with Historical Models and Observations

Because this work focuses on fine-resolution data for a regional approach, the US was divided into 9 climate regions (**Figure S5.1**), and each was evaluated separately. Comparing historic heat waves during the baseline period of 1980–2019 to projected future heat waves from 2020–2059 demonstrates that there are important regional variations as well as the expected differences between downscaling approaches (**Figure 5.1**). Compared to historical averages, the statistical downscaling approach using the DBCCA method projects slightly higher HWMI values than the dynamical downscaling approach using RegCM4 especially at the lowest percentile threshold (85%) (**Figure 5.1A**). This is particularly noticeable in the Ohio Valley (OV), Northern Rockies (NR), and Upper Midwest (UM), where the DBCCA ensemble projects an increase of ~3 HWMI, and the RegCM4 ensemble projects an increase of closer to 2. The South (S) is projected to have little change in future HWMI according to the DBCCA ensemble at all threshold levels. At higher percentile thresholds (95%, 97.5%), both DBCCA and RegCM4 ensembles project little increase in 2020–2059 in HWMI (~1) from the historical reference period. According to Russso et al. (2014), who developed the index, a normal heat wave is defined as HWMI ≥ 1, a

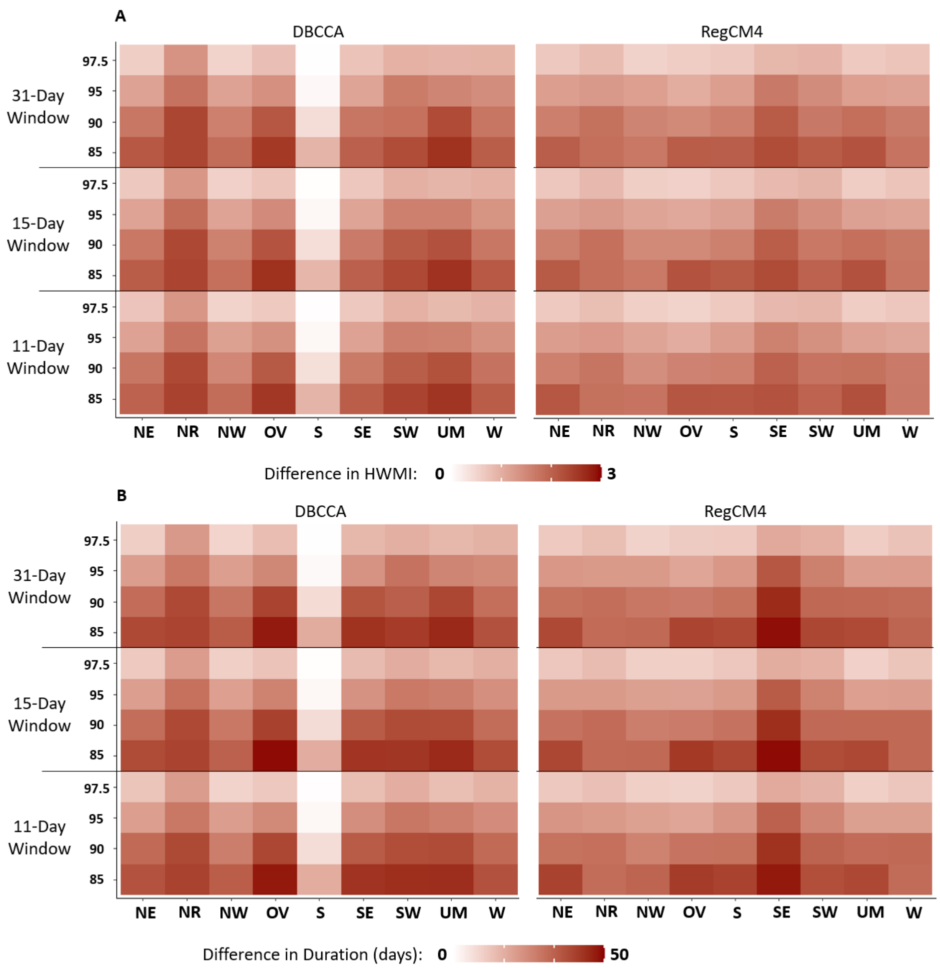

Figure 5.1 A comparison of historic heat waves during 1980–2019 to projected heat waves from 2020–2059. (A) HWMI by region for 2020–2059 for DBCCA and RegCM4 compared to historical averages (1980–2019). (B) The duration of the greatest heat wave event by region 2020–2060 for DBCCA and RegCM4 compared to historical averages (1980–2019). (C) The start day of the greatest heat wave event by region for 2020–2059 for DBCCA and RegCM4 compared to historical averages (1980–2019). (NE: Northeast, NR: Northern Rockies, NW: Northwest, OV: Ohio Valley, S: South, SE: Southeast, SW: Southwest, UM: Upper Midwest, W: West.)

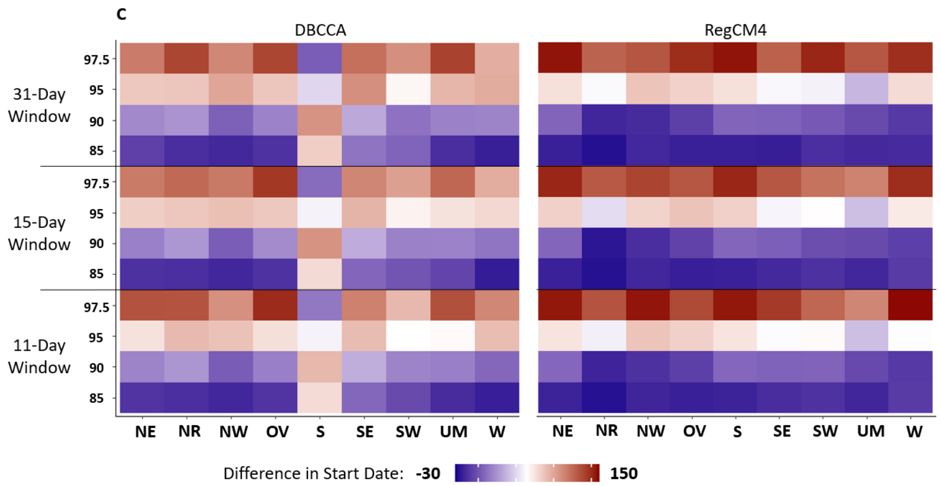

Figure 5.1 (Continued)

moderate heat wave is HWMI ≥ 2, a severe heat wave is HWMI ≥ 3, and an extreme heat wave is HWMI ≥ 4.

The change from the reference period in the duration of the greatest heat wave event of the year also varies by region and by downscaling method (**Figure 5.1B**). The greatest heat wave event is defined as the longest-lasting and most intense heat wave of the year. According to the RegCM4 ensemble, the change in heat wave duration in the Southeast (SE) will be close to 50 days at the 85% threshold but closer to 25 days in the Northern Rockies (NR), Northwest (NW), and West (W). This regional pattern is not seen in the DBCCA projections. Instead, the South (S) will have little change in the duration of the greatest heat wave event, but the Ohio Valley (OV) will experience 50 more days per year at the 85% threshold.

At the lower thresholds (85%, 90%), the DBCCA and RegCM4 ensembles project an earlier start date of the greatest heat wave event in a year compared to the reference period (**Figure 5.1C**). A start date of 30 days earlier (such as the Northwest (NW) from the DBCCA ensemble and the Northern Rockies (NR) from the RegCM4 ensemble) represents a shift to earlier and hotter seasons. However, at the highest thresholds (95%, 97.5%), both the ensembles project a change of 150 days, or about 5 months later. This is not a seasonal shift but a fundamental regime change, meaning that the start date of the greatest heat wave is shifting from winter “warm spells” during the reference period to summer heat waves. However, these warm winter spells are not as long or intense as the summer heat waves because they are no longer counted at higher thresholds. The only region not demonstrating this pattern is the South (S), from the DBCCA ensemble. Instead, the pattern is reversed, with the lower thresholds associated with a 1–2-month delay in start date and higher thresholds associated with a 10–15 day earlier start date. Note that this is the start date of the hottest and longest-lasting heat wave of the year, not the start date of the year's first heat wave, and the number of heat waves in a year is accounted for with the HWMI.

For the purpose of model validation, the CMIP6-DBCCA and CMIP6-RegCM4 ensembles are compared to three gridded observational datasets (Daymet, NClimGrid, and PRISM) for the historic reference period of 1980–2019 (**Figure 4.2**). CMIP6-Raw is the original 6-model ensemble remapped at 1^{o} resolution using bilinear interpolation with no downscaling. In **Figure 4.2A**, all data were regridded to a 1^{o} resolution, and in **Figure 4.2B**, the model projections are compared directly at their original resolution (**Table S4.2**). In the Southwest (SW), Ohio Valley

Figure 5.2 Maximum daily temperature in the US, from 1980–2019. A) Each model or observational output was regridded to the CMIP6 resolution (1ºx1º). B) Each model or observational output was kept at its original resolution.

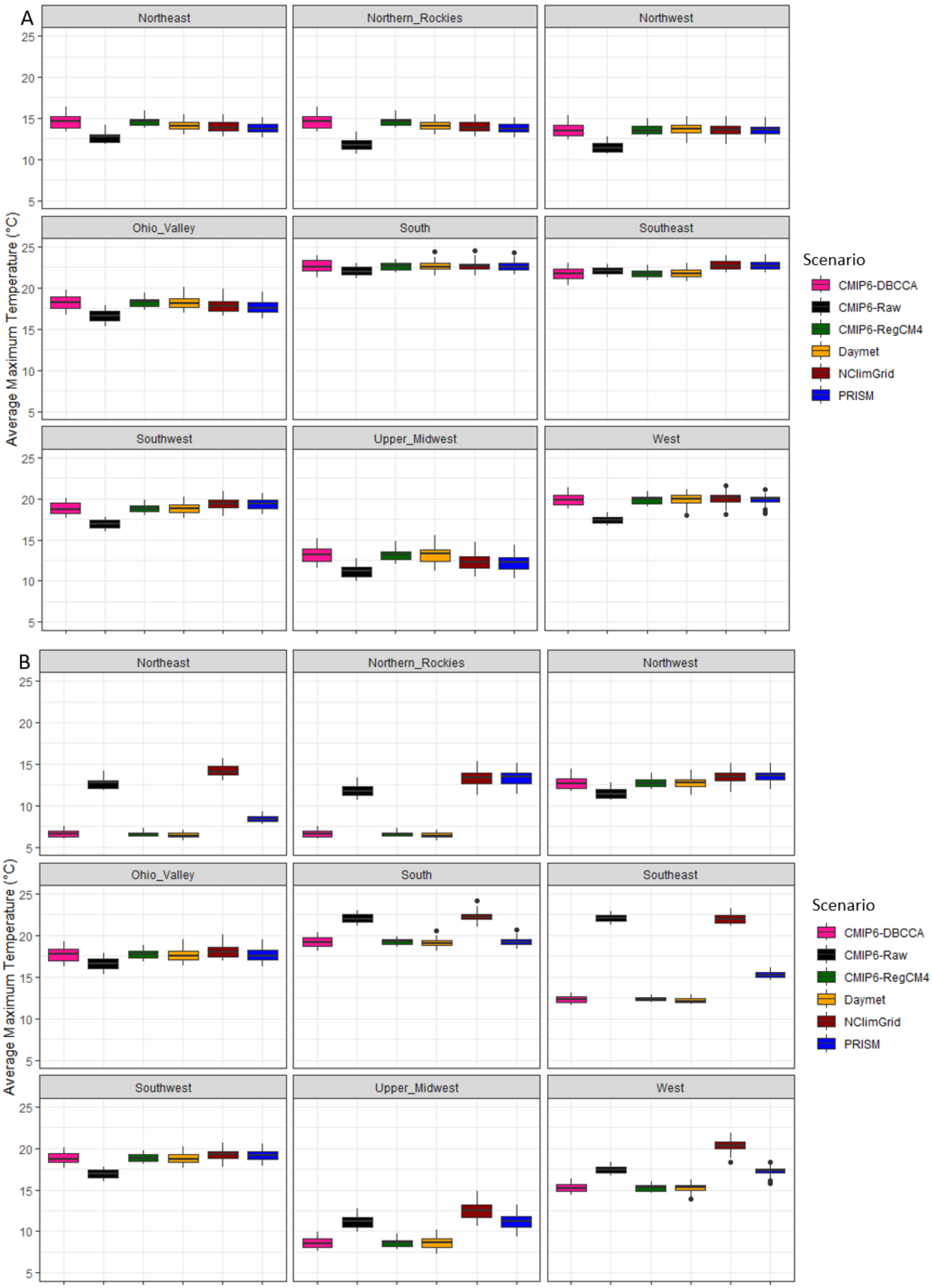
A
Northeast
Northern_Rockies
Northwest
Ohio_Valley
South
Southeast
Southwest
Upper_Midwest
West
Average Maximum Temperature (°C)
25
20
15
10
5
Scenario
CMIP6-DBCCA
CMIP6-Raw
CMIP6-RegCM4
Daymet
NClimGrid
PRISM
B
Northeast
Northern_Rockies
Northwest
Ohio_Valley
South
Southeast
Southwest
Upper_Midwest
West
Average Maximum Temperature (°C)
25
20
15
10
5
Scenario
CMIP6-DBCCA
CMIP6-Raw
CMIP6-RegCM4
Daymet
NClimGrid
PRISM

(OV), and Northwest (NW), aggregation does not change that CMIP6 projects significantly lower maximum temperature estimates than the other model outputs and observations ($P<0.05$). In the Northeast (NE), Northern Rockies (NR), West (W), South (S), and Upper Midwest (UM) the CMIP6 average maximum temperature is significantly higher than the original resolution DBCCA, RegCM4, and Daymet values but is significantly lower than the regridded values ($P<0.05$). In the Southeast (SE) the CMIP6-Raw ensemble mean at 1^{o} resolution is significantly higher than the original resolution DBCCA, RegCM4, and Daymet means whereas aggregation to 1^{o} shifts the DBCCA and RegCM4 means to be significantly lower than the CMIP6-Raw ensemble mean and the NClimGrid and PRISM means to be significantly higher ($P<0.05$). **Table S5.2** lists the original horizontal grid spacing before all the datasets are regridded to 1^{o} for comparison in **Figure 5.2A**.

5.4 Dynamical versus Statistical Downscaling

The HWMI is driven by maximum temperature, by definition (see Methods). The projected annual maximum temperature for each downscaling ensemble is shown in **Figure S5.3**. Notably, the trends and year-to-year variation are very similar, although the DBCCA tends to project slightly higher temperatures in the 2050s. Looking at annual averages over the entire CONUS, it is not immediately apparent that the two approaches are fundamentally different. However, at a seasonal scale, there are definite spatial differences (**Figure 5.3**). While both the DBCCA and RegCM4 downscaled ensembles demonstrate increased warming across all seasons, the DBCCA ensembles for spring, summer, and fall are markedly different from the RegCM4 projections. The DBCCA spring and summer projections appear to be overestimating the increase in 2050s temperatures compared to the RegCM4 projections, with greater warming in the northern and western US. In the fall, however, RegCM4 projects greater warming by the 2050s across much of the northern US.

Figure 5.4 compares future heat wave characteristics in dynamical and statistical downscaling ensembles using 4 different percentile thresholds and 3 different reference windows. When averaged annually across the entire US, both RegCM4 and DBCCA reveal similar patterns of increasing intensity and duration of heat waves in the near future. The HWMI will increase steadily for all percentile thresholds and reference windows (**Figure 5.4A**). The longer reference timeframe of 31 days has no noticeable smoothing effect on the year-to-year variation in HWMI compared to the shorter reference windows.

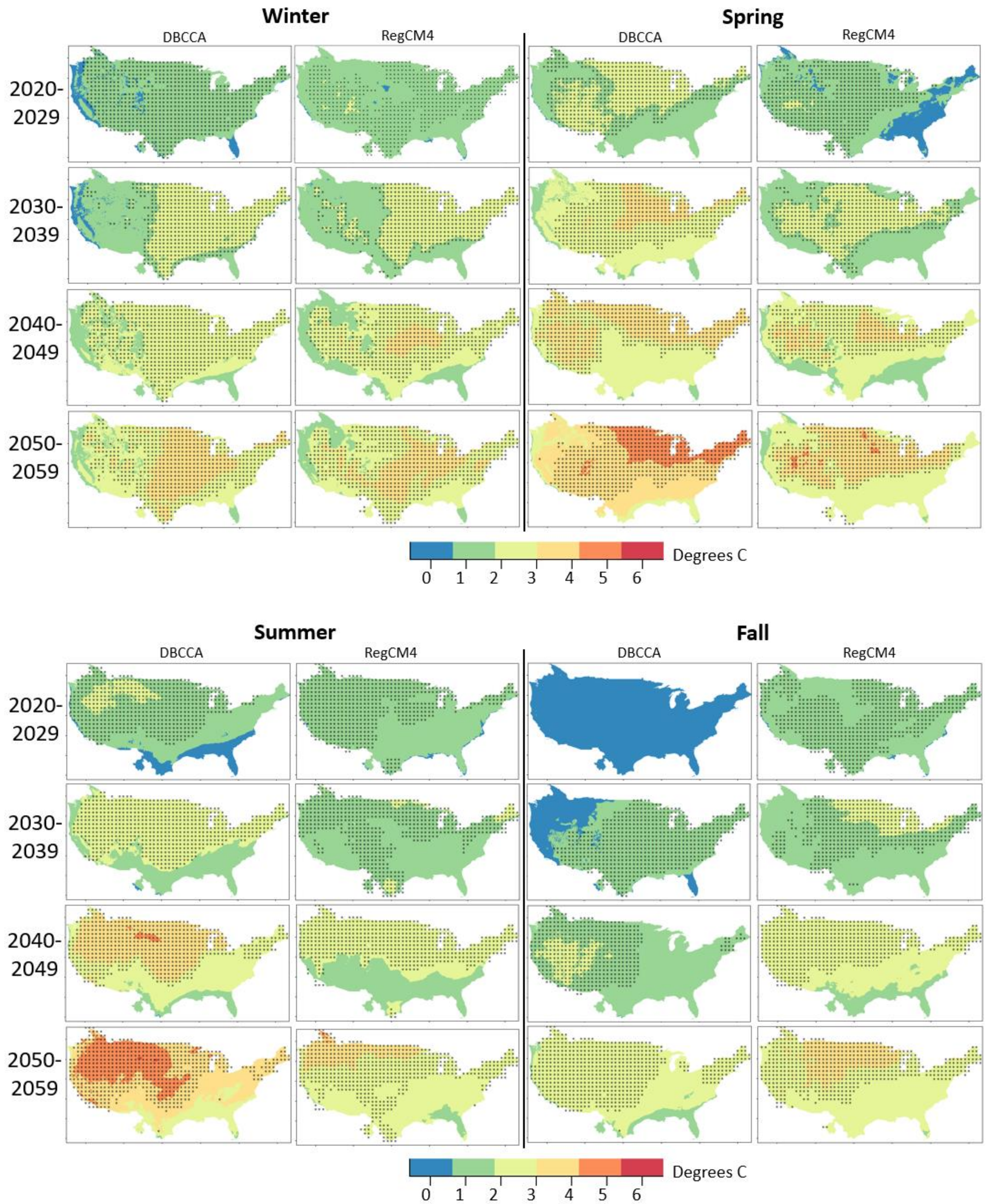

Figure 5.3 Seasonal maximum temperature difference by decade. The difference in average daily maximum temperature in degrees C by season for each future period and downscaling method compared to the reference period of 1980–2019. Stippling indicates statistical significance at the 95% confidence interval under a one-sample, two-sided Student's t-test.

Figure 5.4 Heatwave characteristics by percentile threshold and window. (A) HWMI by threshold and window in the US (2020–2059). (B) Predicted start day of the longest and hottest heat wave by threshold and window in the US (2020–2059) (The 97.5 percentile threshold has been removed for clarity, see Figure S5.2 for the full comparison). (C) Predicted duration of the longest and hottest heat wave by threshold and windows in the US (2020–2059).

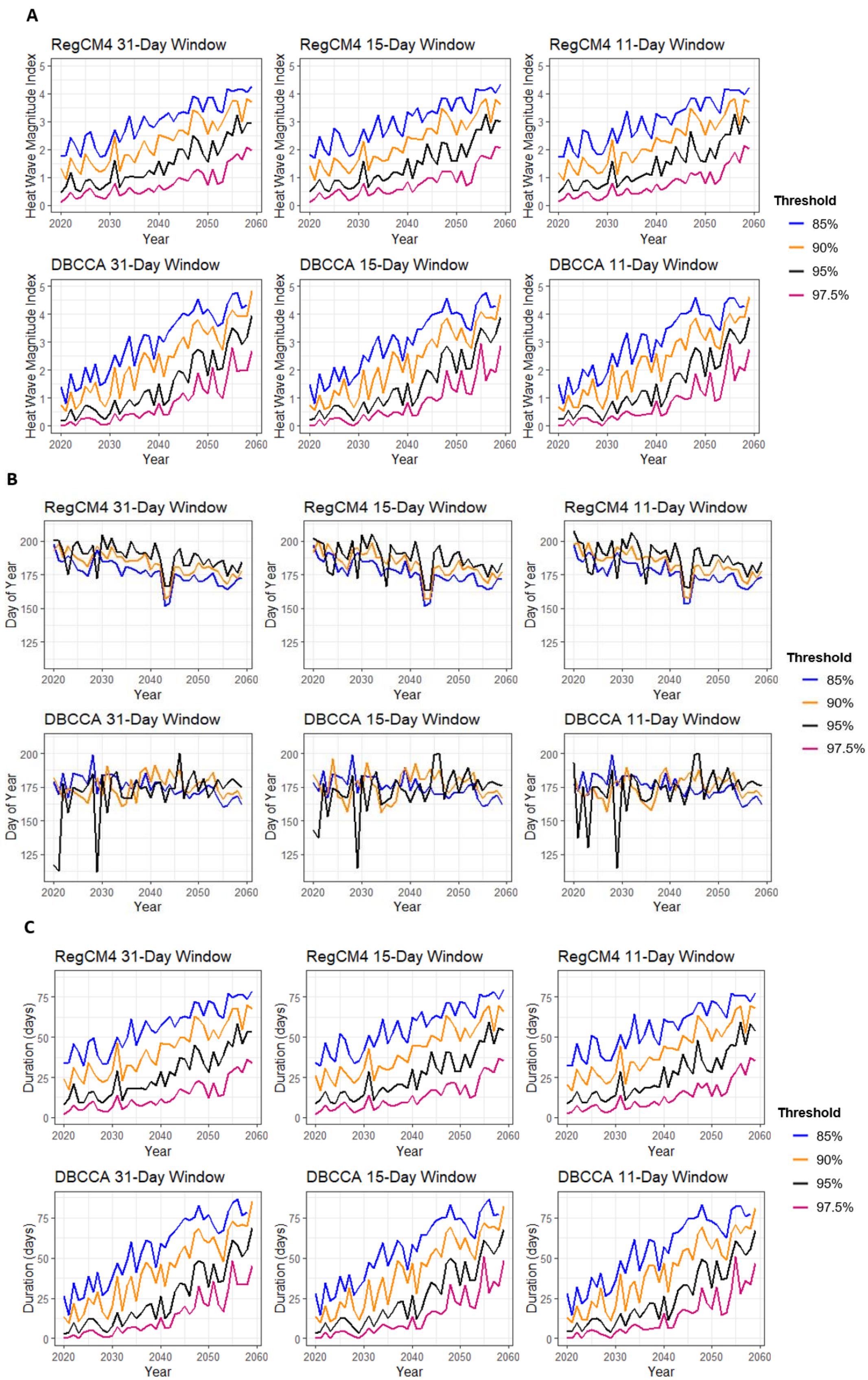
A
RegCM4 31-Day Window
RegCM4 15-Day Window
RegCM4 11-Day Window
DBCCA 31-Day Window
DBCCA 15-Day Window
DBCCA 11-Day Window
Heat Wave Magnitude Index
Year
Threshold
85%
90%
95%
97.5%
B
RegCM4 31-Day Window
RegCM4 15-Day Window
RegCM4 11-Day Window
DBCCA 31-Day Window
DBCCA 15-Day Window
DBCCA 11-Day Window
Day of Year
Year
Threshold
85%
90%
95%
97.5%
C
RegCM4 31-Day Window
RegCM4 15-Day Window
RegCM4 11-Day Window
DBCCA 31-Day Window
DBCCA 15-Day Window
DBCCA 11-Day Window
Duration (days)
Year
Threshold
85%
90%
95%
97.5%

According to the RegCM4 ensemble, the average start day of the longest and hottest heat wave event will occur earlier each year (**Figure 5.4B**). In 2020, the average start date across the US is around day 200 (mid-July), but by 2059, this date will shift closer to day 175 (late June), almost an entire month earlier. The DBCCA ensemble does not demonstrate this shift to earlier, more extreme temperatures. It projects more inter-annual variability, alternating between start dates in mid-April and June.

As the 97.5th percentile threshold (pink lines in **Figure 5.4C**) shows, even the most conservative threshold in both the RegCM4 and DBCCA ensembles predict a steady increase in the duration of the greatest heat waves from fewer than 10 days in the early 2020s to well over 30 days in the 2050s. Under the least conservative threshold, the 85th percentile threshold (blue lines in **Figure 5.4C**), there is a shift in the temperature regime in the US, where the greatest heat wave events will double in duration and last for more than two months.

Diurnal temperature range is an important indicator of climate change (Braganza et al., 2004) and is associated with various human health and environmental impacts (Huang et al., 2020; Whanhee Lee et al., 2020; Park et al., 2020, 2020). Studies have shown that the diurnal temperature range is decreasing (He et al., 2022; Whanhee Lee et al., 2020) with climate change and that increases in nighttime temperatures have a greater impact on human health than changes in daily averages. Hot nights are becoming more frequent and intense (Batibeniz et al., 2020). While both maximum and minimum temperatures are predicted to rise throughout the US during every season of the year (**Figures S5.3, S5.4**), the difference between maximum and minimum is not uniform (**Figure 5.5**). The RegCM4 ensemble projects a decrease in the diurnal temperature range from $6.82^{o} \pm 0.04^{o}$ C to $6.65^{o} \pm 0.04^{o}$ C. The DBCCA ensemble, however, projects an increase in the diurnal temperature range from $6.71^{o} \pm 0.05^{o}$ C to $6.91^{o} \pm 0.05^{o}$ C. The magnitudes of the trends in the diurnal temperature range are similar between the two ensembles, but the direction of change is the opposite.

5.5 Discussion

The RegCM4 and DBCCA ensembles and the three observational datasets of maximum temperature generally follow the same trend by region from 1980–2020 (**Figure 5.2**). The results suggest that the observations match the downscaled ensembles better than the CMIP6-Raw ensemble in these regions, highlighting the necessity of downscaling for the needs of impact

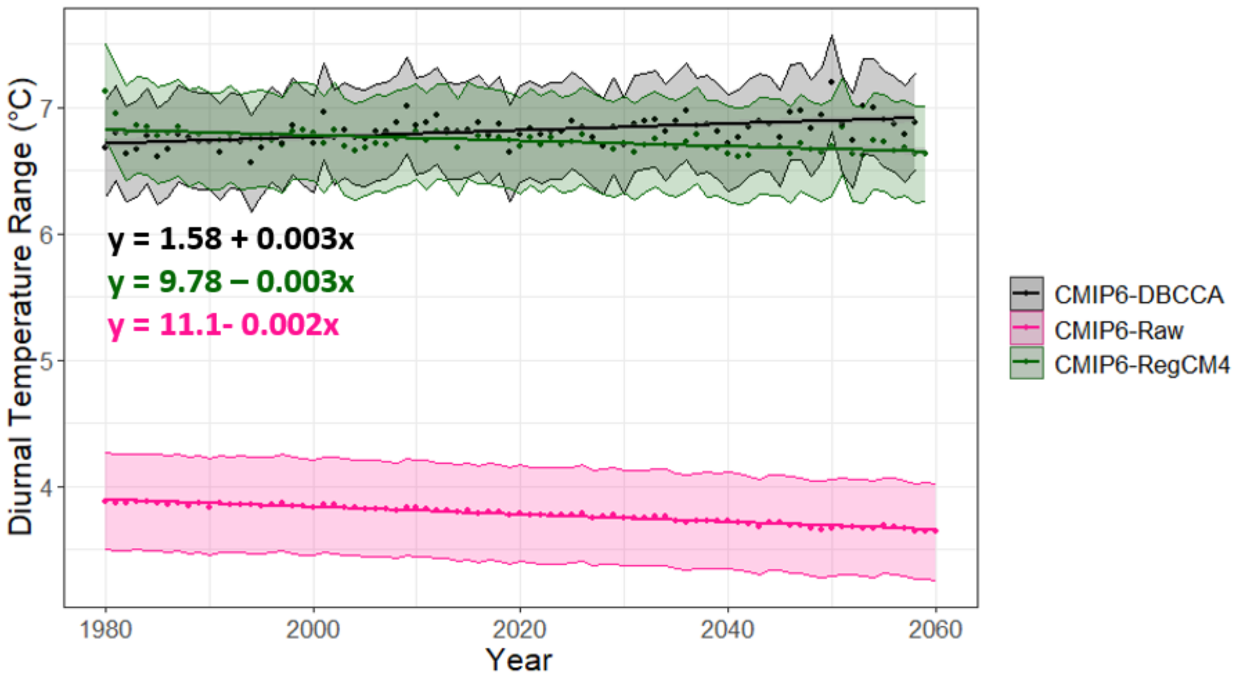

Figure 5.5 Diurnal temperature range over time. The difference between maximum and minimum daily temperature is averaged annually for the DBCCA and RegCM4 ensembles and the original resolution CMIP6 ensemble. The shaded area shows the standard error.

assessment. This is to be expected; the point of downscaling is to increase regional accuracy, and it is reassuring that both downscaling approaches match reference meteorology. However, looking only at annual averages over the entire US masks important regional and seasonal trends and leads viewers to conclude that statistical and dynamical downscaling produce similar results (**Figures S5.3, S5.4**). Instead, examining trends at a seasonal scale (**Figure 5.3**) demonstrates the importance of using dynamical downscaling for future climate projections whenever available, especially since seasonal mean temperature changes are the driving factor behind projected future heat waves (Argüeso et al., 2016). Using the original CMIP6 ensemble results to assess regional impacts and develop mitigations could mislead users and decision-makers. The DBCCA and RegCM4 ensembles produce estimates of regional temperature that are markedly different from the original CMIP6 outputs (**Figure 5.2**). The DBCCA ensemble results project that much of the western US will experience maximum daily temperatures 4-5^{o} warmer in the fall and spring than historical estimates, while the RegCM4 ensemble projects a 3-4^{o} increase over much of the CONUS (**Figure 5.3**). This is a large difference in a single season has important implications for the environmental events that are dependent on temperature such as false spring risk and other phenological indicators that capture risk metrics for ecological and economic damage (Wootten et al., 2024). Choosing statistical downscaling as a method here results in overly pessimistic conclusions about the impacts of heat waves under SSP5-8.5. Downscaling daily maximum temperature projections becomes more challenging under greater warming conditions, during the summer, and in some particular geographic areas such as regions with steep elevation changes (Dixon et al., 2016; Mendoza Paz & Willems, 2023). In fact, downscaling contributes substantial uncertainty to future climate estimates, particularly when projecting extremes, in regions with complex terrain, or where historical observations do agree (Lafferty & Sriver, 2023). These factors are all extremely relevant for calculating future heat wave risk, meaning that statistical downscaling is not sufficient to capture the nuances of regional-scale trends.

Figure 5.4 demonstrates that when comparing trends of future and historical warming, the threshold and reference window do not influence the slope of the trend; however, the threshold selected does impact the projected magnitude. The HWMI increases as the percentile threshold decreases because more heat wave events are counted. Even with the most conservative threshold (97.5%), both the DBCCA and RegCM4 ensembles predict at least a doubling of the duration of the greatest heat wave event in a year by the late 2050s under SSP5-8.5 (**Figure 5.4C**). That means that the probability of a heat wave lasting a month today, in the early 2020s, would be equivalent to the likelihood of a heat wave lasting over 2 months by the late 2050s. Such a projected change is unsustainable from a human health and ecological perspective, with both direct and secondary die-offs likely in affected ecosystems (Breshears et al., 2021). Even wintertime heat waves and mild winters in general, while not necessarily as hazardous to human health, can seriously disrupt ecological processes that rely on consistently cold winters (Colucci et al., 2017; Flanigan et al., 2020; Kreyling et al., 2015).

The pronounced interannual variability in projected heat wave characteristics (**Figure 5.4**) is likely due to the influence of both large and local scale conditions that form heat waves in different regions of the US, such as mid-latitude circulation anomalies or reduced maritime cool air advection off the west coast (Budikova et al., 2019; Teng et al., 2013; Z. Yang et al., 2019). However, the RegCM4 and DBCCA ensemble projections do not necessarily agree on the magnitude of this variation, or the overall trend in the underlying data (**Figure 5.5**). This difference in diurnal temperature range projections between downscaling techniques can be explained by statistical downscaling relying on fixed relationships and being unable cannot account for the future impact of increased warming, especially since it does not take into account local topography and land use (Jang & Kavvas, 2015). It has been shown that differences between statistical and dynamical downscaling methods are larger for future projections than the historical period (Walton et al., 2020).

The predicted trend for the diurnal temperature range from the RegCM4 ensemble is consistent with a global study evaluating CMIP5 models that projected a reduction in the average diurnal temperature range under RCP8.5, though not all models agreed on the sign or the magnitude of the change (Lindvall & Svensson, 2015). The DBCCA ensemble, however, predicts a current and future trend of the same magnitude but in the opposite direction (e.g., increasing diurnal temperature range). Both the DBCCA and RegCM4 ensembles project similar diurnal temperature ranges, much higher than that of the raw CMIP6 ensemble. My work demonstrates that model selection, timeframe, region, and the choice of downscaling technique can impact the magnitude and sign of results, leading to regionally varying conclusions (Ashfaq et al., 2016). In this case, dynamical downscaling is the more trusted method, but because it is time-consuming and computationally costly, it may not be available to all researchers. Choosing statistical downscaling instead would result in a completely different conclusion about the trend in the diurnal temperature range under SSP5-8.5. This result emphasizes the importance of caution, clarity, and domain-specific knowledge when communicating model results and uncertainty to non-scientists for use in policy and climate change adaptation work.

5.6 Conclusions

The association between heat waves and mortality, morbidity, and ecosystem stress is well-established. It has already been established that heat waves are increasing in frequency, intensity, and duration due to climate change. However, we investigate this trend on a regional scale using new fine-resolution climate data ensembles and compare two downscaling approaches to other commonly used meteorology products. We systematically investigate trends in US heat waves on a regional scale in the near future with two separate ensembles of dynamically and statistically downscaled models. We compare the model estimates to meteorological observations and assess the sensitivity of a heat wave index to four percentile thresholds and three reference timeframes. My work shows that the downscaling method, heat wave index, and temporal and spatial scale directly influence model estimates, although heat waves are projected to increase in magnitude and duration regardless of the index used for analysis. We demonstrate the importance of dynamical downscaling a fine spatial scale for regional insights into processes occurring on an intra-annual basis. My results emphasize the need for urgent preparations for a hotter future climate and the importance of state-of-the-science modeling techniques for fine-resolution, domain-specific climate projections.

Chapter 6 Mapping Long-Term Trends in Soil Organic Carbon with Machine Learning

6.1 Mapping Soil Organic Carbon

Soil organic carbon (SOC) is a critical element of the global carbon cycle because soil can be both a sink and a source of carbon emissions. Carbon is captured in the soil through litterfall, rhizodeposition, and root or rhizome death in the soil [1] and carbon is emitted due to disturbances such as fire, tilling, clearing vegetation, and erosion [1–3]. SOC greatly impacts microorganism abundance and soil health [4] and in turn is influenced by vegetation, temperature, and precipitation [5]. The global SOC pool is three times greater than that of above-ground vegetation [6] and because it is relatively easy to modify with human intervention such as land management practices [7], it will likely play an important role in mitigating climate change impacts [8]. In particular, industries wishing to decarbonize by replacing fossil fuels with biofuels need to complete life-cycle assessments of their new fuel type. This requires a deep understanding of how carbon is lost or gained in soils and how the influence of biofuel feedstocks impacts carbon cycling. For example, decarbonizing industries such as aviation require biofuel feedstocks; however, knowing where they can be grown to sequester carbon rather than release carbon is still a large unknown [9]. Decarbonizing aviation is an important step in reaching net-zero GHG and mitigating climate change and biofuels have an important role to play in controlling induced land-use change [10]. However, our understanding of soil carbon dynamics is poorly constrained because of the lack of complete parameterization of soil carbon stocks [1]. A substantial part of the uncertainty is the lack of spatially and temporally continuous maps of baseline SOC.

Based on long-term historical global land use changes, major SOC losses are associated with intensive agricultural practices and degraded grazing lands [11] and there are greater losses of SOC in boreal forests and SOC-rich soils due to warming [12]. However, in the US there are numerous conflicting maps of SOC and the differences in estimated SOC from these various studies and methodologies are greatest in lands that have a high SOC content, meaning the regions that are the greatest contributors to carbon sequestration are also the least well understood [13]. One issue is that the regional environment is extremely important in determining SOC formation, but in some places, the local climate has a much greater influence and this nonlinear relationship is not consistent across different ecoregions [14] meaning that the primary driver of carbon sequestration – land cover change, carbon dioxide levels, nitrogen deposition - can be different in different areas [15]. This is particularly important to get right because, otherwise, the expansion of biofuel crops could end up decreasing carbon sink capacity in newly planted lands [16].

Our work therefore aims to improve SOC baseline estimates in the US and investigate long-term trends in land use and climate change with the overall goal of improving our understanding of carbon cycling in complex environments. Although gridded estimates of SOC in the US do exist, the lack of explicit uncertainty quantifications and the large variation of SOC magnitude and distribution makes them challenging to rely on, especially for fine-resolution applications [17]. We use machine learning to overcome these challenges, and in particular, a comparison of machine learning techniques from the literature, rather than selecting a single technique that has been used in past approaches. We also break down SOC drivers by region and climate conditions to emphasize the spatial heterogeneity of SOC and the influence of historical conditions.

The Soil Survey Geographic Database (SSURGO) and the Digital General Soil Map of the US (STATSGO2) database provide soil property data for the majority of the USA. However, these measurements are not spatially or temporally continuous. The US Geological Survey (USGS) used SSURGO and STATSGO2 data to estimate SOC storage for a single year in 2009 [18]. While the USGS map covers the conterminous USA (CONUS), uncertainties are hard to estimate due to spatial extrapolation for regions with incomplete measurement coverage. Spatially continuous SOC estimates for the US from 1991-2011 are also available from NASA [19,20]. These gridded estimates were derived from field data and environmental variables using a machine learning approach: a random forest regression within a simulated annealing framework. However, this work does not extend to the present and the SOC estimates are mapped at a fairly coarse resolution (250 m).

Other efforts focused on mapping SOC have incorporated remote sensing techniques and machine learning to increase monitoring capacity and resolution and enable better representation of SOC fluxes [21]. Venter et al. used a machine learning workflow – a random forest algorithm – with imagery from NASA/USGS's Landsat 5, 7, and 8 satellites to map SOC stocks in South Africa [3]. Work in the Mediterranean region also relied on Landsat but instead used stochastic gradient tree boosting to predict SOC distribution across the landscape [22]. Tian et al. developed a different approach, using a random forest model to map soil erosion, an import influence on soil carbon pools, from environmental variables and the normalized difference vegetation index (NDVI) from the Moderate Resolution Imaging Spectroradiometer (MODIS), onboard NASA's Terra satellite [23]. A similar study with Landsat relied on regression kriging [24]. Recent work with ESA's Sentinel satellite demonstrates a reasonable capacity to predict and map SOC in bare soils [25,26]. In general, however, approaches that require bare soil are geographically limited due to the lack of ground-based observations or, in the case of hyperspectral imagery with bare soil require significant spectral preprocessing [27]. Research on the spatial and vertical distribution of SOC in Canadian soils relied on a random forest model and NDVI to create a map of SOC concentration [28]. Estimates of SOC with the US Department of Agriculture's Rapid Carbon Assessment (RACA) data using a random forest model demonstrate the potential for SOC stock prediction in forested lands [29]. Other work using RACA data compared gradient boosting, random forest, and extreme gradient boosting methods to predict SOC stocks across the US using earth system model outputs [30]. Work in Argentina predicted SOC stocks based on weighted averages of annual NDVI such that the current estimates were based on historical NDVI values [31]. One study in Brazil found that clay content helped predict the spatial distribution of SOC [32]. However, they relied on a single date of Landsat imagery which does not adequately reflect the dynamics of crop growth over time and thus their model cannot be applied to additional dates or locations. One study in China relied on a timeseries of NDVI because the land use change data were not detailed enough to represent the variations in different agricultural management practices or fine-scale plant productivity [33]. Our work builds upon and unifies these approaches by using all available soil observations in the US and incorporating satellite imagery from the Landsat archive for more complete spatial coverage. Our approach improves upon previous work by incorporating more soil measurements but fewer other predictor variables, predicting SOC at a higher resolution, including changes over time, rigorously comparing machine learning algorithms rather than selecting a single method from a prior study, and putting our work into context with past literature.

6.2 Methods and Data

We used all available SOC measurements in the US from the International Soil Carbon Network version 3 database (ISCN) (L. Nave et al., 2016), the World Soil Information Service (WOSIS) (Niels H. Batjes et al., 2017), and the RACA program. We also included observations from the Soils Data Harmonization Database (SoDaH) (Wieder et al., 2021), and Sanderman et al.'s work on soil carbon related to land use change (Sanderman et al., 2017). We ensured that all measurements were within the CONUS and taken after 1984 when Landsat 5 was launched. Landsat was chosen because of the combination of relatively fine resolution (30 m) and extremely long record (1984 – present). While NDVI products from finer spectral and spatial resolution satellites do now exist for the most recent years of the observational record, using multiple satellite products or switching between satellite products would increase the observational error already inherent in the atmospheric correction and scaling process.

We then harmonized the datasets, ensuring that all of the observations had coordinates in the same projection, at least a 30 cm deep profile, a year associated with the measurement, and no error flags. In many cases, we had to find the original study in order to locate the exact coordinates and date of the soil sample. When samples had a place or town rather than coordinates listed, we looked up the latitude and longitude. For observations reported in concentrations rather than mass per unit area, we converted the measurement for a given layer using bulk density, when available (Fowler et al., 2023; Tadiello et al., 2022). We then aggregated each profile to be a single value representing the total SOC for 0 – 30 cm, removing deeper or incomplete layers. The Intergovernmental Panel on Climate Change (IPCC) recommends 30 cm as a standard for measurements and comparisons, as most accumulations and losses occur in the upper soil layers (IPCC, 2019). The SOC values were highly positively skewed and so were transformed with a logarithmic function before modeling and then back-transformed for meaningful mapping when applying the machine learning algorithm.

Elevation was extracted for each soil sample location from a 10 m digital elevation model (DEM) of the CONUS, publicly available from the USGS. Slope and aspect were calculated from the DEM in ArcGIS Pro. A raster of bedrock geology was downloaded from the USGS. Clay content was extracted from the Unified North American Soil Map (S. Liu et al., 2014). Annual maximum and minimum temperature and annual precipitation were extracted from Daymet version 4, a 1 km gridded weather and climate product based on long-term observations (P. E. Thornton et al., 2021), for each observation location. Soil moisture was extracted from the European Space Agency (ESA) Climate Change Initiative (CCI) soil moisture maps, publicly available on the ESA's website (European Space Agency, 2022). Historical and modeled land use raster were available from the US and the land use category was extracted for each soil sample location and date (T. Sohl et al., 2016; T. L. Sohl et al., 2014).

Annual NDVI maps of the CONUS were created in Google Earth Engine for 1985-2022 using Landsat 5, 7, and 8 pixels. Clouds and haze were removed to improve landscape change detection and NDVI was calculated per pixel as

$$\frac{NIR - R}{NIR + R}$$

where NIR is near-infrared, and R is red. We found the median, 5th percentile, and 95th percentile for each year.

All further analysis was done in R (R Core Team, 2022). We stratified our dataset into validation and training such that 80% of the locations were training and 20% were designated as validation (**Figure S6.1**). Because some locations had multiple samples, this means that all locations with multiple samples were either separated into validation or training and were not split between the two. We constructed a linear regression model to predict SOC from average annual maximum and minimum temperature, average annual precipitation, bedrock geology, elevation, slope, aspect, clay content, latitude, longitude, soil moisture, and NDVI for the current year and previous 5 years, and land use for the current year and previous 5 years. We created a linear regression model to understand how much of the variation in SOC can be explained by a simple linear relationship without machine learning. As expected, there is not a strong linear relationship between the predictor variables and SOC; for example, a one cm/year increase in precipitation across a region does not translate directly to a 1 mg/ha increase or decrease in SOC stocks across the region. Then multiple machine-learning models were constructed using the same variables:

1. Random Forest (RF), R Package: randomForest
2. Regression Kriging, R Package: gstat
3. Extreme Gradient Boosting (XGB), R Package: xgboost
4. Generalized Boosted Regression (GB), R Package: gbm
5. Support Vector Machine (SVM), R Package: e1071
6. Artificial Neural Network (ANN), R Package: neuralnet
7. K-Nearest Neighbors (KNN), R Package: caret

Error and accuracy were assessed with root mean squared error (RMSE), mean absolute error (MAE), R^2 values, and the slope of the predicted vs. observed line. The model with the lowest RMSE and MAE and highest R^2 – the random forest (**Table 6.1**) – was selected to apply to the

CONUS for all years with available input data. Because we needed the previous 5 years of NDVI values for creating SOC maps by interpolation with the Random Forest, this limited our analysis to 1990 (1985, when Landsat 5 was launched + 5 years) to 2022.

Further data analysis was done using the US Department of Agriculture (USDA) farm resource regions (**Figure 6.1**), which are a set of regions in the CONUS where counties are grouped together based on farm attributes and commodities produced to better delineate geographic specialization.

6.3 Results

The Random Forest model was the algorithm with a combination of the highest R^2 value and the lowest RMSE and MAE values for the validation dataset (**Table 6.1**). MAE and RMSE are measured in mg/m^2. While the ANN and the KNN had the lowest overall MAE and RMSE values, the slope of the line between the predicted and observed was only 0.28 (for the ANN) and 0.32 (for the KNN) with similar R^2 values. Other algorithms had slopes closer to 1 with higher R^2 values. This means that the KNN and ANN models may be the most accurate – predicting values at the same scale or order of magnitude – but they are not effectively explaining the variation in SOC based on the predictor variables.

Applying the Random Forest algorithm to the CONUS to interpolate between soil observations results in spatially and temporally consistent 30 m resolution maps. Variable importance is shown in **Figure S6.2** and the fit of the model is shown in **Figure S6.3**. We produced a map for each year from 1990-2022 (available in the GitHub code repository) and calculated the mean (**Figure 6.2A**).

Mean soil carbon values are not consistent between USDA farm resource regions in the US (**Figure 6.3**) and one would not expect them to be given the different sizes of the regions (**Figure S6.4**), different land use types, soil types, and climates, but the mean shows this discrepancy particularly well. There is little interannual variation but there are large regional differences. The regions with the lowest total SOC estimates were the Mississippi Portal (1.94 ± 0.03 Pg), the Eastern Uplands (4.35 ± 0.07 Pg), and the Southern Seaboard (5.00 ± 0.15 Pg). The total SOC estimate for the Northern Great Plains is 6.63 ± 0.21 Pg. For the Prairie Gateway, it is 7.81 ± 0.37 Pg and for the Heartland, it is 6.73 ± 0.07 Pg. The highest SOC estimates were found in the Basin and Range (11.24 ± 0.22 Pg), Fruitful Rim (8.60 ± 0.28 Pg), and the Northern Crescent (7.69 ± 0.09 Pg).

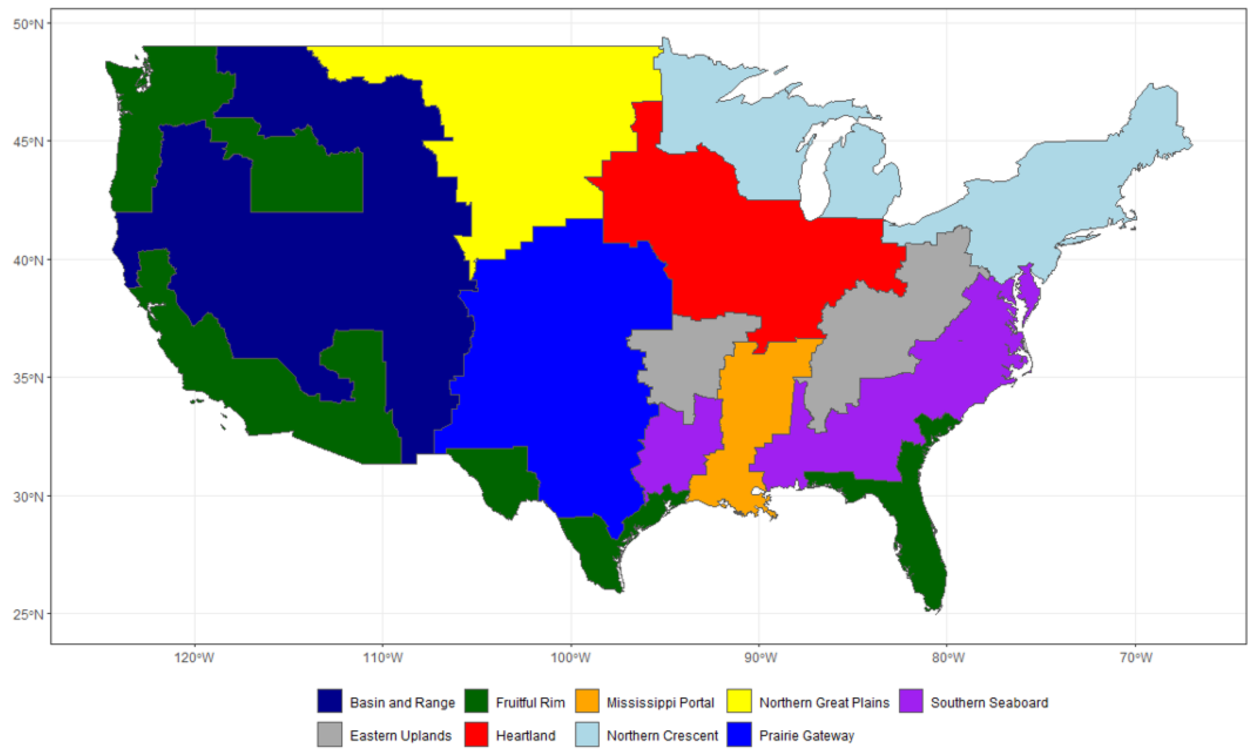

Figure 6.1 Farm Resource Regions, from the USDA.

Table 6.1 Statistical description of model fit for the machine learning algorithms and the linear regression model.

	Training				Validation			
Model	**MAE**	**RMSE**	**Slope**	**R2**	**MAE**	**RMSE**	**Slope**	**R2**
Linear Regression	0.56	0.71	0.33	0.33	0.59	0.74	0.31	0.30
Random Forest	0.30	0.40	0.79	0.84	0.42	0.57	0.54	0.59
Gradient Boosting (GBM)	0.57	0.71	0.22	0.42	0.60	0.73	0.22	0.42
Gradient Boosting (XGBoost)	0.21	0.28	0.86	0.90	0.48	0.64	0.56	0.49
SVM	0.45	0.64	0.52	0.46	0.49	0.67	0.50	0.44
Kriging	0.45	0.60	0.42	0.59	0.72	0.90	0.09	0.05
ANN	0.14	0.18	0.35	0.30	0.15	0.18	0.28	0.24
KNN	0.35	0.48	1	0.27	0.35	0.5	0.32	0.22

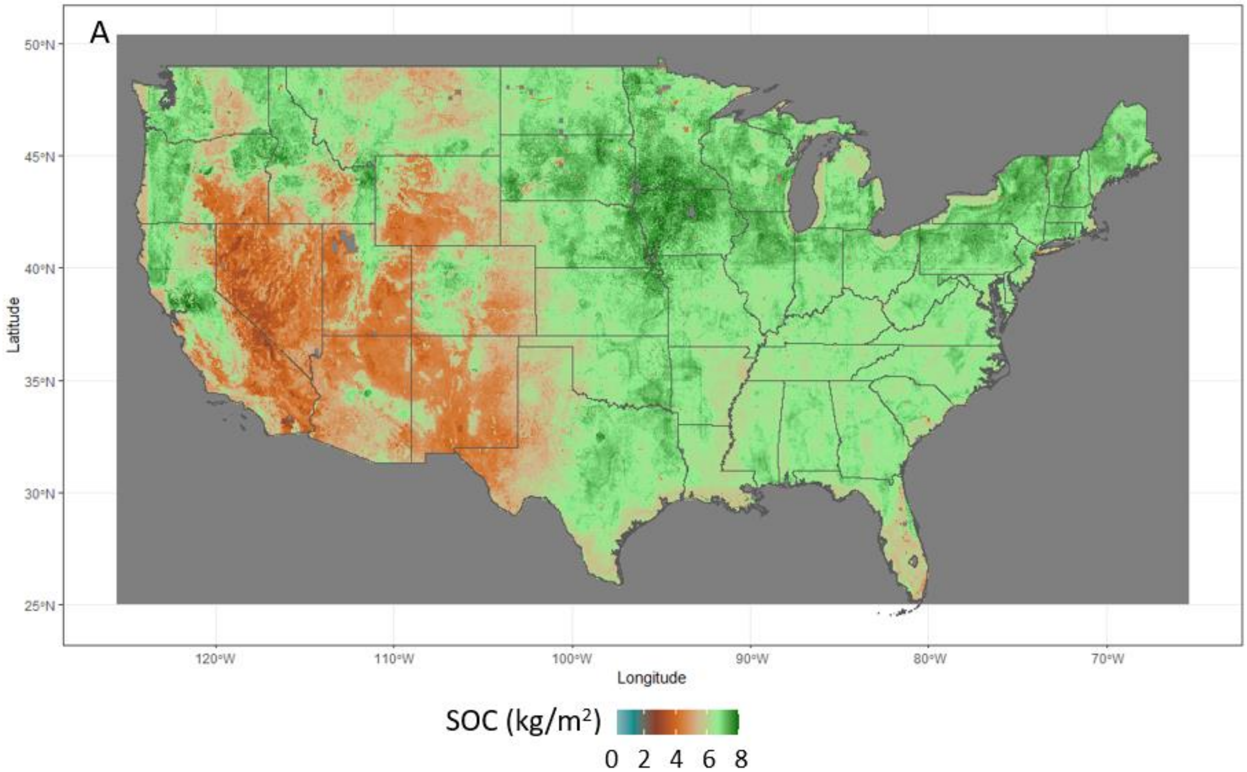

Figure 6.2 A) Mean SOC (kg/m2) from 1990-2022 in the top 30 cm of soil. B) The slope of the trendline in SOC stocks from 1990 – 2022 by pixel. Blue indicates an estimated gain in SOC and red indicates an estimated loss in SOC.

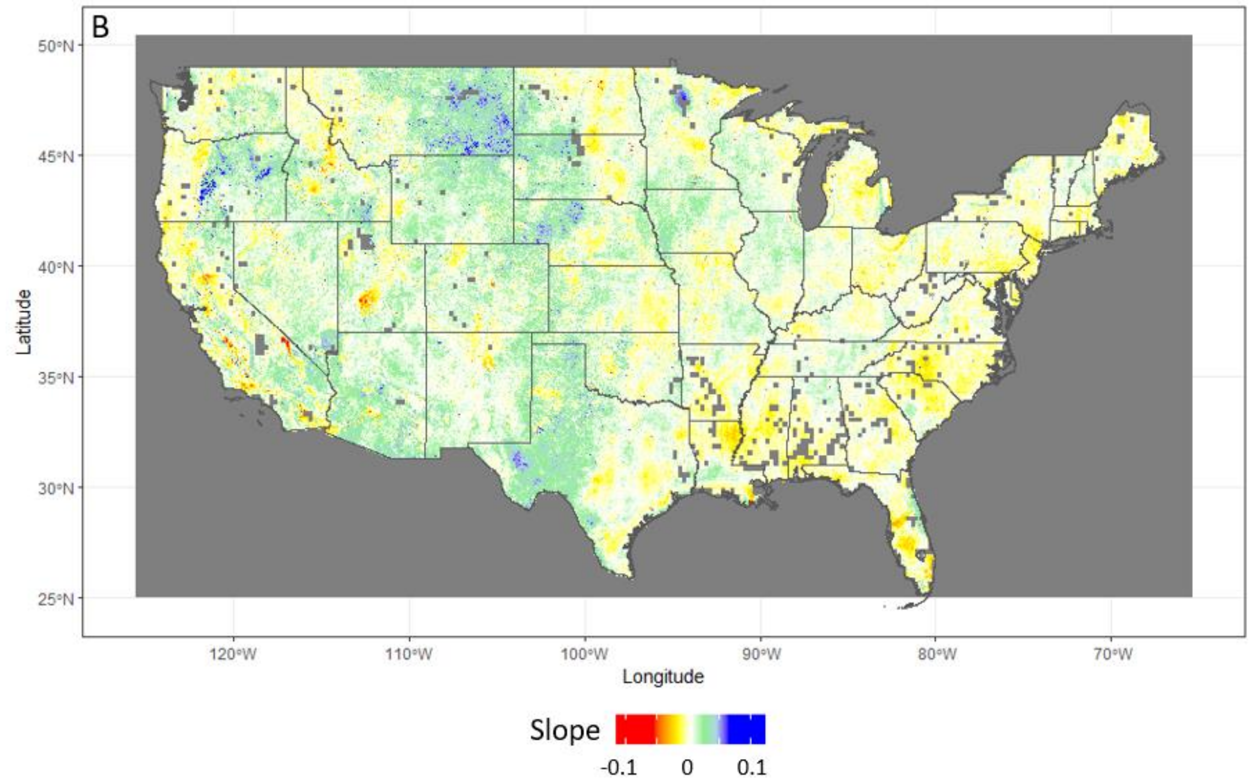

Figure 6.2 (Continued)

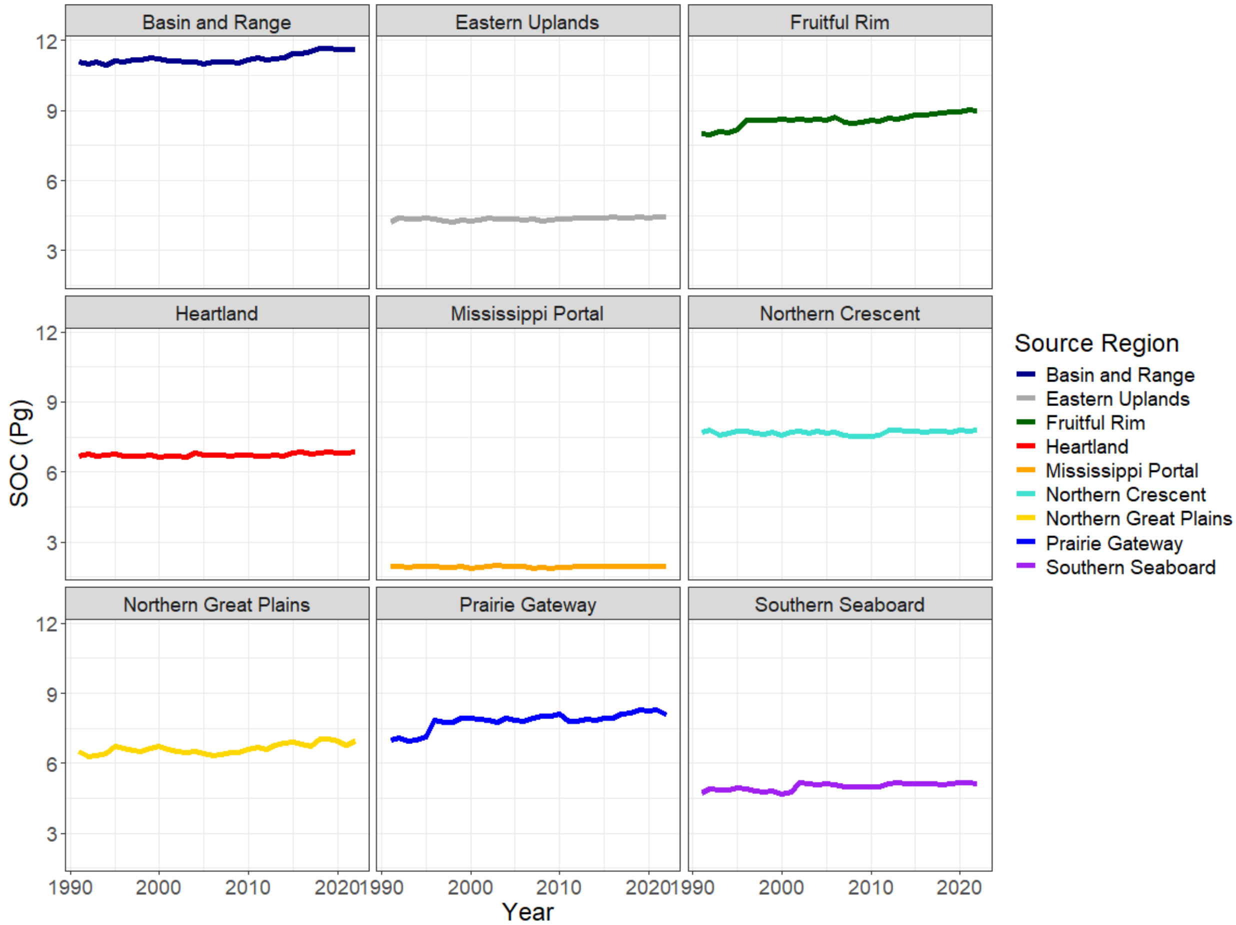

Figure 6.3 Changes in annual SOC stocks by farm resource region.

Using the land cover rasters from the USGS that were part of the input datasets for the Random Forest algorithm, we separated land use classes by year and calculated the average total SOC value for each year in each land use class. We find that of the 60.4 Pg C stored in the top 30 cm of CONUS soils, about a third of it is stored in shrubland and grassland soils and another third is stored in agricultural soils (**Figure 6.4**). Forested soils make up around a quarter of the total and the rest is split between wetlands, urban areas, barren lands and mining, and water and permanent ice or snow.

The SOC stock in land areas that experience high annual temperatures and precipitation remains consistent at close to 65% of the total (**Figure 6.5**), even as the land areas that meet this qualification may change from year to year. The annual percentage of SOC in land areas that have experienced higher than usual temperatures and precipitation rates (greater than the 95th percentile of the entire time period for each pixel) for that year are shown in **Figure 6.5**.

6.4 Discussion

Based on the difference in error metrics between the training and validation datasets, the machine learning models are overfitting the training data and therefore are not fully capturing the relationships between the input layers and the soil carbon observations. The linear regression, on the other hand, has nearly identical error metrics describing the relationship between the input layers and the SOC observations in both the training and validation datasets, meaning that around 30% of the variation in SOC (from the R^2, **Table 6.1**) value can be explained by a linear relationship between climate, topography, soil moisture, greenness (NDVI), and soil organic carbon. Soil moisture is positively correlated with SOC sequestration since water availability is crucial for plant growth, however, soil moisture also directly impacts the decomposition rate (Védère et al., 2022). Similarly, increased temperatures promote litter decomposition (Gregorich et al., 2017) but this is offset by the CO_2 fertilization effect expected with climate change (Davidson & Janssens, 2006). Topography has a similar impact where SOC increases with elevation due to cooler temperatures and more water storage capacity, but biomass inputs and soil thickness decrease at higher elevations, leading to lower SOC sequestration (Patton et al., 2019). The machine learning algorithms, particularly the Random Forest, improve upon this understanding by quantifying these non-linear relationships. One way of doing this is, for example in the case of the KNN, to memorize the training data; the end result of applying this function is a very low R^2 value for the validation dataset and an output map of soil carbon that is

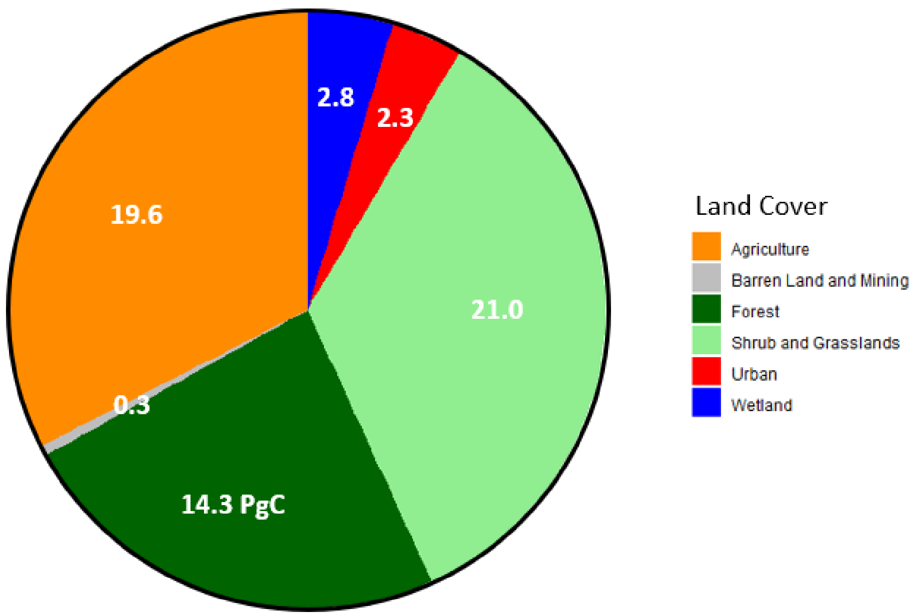

Figure 6.4 SOC stocks by land cover category in the CONUS, averaged from 1990-2022.

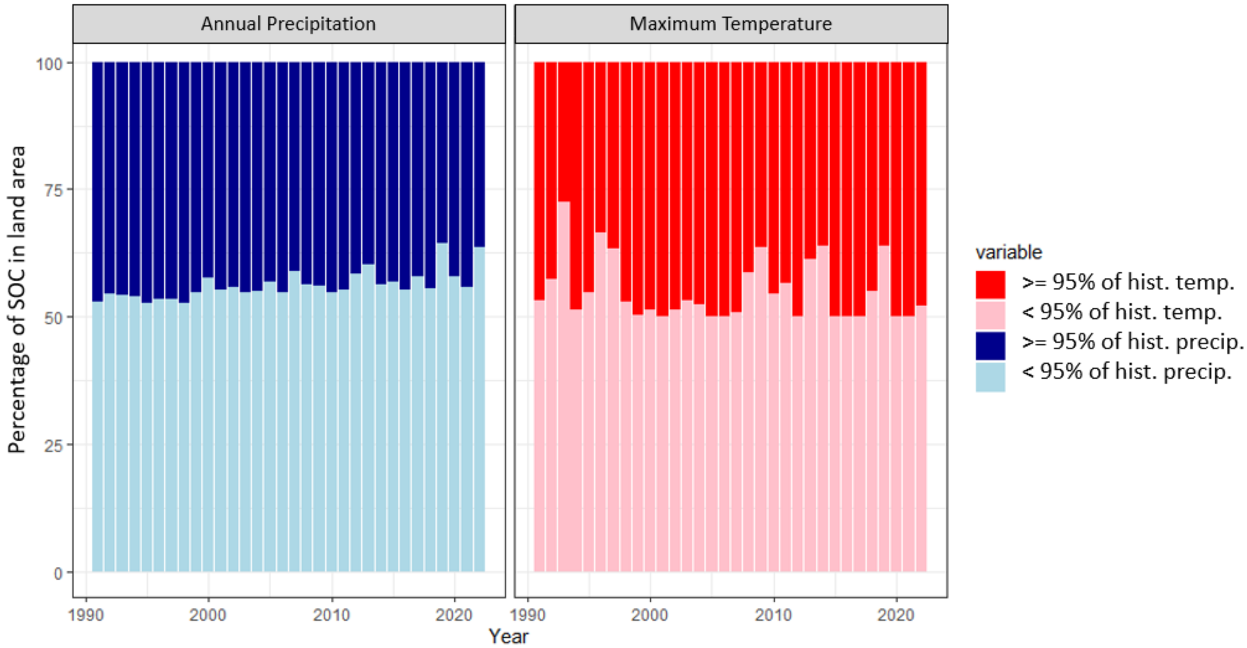

Figure 6.5 Annual percentage of SOC stocks contained in land areas with maximum temperatures greater than the 95th percentile of the maximum temperature from 1990-2022 (red), with maximum temperatures less than the 95th percentile of the maximum temperature from 1990-2022 (pink), with annual precipitation greater than the 95th percentile of the annual precipitation from 1990-2022 (dark blue), and with annual precipitation less than the 95th percentile of the annual precipitation from 1990-2022 (light blue). SOC stocks are calculated on a per pixel basis, with each pixel either exceeding or being less than the 95th percentile of the entire time period for that pixel.

Table 6.2 Modeled SOC values for the CONUS from recent literature. My study is highlighted in green. Acronyms are included below the table for improved reading comprehension.

Study	SOC (Pg C)	Resolution	Method	SOC Datasets (CONUS only)	Time Period
Bliss et al., 2014 (using SSURGO)	29.3	30 m	percentage of SOM from soil surveys	SSURGO, STATSGO2	Not stated
Wang et al., 2024	35.4	1 km	multivariate geographic clustering, RF	ISCN, NEON	Soil samples from 1920s to 2010s, bioclimatic variables from 1970-2000, MODIS from 2000-2015
HWSD-NCSCD	33.4	1 km	Taxotransfer procedure	ISRIC-WISE	Not stated
Poggio et al., 2021 (SoilGrids 2.0)	33.9	250 m	recursive feature elimination	WoSIS	Climatic variables and vegetation from 2001-2015, soil samples from 1960-2020
Guevara et al., 2020	39	250 m	RF, recursive feature elimination, simulated annealing	ISCN, RaCA,	1991-2010
Chaney et al., 2019	59.2	30 m	ANN, RF	POLARIS soil series, NASIS, SSURGO, STATSGO2, NCSS SCD	Not stated
Rubin et al.	60.4	30 m	RF, GB, XGB, ANN, SVM, KNN, kriging, linear reg.	ISCN, RaCA, WOSIS, SoDaH, Sanderman et al., 2017	1990-2022
Gautam et al., 2022	64.2	100 m	RF, GB, XGB	RaCA	2014-2100
Batjes, 2016	97.7	1 km	Taxotransfer procedure	ISRIC-WISE, ISCN	Not stated

Table 6.2 (Continued)

Tao et al., 2020	*77.4 - 101.2*	*0.5°*	*Bayesian Markov Chain Monte Carlo*	*WoSIS*	*MODIS from 2000-2015*
Hengl et al., 2017 (SoilGrids250m)	102.4	250 m	RF, GB, ANN	WoSIS	Not stated
Ramcharan et al., 2018	106.2	100 m	RF, GB	NCSS, NASIS, RaCA	Not stated

Name	Acronym
National Cooperative Soil Survey Characterization	NCSS
National Soil Information System	NASIS
International Soil Reference and Information Centre World Inventory of Soil Emission Potentials	ISRIC-WISE
National Ecological Observatory Network	NEON
Instituto Nacional de Estadística y Geografía	INEGI
Institute of Soil Science	ISS
European Soil Data Centre	ESDAC
Harmonized World Soil Database	HWSD

not meaningful and does not accurately reflect reality. However, the Random Forest is doing a reasonable job at predicting SOC in new locations and does improve upon the linear regression; while the output maps are not perfect, they do reflect the actual spatial patterns of SOC in the CONUS in a meaningful enough way to derive useful climate and land use relationships from them.

There are large differences in estimates of soil carbon stocks from different global and regional databases (**Table 6.2**) but predictions for the US do tend to be underestimated when compared to field data (Tifafi et al., 2018). One study used SSURGO filled from STATSGO2 to estimate SOC in the CONUS from 0 – 30 cm and found 29.3 Pg C. The Harmonized World Soil Database (HWSD) in combination with the Northern Circumpolar Soil Carbon Database (NCSCD) produced an estimate of 33.4 Pg C (Z. Wang et al., 2024). SoilGrids 2.0 maps estimated at 33.9 Pg C (Poggio et al., 2021). A recent study using multivariate geographic clustering and a random Forest model found that total soil carbon stocks in the CONUS total 35.4 ± 1.8 Pg at a depth of 0 – 30 cm (Z. Wang et al., 2024). A modeling effort across Mexico and the CONUS using a Random Forest model estimates at 0-30cm depth from 1991–2010 of 39 Pg across the CONUS (Mario Guevara et al., 2020). The Probabilistic Remapping of SSURGO (POLARIS) database of soil property maps predicts 59.2 Pg across the CONUS (Chaney et al., 2019). One study of SOC in the US using observations and earth system model (ESM) projections with machine learning estimated present-day stocks at 64.2 Pg C for up to 1 m depth. The ESM-only estimate was 69.4 Pg C (Gautam et al., 2022). RACA estimates total carbon storage in the CONUS is 73 Pg but they do not explicitly state the depth of the measurements (Sundquist et al., 2009). Different methods to improve the representation of SOC distribution in a land biogeochemical model (CLM5) produced estimates ranging from 77.4 to 101.2 Pg C (Tao et al., 2020). The World Inventory of Soil Property Estimates (WISE30) estimated that the total SOC stocks in the CONUS were 97.7 Pg C for 0 – 30 cm (N. H. Batjes, 2016). One commonly used dataset, SoilGrid250m, estimated 102.4 Pg C across the CONUS at 0 – 30 cm (Hengl et al., 2017). Calculation from soil property and class maps of CONUS at 100 m spatial resolution indicated 106.2 Pg at 0 – 30 cm (Ramcharan et al., 2018). These are wide-ranging values, from a low of 29.3 to a high of 106.2 Pg C for the same area for generally the same time period, although soil carbon changes slowly so any differences in timeframe are unlikely to account for such drastically different estimates. It has been demonstrated that predictors of SOC vary by spatial scale (Adhikari et al., 2020) and so some of this large variation could be explained by the different resolutions of these studies which vary from 250 m (Hengl et al., 2017) to 1 km (Z. Wang et al., 2024). This issue of aggregation producing different results depending on the scale is known as the Modifiable Area Unit Problem (MAUP) in geographic research (Gehlke & Biehl, 1934). However, in this case, it is additionally complicated because the underlying datasets are not identical. Our approach seeks to harmonize a wide variety of datasets and create an informative and useful accounting of regional variations and total SOC in the US, including a comprehensive comparison of different machine learning methods that are commonly employed.

6.5 Regional Differences

The recent paper by Wang et al. (Z. Wang et al., 2024) on upscaling soil organic carbon measurements in the US to create a unified map relies on a representativeness analysis and a separate Random Forest model for each of the 20 regions they identify. This approach with multivariate geographic clustering demonstrates that different predictor variables have different importances in the location-specific Random Forest models, but it also means that the framework lacks some applicability outside of these regions. Where this analysis is particularly valuable, however, is in locating regions that have high uncertainty and therefore should be targeted in future SOC monitoring and field sampling efforts. Our results agree with theirs on the spatial pattern of SOC stocks: SOC generally decreases with latitude and the West and Rocky Mountains have particularly low values but also encompass a very large region (**Figure 6.3**). In these regions, many of the soils are aridisols, which are extremely soil moisture-limited and contain very little organic content. The Fruitful Rim and Prairie Gateway have been gaining SOC consistently since 1990 while every other region has remained closer to constant, potentially due to a combination of increased precipitation, reforestation, and relatively stable temperatures (Barnes et al., 2024; L. E. Nave et al., 2022).

Additionally, Wang et al. make the argument that because the SOC observations within each region were not taken with the region already defined, this implies that the distribution is random in terms of environmental conditions. They also reason that some regions have particularly low representativeness as well as high uncertainty due to lack of sampling density. We do not disagree with the fundamental conclusion that more sampling in these areas would decrease uncertainty, but we do make the point that regions that are historically important in terms of SOC such as agricultural areas are likely to be more similar in terms of environmental characteristics (higher representativeness) than the whole region and therefore oversampled in relation to the entire region. Our approach, rather, randomly separates the observations into training and validation datasets by location before creating a single Random Forest model for the whole CONUS. Our model instead relies on the interaction between variables across the entire landscape to interpolate SOC. This is consistent with other approaches that have shown that geochemical and climate predictors are relatively constant in importance across landscapes and depths (Yu et al., 2021). In fact, annual temperatures and precipitation do not greatly influence the interannual variation in SOC stocks across the CONUS (**Figure 6.5**). This means that some extreme events such as drought do not have as great an impact on SOC as feared, because of the short timescales involved. Drought reduces soil carbon content because of decreased plant litter input, but it also decreases CO_2 flux because of the slowing rate of decomposition (Deng et al., 2021). However, these effects are regulated by land cover type, meaning that the impact of a single drought is hard to see in the long-term SOC stocks averaged over the entire CONUS. This is a positive characteristic of the soil for long-term carbon storage since ideally carbon stored in the soil will not be quickly lost to the atmosphere every time the soil dries out. Other research has shown that drought and irrigation both produce slight increases in the soil C pool due to decreases in heterotrophic respiration and increases in new input material, respectively (X. Zhou et al., 2016).

There is little year-to-year change in SOC stocks among regions with similar temperature and precipitation regimes, demonstrating that while climate does impact regional SOC totals, it is on much longer timescales than annual or even decadal.

6.6 Land Use

1. Forested Lands

Our estimate of SOC in forested lands is 14.3 Pg C (**Figure 6.4**). A recent study of carbon stock averaged from 2001 to 2005 in the upper 20 cm of federal lands estimated that 8.7 Pg is stored in forested soils (Z. Tan et al., 2015). Forested federal lands are a significant portion of the US forested lands but are not representative of the total. One study used SSURGO with gaps filled from STATSGO2 and found that forested lands contain 7.4 Pg C (Bliss et al., 2014). Another study estimated that 31% of the total SOC in the CONUS is stored in forested soils, which according to our estimate would be 18.7 Pg C (Mario Guevara et al., 2020). Our estimate is in the middle of this range, potentially because we do not differentiate between forested lands that have been disturbed through anthropogenic modification or management, fires, or other natural causes and undisturbed forested lands, given that the NDVI values for disturbed versus undisturbed forest would not significantly differ. SOC in forested soils is particularly susceptible to decline under these conditions (An et al., 2021) which would not be captured simply by NDVI, soil moisture, and broad land use categories. Our estimate could be high, however, because of the tendency of wetlands to be obscured by or misclassified as forested lands in land use classifications (Stewart et al., 2024).

2. Shrublands and Grasslands

Our estimate of SOC in shrubs and grasslands is 21.0 Pg C (**Figure 6.4**), with shrublands accounting for 9.9 Pg C and grasslands accounting for 11.6 Pg C. A recent study of carbon stock averaged from 2001 to 2005 in the upper 20 cm of federal lands estimated that merely 2 Pg C is stored in shrublands and grasslands on federal lands (Z. Tan et al., 2015); however, the percentage of federal lands that are shrublands or grasslands is low, given that 85% of grasslands are privately owned (Wyden, 2022). Another study estimated that 34.9% of the total SOC in the CONUS is stored in shrubland and grassland soils, which given our values would be 21.1 Pg C (Mario Guevara et al., 2020). Generally, researchers estimate that about a third of global soil carbon is stored in grasslands (Bai & Cotrufo, 2022); our estimate (at 34.5 %) agrees with that of the CONUS. However, shrublands and grasslands, while considered together here are not actually the same land use type, and many studies separate them. There is some disagreement about the role of shrublands in sequestering carbon; shrubland encroachment into grasslands, for example, has been shown to increase SOC content in topsoils (H. Li et al., 2016) but shrublands in China have been shown to store less SOC than grasslands (J. Ge et al., 2020). Research focusing exclusively on the difference between carbon storage in grasslands and shrublands in the US is limited because these regions are dried and so tend to uptake less carbon than forests and are further complicated by the dynamics of prevalent wildfire and regrowth cycles (Provencher et al., 2023).

3. Wetlands

Our estimate of SOC in wetlands is 2.8 Pg C (**Figure 6.4**). One recent study specifically focusing on carbon storage in US wetlands estimated that 11.52 Pg C is stored in wetland soils, mostly deeper than 30 cm. Their estimate for both the sampled (2.63±0.12 Pg C) and unsampled but interpolated (4.02 Pg C) population of wetlands for 0 – 30 cm is 6.65 ±0.12 Pg C. However, this includes tidal saline wetlands and other inland wetlands that are not in our study area (Nahlik & Fennessy, 2016). A separate study of wetland soil carbon estimated that 8.4 Pg C is stored in inland wetlands in the first meter of soil (Uhran et al., 2021). One more study used SSURGO with gaps filled from STATSGO2 and found that wetlands total only 3.7 Pg C (Bliss et al., 2014). Our estimate of SOC in wetlands is therefore likely incomplete; the lack of SOC observations from wetlands means that the Random Forest model is not trained to associate wetlands with high SOC values. Similarly, excluding both tidal and some inland wetlands means that those regions are also undervalued in terms of SOC storage.

4. Croplands

Our estimate of SOC in croplands is 19.6 Pg C (**Figure 6.4**). A recent study used SSURGO with gaps filled from STATSGO2 and found that grasslands, shrublands, and agriculture together total 16.2 Pg C (Bliss et al., 2014). Other researchers estimated that 27% of the total SOC in the CONUS is found in agricultural soils, which given our estimate would be 16.7 Pg C (Mario Guevara et al., 2020). The carbon storage potential of croplands is a heavily debated issue because management practices contribute heavily to variations in SOC values and therefore have the potential to offset the impacts on SOC storage from climate change (Ren et al., 2020). Effects of land use change and land management are estimated to be 7-10 times larger than direct effects of climate change, excluding indirect effects such as wildfires (Beillouin et al., 2023). The effects of wildfires on soil carbon pools vary widely depending on fire extent and severity, soil type, tree species, elevation, slope, and ecosystem (Y. Cheng et al., 2023). Fires lead to carbon loss as both plant and soil biomass burn; however, during the fire recovery process, soil carbon increases as fires promote soil microbial activity and pyrogenic carbon is sequestered (Y. Cheng et al., 2023). We find, similarly, that there is no clear relationship between fire activity and SOC (**Figure S6.4**).

Much of the gain in SOC in the CONUS over the last hundred years can be attributed to cropland expansion and nitrogen fertilizer use (Ren et al., 2020). Interventions like biochar and agroforestry have been shown to help rebuild SOC stocks in croplands (Chenu et al., 2019). However, there is no way to differentiate between land management practices in our maps without an additional dataset to label lands. For example, the Random Forest model may "know" that a specific field has had a cover crop over the winter because the NDVI value remains higher than if it were bare soil; but it cannot say that that field has been managed with no-till vs. the plowing before planting.

Intensive tillage has historically been highest in the Fruitful Rim, the Mississippi Portal, and the Southern Seaboard while the Prairie Gateway, Heartland, and Northern Great Plains have historically benefited from higher rates of reduced tillage and conservation tillage practices (**Figure S6.5**). These Midwestern areas are also the ones that have a more positive slope in the annual rate of SOC change while the most negative changes in SOC accumulation are all found in the Southern Seaboard, Eastern Uplands, and Northern Crescent (**Figure 6.2B**).

6.7 Climate Change

From a study on urban greenspaces, mapping SOC with a Random Forest model, we know that higher SOC levels are associated with colder, less variable climates, particularly in older undisturbed areas where vegetation can regrow (H. Guo et al., 2024). With the world warming due to the increased CO_2 in the atmosphere there will be two effects: 1) more plant growth due to higher CO_2 levels, leading to higher soil carbon, and 2) increased microbial activity due to the warmer temperature leading to more soil carbon loss (J. Liu et al., 2022). Overall, SOC will be reduced by 10.5% globally under 1.5 degrees C of warming (M. Wang et al., 2024). However, this effect will have regional variation. For example, one study showed that warming-induced vegetation growth canceled out soil carbon-climate feedback in the northern Asian permafrost region (J. Liu et al., 2022). In Florida, research showed that SOC sequestration under climate change was dependent on the land use type (Xiong et al., 2014) and in the Upper Midwest and Ohio Valley regions, research showed that SOC stocks will decline as temperatures and precipitation increase, although this will be dependent on the agricultural practices (Grace et al., 2006).

Nearly 50% of the SOC in the entire CONUS is located in regions that have experienced unusually high temperatures (**Figure 6.5**); this is not an indication of SOC or temperature changing rapidly, but rather an indication that the highest levels of soil carbon are located in places that are frequently experiencing both higher temperatures and more rainfall than the average. The precipitation patterns are more variable, with between 30% and 50% of the total SOC in regions that experience unusually high precipitation each year (**Figure 6.5**). Climate extremes can also impact the spatial distribution of carbon loss and the pattern of loss is not consistent across different ecosystems (M. Wang et al., 2024) or time periods because multiple extreme events can impact the carbon cycle both concurrently and also with a time-lagged response (Arnone III et al., 2008; Frank et al., 2015). The timing of these climate extremes is important and different ecosystems experience different impacts (Frank et al., 2015). For example, croplands are affected differently than other ecosystems because they are managed, and interventions can happen quickly (such as irrigation to offset a drought). The soil-vegetation system is also reset regularly throughout the year, and the type and duration of crop cover are variable (Reichstein et al., 2013). Additionally, there is a temporal element because crops can be vulnerable to specific stressors at different stages of the year.

6.8 Conclusions

We compile a set of comprehensive georeferenced databases of SOC measurements in the CONUS and match the soil observations with climate, topography, soil moisture, and NDVI layers based on the date and location of the measurement. We then use this database to compare 7 machine learning models and linear regression in terms of how well they can interpolate SOC stocks in the top 30 cm of soil across the region. We generate spatially and temporally continuous maps of SOC using the best performing model – the Random Forest – and evaluate land use and climate impacts on SOC. We demonstrate that the factors that influence SOC do so on long time scales and the lack of interannual variation is a desirable property for carbon capture and carbon sequestration on a landscape scale. Our maps and analysis have great potential to be a resource for further studies on soil biogeochemistry and the role of anthropogenic disturbance and land use changes. In particular, we include soil measurements from more sources than many of the previous research efforts, we compare a wide range of potential machine learning models instead of selecting a single one based on a single prior approach, and our covariate selection is relatively simple (unlike, for example, SoilGrids 2.0 which includes around 400 covariate layers). We also suggest that future soil sampling should be better distributed to more accurately represent the variation in climate, topography, and land use across the landscape.

Chapter 7 Conclusions

This research investigates several facets of global environmental change and demonstrates the effectiveness of machine learning for quantification of climate risks and uncertainties both in terms of historical data and in the near future.

First, I update the 2010 deposition budgets for reactive nitrogen and sulfur deposition using measurement-model fusion to combine the broad spatial coverage of a model with accurate in-situ measurements. This work emphasizes the necessity of combining models with observations wherever possible, to better capture regional patterns and to inform policy and decision-making. Future work to improve measurement-model fusion should investigate more advanced MMF methods to avoid the limitations associated with IDW such as surface artifacts and high error in regions with sparse measurements. It should also incorporate satellite remote sensing derived concentrations to improve model estimates where in-situ measurements are not available.

Second, I evaluate the potential ecological impacts of enacting SAI globally in the near future by focusing on an often-overlooked aspect of SAI – sulfur deposition. My work compares sulfur deposition under G6sulfur with SSP2-4.5 and SSP5-8.5 scenarios. There are large discrepancies across models and injection strategies and as such it is challenging to compare projections by creating ensembles, as is the usual method for multidimensional climate variables. Much more work is needed in this area to incorporate nitrogen-sulfur interactions and bidirectional flux into the ESMs as well as ensuring land and fire models accurately capture sulfur dynamics and stratosphere-troposphere interactions.

My fourth study investigates the trend of increasing heat wave frequency, intensity, and duration on a regional scale using new fine-resolution climate data ensembles and compares two downscaling approaches to other commonly used meteorology products. I systematically compare the model estimates from two separate ensembles of dynamically and statistically downscaled models with meteorological observations and assess the sensitivity of a heat wave index to four percentile thresholds and three reference timeframes. My work shows that the downscaling method, heat wave index, and temporal and spatial scale directly influence model estimates, although heat waves are projected to increase in magnitude and duration regardless of the index used for analysis. This demonstrates the importance of dynamical downscaling a fine spatial scale for regional insights into processes occurring on an intra-annual basis and emphasizes the need for urgent preparations for a hotter future climate.

And the fifth study is fundamentally about mitigating climate change through industrial decarbonization. Many efforts in the direction have begun, but without baseline maps of SOC, it is hard to accurately assess whether targets have been met. I compiled a georeferenced database of SOC measurements in the CONUS and matched the soil observations with climate, topography, soil moisture, and NDVI based on the date and location of the measurement. I then used this database to compare 7 machine learning models and a linear regression in terms of how well they can interpolate SOC stocks in the top 30 cm of soil across the region. I generated spatially and temporally continuous maps of SOC using the best performing model – the Random Forest – and evaluated land use and climate impacts on SOC. My work demonstrates that the factors that influence SOC do so on long time scales and the lack of interannual variation is in fact a desirable property for carbon capture and carbon sequestration on a landscape scale. These maps and analysis have great potential to be a resource for further studies on soil biogeochemistry and the role of anthropogenic disturbance and land use changes.

References

Aas, W., Mortier, A., Bowersox, V., Cherian, R., Faluvegi, G., Fagerli, H., et al. (2019). Global and regional trends of atmospheric sulfur. *Scientific Reports*, *9*(1), 953. https://doi.org/10.1038/s41598-018-37304-0

Abram, N. J., McGregor, H. V., Tierney, J. E., Evans, M. N., McKay, N. P., & Kaufman, D. S. (2016). Early onset of industrial-era warming across the oceans and continents. *Nature*, *536*(7617), 411–418. https://doi.org/10.1038/nature19082

Adhikari, K., Mishra, U., Owens, P. R., Libohova, Z., Wills, S. A., Riley, W. J., et al. (2020). Importance and strength of environmental controllers of soil organic carbon changes with scale. *Geoderma*, *375*, 114472. https://doi.org/10.1016/j.geoderma.2020.114472

Adon, M., Galy-Lacaux, C., Yoboué, V., Delon, C., Lacaux, J. P., Castera, P., et al. (2010). Long term measurements of sulfur dioxide, nitrogen dioxide, ammonia, nitric acid and ozone in Africa using passive samplers. *Atmospheric Chemistry and Physics*, *10*(15), 7467–7487. https://doi.org/10.5194/acp-10-7467-2010

An, Z., Bernard, G. M., Ma, Z., Plante, A. F., Michaelis, V. K., Bork, E. W., et al. (2021). Forest land-use increases soil organic carbon quality but not its structural or thermal stability in a hedgerow system. *Agriculture, Ecosystems & Environment*, *321*, 107617. https://doi.org/10.1016/j.agee.2021.107617

Anderson, D. M., Burkholder, J. M., Cochlan, W. P., Glibert, P. M., Gobler, C. J., Heil, C. A., et al. (2008). Harmful algal blooms and eutrophication: Examining linkages from selected coastal regions of the United States. *Harmful Algae*, *8*(1), 39–53. https://doi.org/10.1016/j.hal.2008.08.017

Angelopoulou, T., Tziolas, N., Balafoutis, A., Zalidis, G., & Bochtis, D. (2019). Remote Sensing Techniques for Soil Organic Carbon Estimation: A Review. *Remote Sensing*, *11*(6), 676. https://doi.org/10.3390/rs11060676

Arbuthnott, K. G., & Hajat, S. (2017). The health effects of hotter summers and heat waves in the population of the United Kingdom: a review of the evidence. *Environmental Health*, *16*(1), 119. https://doi.org/10.1186/s12940-017-0322-5

d’Arge, R. C., Schulze, W. D., & Brookshire, D. S. (1982). Carbon Dioxide and Intergenerational Choice. *The American Economic Review*, *72*(2), 251–256.

Argüeso, D., Di Luca, A., Perkins-Kirkpatrick, S. E., & Evans, J. P. (2016). Seasonal mean temperature changes control future heat waves. *Geophysical Research Letters*, *43*, 7653–7660.

Arnone III, J. A., Verburg, P. S. J., Johnson, D. W., Larsen, J. D., Jasoni, R. L., Lucchesi, A. J., et al. (2008). Prolonged suppression of ecosystem carbon dioxide uptake after an anomalously warm year. *Nature*, *455*(7211), 383–386. https://doi.org/10.1038/nature07296

Ashfaq, M., Rastogi, D., Mei, R., Kao, S.-C., Gangrade, S., Naz, B. S., & Touma, D. (2016). High-resolution ensemble projections of near-term regional climate over the continental United States. *Journal of Geophysical Research: Atmospheres*, *121*(17), 9943–9963. https://doi.org/10.1002/2016JD025285

Ashfaq, M., Rastogi, D., Kitson, J., Abid, M. A., & Kao, S.-C. (2022). Evaluation of CMIP6 GCMs Over the CONUS for Downscaling Studies. *Journal of Geophysical Research: Atmospheres*, *127*(21), e2022JD036659. https://doi.org/10.1029/2022JD036659

Asia Center for Air Pollution Research. (2021). Acid Deposition Monitoring Network in East Asia (EANET). Retrieved November 18, 2021, from https://www.eanet.asia/

Bai, Y., & Cotrufo, M. F. (2022). Grassland soil carbon sequestration: Current understanding, challenges, and solutions. *Science*, *377*(6606), 603–608. https://doi.org/10.1126/science.abo2380

Bailey, V. L., Pries, C. H., & Lajtha, K. (2019). What do we know about soil carbon destabilization? *Environmental Research Letters*, *14*(8), 083004. https://doi.org/10.1088/1748-9326/ab2c11

Balbus, J., Crimmins, A., Gamble, J. L., Easterling, D. R., Kunkel, K. E., Saha, S., & Sarofim, M. C. (2016). *Ch. 1: Introduction: Climate Change and Human Health. The Impacts of Climate Change on Human Health in the United States: A Scientific Assessment*. U.S. Global Change Research Program. https://doi.org/10.7930/J0VX0DFW

Barnes, M. L., Zhang, Q., Robeson, S. M., Young, L., Burakowski, E. A., Oishi, A. Christopher., et al. (2024). A Century of Reforestation Reduced Anthropogenic Warming in the Eastern United States. *Earth's Future*, *12*(2), e2023EF003663. https://doi.org/10.1029/2023EF003663

Batibeniz, F., Ashfaq, M., Diffenbaugh, N. S., Key, K., Evans, K. J., Turuncoglu, U. U., & Önol, B. (2020). Doubling of U.S. Population Exposure to Climate Extremes by 2050. *Earth's Future*, *8*(4), e2019EF001421. https://doi.org/10.1029/2019EF001421

Batjes, N. H. (2016). Harmonized soil property values for broad-scale modelling (WISE30sec) with estimates of global soil carbon stocks. *Geoderma*, *269*, 61–68. https://doi.org/10.1016/j.geoderma.2016.01.034

Batjes, Niels H., Ribeiro, E., van Oostrum, A., Leenaars, J., Hengl, T., & Mendes de Jesus, J. (2017). WoSIS: providing standardised soil profile data for the world. *Earth System Science Data*, *9*(1), 1–14. https://doi.org/10.5194/essd-9-1-2017

Behnke, R., Vavrus, S., Allstadt, A., Albright, T., Thogmartin, W. E., & Radeloff, V. C. (2016). Evaluation of downscaled, gridded climate data for the conterminous United States. *Ecological Applications*, *26*(5), 1338–1351. https://doi.org/10.1002/15-1061

Beillouin, D., Corbeels, M., Demenois, J., Berre, D., Boyer, A., Fallot, A., et al. (2023). A global meta-analysis of soil organic carbon in the Anthropocene. *Nature Communications*, *14*(1), 3700. https://doi.org/10.1038/s41467-023-39338-z

Belgiu, M., & Drăguţ, L. (2016). Random forest in remote sensing: A review of applications and future directions. *ISPRS Journal of Photogrammetry and Remote Sensing*, *114*, 24–31. https://doi.org/10.1016/j.isprsjprs.2016.01.011

Benish, S. E., Bash, J. O., Foley, K. M., Appel, K. W., Hogrefe, C., Gilliam, R., & Pouliot, G. (2022). Long-term regional trends of nitrogen and sulfur deposition in the United States from 2002 to 2017. *Atmospheric Chemistry and Physics*, *22*(19), 12749–12767. https://doi.org/10.5194/acp-22-12749-2022

Bliss, N. B., Waltman, S. W., West, L. T., Neale, A., & Mehaffey, M. (2014). Distribution of Soil Organic Carbon in the Conterminous United States. In A. E. Hartemink & K. McSweeney (Eds.), *Soil Carbon* (pp. 85–93). Cham: Springer International Publishing. https://doi.org/10.1007/978-3-319-04084-4_9

Bobbink, R., Hicks, K., Galloway, J., Spranger, T., Alkemade, R., Ashmore, M., et al. (2010). Global assessment of nitrogen deposition effects on terrestrial plant diversity: a synthesis. *Ecological Applications*, *20*(1), 30–59. https://doi.org/10.1890/08-1140.1

Bowman, W. D., Cleveland, C. C., Halada, Ĺ., Hreško, J., & Baron, J. S. (2008). Negative impact of nitrogen deposition on soil buffering capacity. *Nature Geoscience*, *1*(11), 767–770. https://doi.org/10.1038/ngeo339

Braganza, K., Karoly, D. J., & Arblaster, J. M. (2004). Diurnal temperature range as an index of global climate change during the twentieth century. *Geophysical Research Letters*, *31*(13). https://doi.org/10.1029/2004GL019998

Brás, T. A., Seixas, J., Carvalhais, N., & Jägermeyr, J. (2021). Severity of drought and heatwave crop losses tripled over the last five decades in Europe. *Environmental Research Letters*, *16*(6), 065012. https://doi.org/10.1088/1748-9326/abf004

Breiman, L. (2001). Random forests. *Machine Learning*, *45*(1), 5–32. https://doi.org/10.1023/A:1010933404324

Breshears, D. D., Fontaine, J. B., Ruthrof, K. X., Field, J. P., Feng, X., Burger, J. R., et al. (2021). Underappreciated plant vulnerabilities to heat waves. *New Phytologist*, *231*(1), 32–39. https://doi.org/10.1111/nph.17348

Budikova, D., Ford, T. W., & Ballinger, T. J. (2019). United States Heat Wave Frequency and Arctic Ocean Marginal Sea Ice Variability. *Journal of Geophysical Research: Atmospheres*, *124*(12), 6247–6264. https://doi.org/10.1029/2018JD029365

Chaney, N. W., Minasny, B., Herman, J. D., Nauman, T. W., Brungard, C. W., Morgan, C. L. S., et al. (2019). POLARIS Soil Properties: 30-m Probabilistic Maps of Soil Properties Over the Contiguous United States. *Water Resources Research*, *55*, 2916–2938. https://doi.org/doi.org/10.1029/2018WR022797

Chen, G., Li, S., Knibbs, L. D., Hamm, N. A. S., Cao, W., Li, T., et al. (2018). A machine learning method to estimate PM2.5 concentrations across China with remote sensing, meteorological and land use information. *Science of The Total Environment*, *636*, 52–60. https://doi.org/10.1016/j.scitotenv.2018.04.251

Cheng, I., Zhang, L., He, Z., Cathcart, H., Houle, D., Cole, A., et al. (2022). Long-term declines in atmospheric nitrogen and sulfur deposition reduce critical loads exceedances at multiple Canadian rural sites, 2000–2018. *Atmospheric Chemistry and Physics*, *22*(22), 14631–14656. https://doi.org/10.5194/acp-22-14631-2022

Cheng, W., MacMartin, D. G., Dagon, K., Kravitz, B., Tilmes, S., Richter, J. H., et al. (2019). Soil Moisture and Other Hydrological Changes in a Stratospheric Aerosol

Geoengineering Large Ensemble. *Journal of Geophysical Research: Atmospheres*, *124*(23), 12773–12793. https://doi.org/10.1029/2018JD030237

Cheng, Y., Luo, P., Yang, H., Li, H., Luo, C., Jia, H., & Huang, Y. (2023). Fire effects on soil carbon cycling pools in forest ecosystems: A global meta-analysis. *Science of The Total Environment*, *895*(165001). https://doi.org/DOI:10.1016/j.scitotenv.2023.165001

Chenu, C., Angers, D. A., Barré, P., Derrien, D., Arrouays, D., & Balesdent, J. (2019). Increasing organic stocks in agricultural soils: Knowledge gaps and potential innovations. *Soil and Tillage Research*, *188*, 41–52. https://doi.org/10.1016/j.still.2018.04.011

Clarisse, L., Van Damme, M., & Coheur, P. -F. (2018). Standard daily IASI/Metop-A ULB-LATMOS ammonia (NH3)L2 product (total column). AERIS. Retrieved from https://www.aeris-data.fr/metadata/metadata/

Clark, Brendan, Xia, L., Robock, A., Tilmes, S., Richter, J. H., Visioni, D., & Rabin, S. S. (2023). Optimal climate intervention scenarios for crop production vary by nation. *Nature Food*, *4*(10), 902–911. https://doi.org/10.1038/s43016-023-00853-3

Clark, Britta. (2023). How to Argue about Solar Geoengineering. *Journal of Applied Philosophy*, *40*(3), 505–520. https://doi.org/10.1111/japp.12643

Clark, C. M., Bai, Y., Bowman, W. D., Cowles, J. M., Fenn, M. E., Gilliam, F. S., et al. (2013). Nitrogen Deposition and Terrestrial Biodiversity. In *Encyclopedia of Biodiversity* (pp. 519–536). Elsevier. https://doi.org/10.1016/B978-0-12-384719-5.00366-X

Clow, D. W., Roop, H. A., Nanus, L., Fenn, M. E., & Sexstone, G. A. (2015). Spatial patterns of atmospheric deposition of nitrogen and sulfur using ion-exchange resin collectors in Rocky Mountain National Park, USA. *Atmospheric Environment*, *101*, 149–157. https://doi.org/10.1016/j.atmosenv.2014.11.027

Colucci, R. R., Giorgi, F., & Torma, C. (2017). Unprecedented heat wave in December 2015 and potential for winter glacier ablation in the eastern Alps. *Scientific Reports*, *7*(1), 7090. https://doi.org/10.1038/s41598-017-07415-1

Coppola, E., Stocchi, P., Pichelli, E., Torres Alavez, J. A., Glazer, R., Giuliani, G., et al. (2021). Non-Hydrostatic RegCM4 (RegCM4-NH): model description and case studies over multiple domains. *Geoscientific Model Development*, *14*(12), 7705–7723. https://doi.org/10.5194/gmd-14-7705-2021

Coumou, D., & Rahmstorf, S. (2012). A decade of weather extremes. *Nature Climate Change*, *2*(7), 491–496. https://doi.org/10.1038/nclimate1452

Crutzen, P. J. (2006). Albedo Enhancement by Stratospheric Sulfur Injections: A Contribution to Resolve a Policy Dilemma? *Climatic Change*, *77*(3), 211–220. https://doi.org/10.1007/s10584-006-9101-y

Daly, C., Halbleib, M., Smith, J. I., Gibson, W. P., Doggett, M. K., Taylor, G. H., et al. (2008). Physiographically sensitive mapping of climatological temperature and precipitation across the conterminous United States. *International Journal of Climatology*, *28*(15), 2031–2064. https://doi.org/10.1002/joc.1688

Davidson, E. A., & Janssens, I. A. (2006). Temperature sensitivity of soil carbon decomposition and feedbacks to climate change. *Nature*, *440*(7081), 165–173. https://doi.org/10.1038/nature04514

Deng, L., Peng, C., Kim, D.-G., Li, J., Liu, Y., Hai, X., et al. (2021). Drought effects on soil carbon and nitrogen dynamics in global natural ecosystems. *Earth-Science Reviews*, *214*, 103501. https://doi.org/10.1016/j.earscirev.2020.103501

Dentener, F., Drevet, J., Lamarque, J. F., Bey, I., Eickhout, B., Fiore, A. M., et al. (2006). Nitrogen and sulfur deposition on regional and global scales: A multimodel evaluation. *Global Biogeochemical Cycles*, *20*(4). https://doi.org/10.1029/2005GB002672

Dierauer, J. R., Allen, D. M., & Whitfield, P. H. (2019). Snow Drought Risk and Susceptibility in the Western United States and Southwestern Canada. *Water Resources Research*, *55*(4), 3076–3091. https://doi.org/10.1029/2018WR023229

Dise, N. B., & Stevens, J. (2005). Nitrogen deposition and reduction of terrestrial biodiversity: Evidence from temperate grasslands. *Science in China Series C: Life Sciences*, *48*(2), 720–728. https://doi.org/10.1007/BF03187112

Dixon, K. W., Lanzante, J. R., Nath, M. J., Hayhoe, K., Stoner, A., Radhakrishnan, A., et al. (2016). Evaluating the stationarity assumption in statistically downscaled climate projections: is past performance an indicator of future results? *Climatic Change*, *135*(3), 395–408. https://doi.org/10.1007/s10584-016-1598-0

Domke, G. M., Perry, C. H., Walters, B. F., Nave, L. E., Woodall, C. W., & Swanston, C. W. (2017). Toward inventory-based estimates of soil organic carbon in forests of the United States. *Ecological Applications*, *27*(4), 1223–1235. https://doi.org/10.1002/eap.1516

Doney, S. C., Mahowald, N., Lima, I., Feely, R. A., Mackenzie, F. T., Lamarque, J.-F., & Rasch, P. J. (2007). Impact of anthropogenic atmospheric nitrogen and sulfur deposition on ocean acidification and the inorganic carbon system. *Proceedings of the National Academy of Sciences*, *104*(37), 14580–14585. https://doi.org/10.1073/pnas.0702218104

Driscoll, C. T., Lawrence, G. B., Bulger, A. J., Butler, T. J., Cronan, C. S., Eagar, C., et al. (2001). Acidic Deposition in the Northeastern United States: Sources and Inputs, Ecosystem Effects, and Management Strategies: The effects of acidic deposition in the northeastern United States include the acidification of soil and water, which stresses terrestrial and aquatic biota. *BioScience*, *51*(3), 180–198. https://doi.org/10.1641/0006-3568(2001)051[0180:ADITNU]2.0.CO;2

Eastham, S. D., Weisenstein, D. K., Keith, D. W., & Barrett, S. R. H. (2018). Quantifying the impact of sulfate geoengineering on mortality from air quality and UV-B exposure. *Atmospheric Environment*, *187*, 424–434. https://doi.org/10.1016/j.atmosenv.2018.05.047

Elder, M., & Zusman, E. (2016). *Strengthening the Linkages Between Air Pollution and the Sustainable Development Goals* (Technical Report No. 35) (p. 11). Institute for Global Environmental Strategies. Retrieved from https://www.researchgate.net/publication/305116520_Strengthening_The_Linkages_Between_Air_Pollution_And_The_Sustainable_Development_Goals

EMEP. (2021). European Monitoring and Evaluation Prgrarmme (EMEP). Retrieved November 18, 2021, from https://www.emep.int/

Environment and Climate Change Canada. (2017, November 30). Canadian Air and Precipitation Monitoring Network [program descriptions]. Retrieved November 18, 2021, from https://www.canada.ca/en/environment-climate-change/services/air-pollution/monitoring-networks-data/canadian-air-precipitation.html

European Drought Observatory. (2018). *Heat and Cold Wave Index* (Factsheet) (p. 5). European Comission. Retrieved from https://edo.jrc.ec.europa.eu/documents/factsheets/factsheet_heatColdWaveIndex.pdf

European Space Agency. (2022). Soil Moisture [Overviews and Factsheets]. Retrieved April 15, 2024, from https://climate.esa.int/en/projects/soil-moisture/

Eyring, V., Bony, S., Meehl, G. A., Senior, C. A., Stevens, B., Stouffer, R. J., & Taylor, K. E. (2016). Overview of the Coupled Model Intercomparison Project Phase 6 (CMIP6) experimental design and organization. *Geoscientific Model Development*, *9*(5), 1937–1958. https://doi.org/10.5194/gmd-9-1937-2016

Feeney, C. J., Cosby, B. J., Robinson, D. A., Thomas, A., Emmett, B. A., & Henrys, P. (2022). Multiple soil map comparison highlights challenges for predicting topsoil organic carbon concentration at national scale. *Scientific Reports*, *12*(1), 1379. https://doi.org/10.1038/s41598-022-05476-5

Fenn, M. E., Baron, J., Allen, E. B., Rueth, H. M., Nydick, K. R., Geiser, L., et al. (2003). Ecological effects of nitrogen deposition in the western United States. *BioScience*, *53*(4), 404–420. https://doi.org/10.1641/0006-3568(2003)053[0404:EEONDI]2.0.CO;2

Fioletov, V. E., McLinden, C. A., Krotkov, N., Li, C., Joiner, J., Theys, N., et al. (2016). A global catalogue of large SO_2 sources and emissions derived from the Ozone Monitoring Instrument. *Atmospheric Chemistry and Physics*, *16*(18), 11497–11519. https://doi.org/10.5194/acp-16-11497-2016

Fiorini, A. C. O., Angelkorte, G., Maia, P. L., Bergman-Fonte, C., Vicente, C., Morais, T., et al. (2023). Sustainable aviation fuels must control induced land use change: an integrated assessment modelling exercise for Brazil. *Environmental Research Letters*, *18*(1), 014036. https://doi.org/10.1088/1748-9326/acaee1

Fischer, E. M., & Schär, C. (2010). Consistent geographical patterns of changes in high-impact European heatwaves. *Nature Geoscience*, *3*(6), 398–403. https://doi.org/10.1038/ngeo866

Fisher, B. E. A. (1975). The long range transport of sulphur dioxide. *Atmospheric Environment (1967)*, *9*(12), 1063–1070. https://doi.org/10.1016/0004-6981(75)90180-8

Flanigan, N. P., Bandara, R., Wang, F., Jastrzębowski, S., Hidayati, S. N., & Walck, J. L. (2020). Germination responses to winter warm spells and warming vary widely among woody plants in a temperate forest. *Plant Biology*, *22*(6), 1052–1061. https://doi.org/10.1111/plb.13152

Fowler, A. F., Basso, B., Millar, N., & Brinton, W. F. (2023). A simple soil mass correction for a more accurate determination of soil carbon stock changes. *Scientific Reports*, *13*(1), 2242. https://doi.org/10.1038/s41598-023-29289-2

Frank, D., Reichstein, M., Bahn, M., Thonicke, K., Frank, D., Mahecha, M. D., et al. (2015). Effects of climate extremes on the terrestrial carbon cycle: concepts, processes and potential future impacts. *Global Change Biology*, *21*(8), 2861–2880. https://doi.org/10.1111/gcb.12916

Frich, P., Alexander, L. V., Della-Marta, P., Gleason, B., Haylock, M., Tank, A. M. G. K., & Peterson, T. (2002). Observed coherent changes in climatic extremes during the second half of the twentieth century. *Climate Research*, *19*(3), 193–212. https://doi.org/10.3354/cr019193

Friedlingstein, P., O'Sullivan, M., Jones, M. W., Andrew, R. M., Hauck, J., Olsen, A., et al. (2020). Global Carbon Budget 2020. *Earth System Science Data*, *12*(4), 3269–3340. https://doi.org/10.5194/essd-12-3269-2020

Fu, J. S., Carmichael, G. R., Dentener, F., Aas, W., Andersson, C., Barrie, L. A., et al. (2022). Improving Estimates of Sulfur, Nitrogen, and Ozone Total Deposition through Multi-Model and Measurement-Model Fusion Approaches. *Environmental Science & Technology*, *56*(4), 2134–2142. https://doi.org/10.1021/acs.est.1c05929

Galloway, J. N. (1995). Acid deposition: Perspectives in time and space. *Water, Air, and Soil Pollution*, *85*(1), 15–24. https://doi.org/10.1007/BF00483685

Galy-Lacaux, C., Delon, C., Solmon, F., Adon, M., Yoboué, V., Mphepya, J., et al. (2014). Dry and Wet Atmospheric Nitrogen Deposition in West Central Africa. In M. A. Sutton, K. E. Mason, L. J. Sheppard, H. Sverdrup, R. Haeuber, & W. K. Hicks (Eds.), *Nitrogen Deposition, Critical Loads and Biodiversity* (pp. 83–91). Dordrecht: Springer Netherlands. https://doi.org/10.1007/978-94-007-7939-6_10

Gao, Y., Fu, J. S., Drake, J. B., Liu, Y., & Lamarque, J.-F. (2012). Projected changes of extreme weather events in the eastern United States based on a high resolution climate modeling system. *Environmental Research Letters*, *7*(4), 044025. https://doi.org/10.1088/1748-9326/7/4/044025

Gautam, S., Mishra, U., Scown, C. D., Wills, S. A., Adhikari, K., & Drewniak, B. A. (2022). Continental United States may lose 1.8 petagrams of soil organic carbon under climate change by 2100. *Global Ecology and Biogeography*, *31*(6), 1147–1160. https://doi.org/10.1111/geb.13489

Ge, J., Xu, W., Liu, Q., Tang, Z., & Xie, Z. (2020). Patterns and environmental controls of soil organic carbon density in Chinese shrublands. *Geoderma*, *363*, 114161. https://doi.org/10.1016/j.geoderma.2019.114161

Ge, X., Yu, Q., Duan, L., Zhao, Y., Posch, M., & Hao, J. (2023). High-resolution maps of critical loads for sulfur and nitrogen in China. *Scientific Data*, *10*(1), 339. https://doi.org/10.1038/s41597-023-02178-z

Geddes, J. A., & Martin, R. V. (2017). Global deposition of total reactive nitrogen oxides from 1996 to 2014 constrained with satellite observations of NO_2 columns. *Atmospheric Chemistry and Physics*, *17*(16), 10071–10091. https://doi.org/10.5194/acp-17-10071-2017

Geddes, J. A., Murphy, J. G., O'Brien, J. M., & Celarier, E. A. (2012). Biases in long-term NO2 averages inferred from satellite observations due to cloud selection criteria. *Remote Sensing of Environment*, *124*, 210–216. https://doi.org/10.1016/j.rse.2012.05.008

Gehlke, C. E., & Biehl, K. (1934). Certain Effects of Grouping upon the Size of the Correlation Coefficient in Census Tract Material. *Journal of the American Statistical Association*, *29*(185A), 169-170].

Geiser, L. H., Root, H., Smith, R. J., Jovan, S. E., St Clair, L., & Dillman, K. L. (2021). Lichen-based critical loads for deposition of nitrogen and sulfur in US forests. *Environmental Pollution*, *291*, 118187. https://doi.org/10.1016/j.envpol.2021.118187

Gholizadeh, A., Žižala, D., Saberioon, M., & Borůvka, L. (2018). Soil organic carbon and texture retrieving and mapping using proximal, airborne and Sentinel-2 spectral imaging. *Remote Sensing of Environment*, *218*, 89–103. https://doi.org/10.1016/j.rse.2018.09.015

Grace, P. R., Colunga-Garcia, M., Gage, S. H., Robertson, G. P., & Safir, G. R. (2006). The Potential Impact of Agricultural Management and Climate Change on Soil Organic Carbon of the North Central Region of the United States. *Ecosystems*, *9*(5), 816–827. https://doi.org/10.1007/s10021-004-0096-9

Gregorich, E. G., Janzen, H., Ellert, B. H., Helgason, B. L., Qian, B., Zebarth, B. J., et al. (2017). Litter decay controlled by temperature, not soil properties, affecting future soil carbon. *Global Change Biology*, *23*(4), 1725–1734. https://doi.org/10.1111/gcb.13502

Gu, L., Baldocchi, D. D., Wofsy, S. C., Munger, J. W., Michalsky, J. J., Urbanski, S. P., & Boden, T. A. (2003). Response of a Deciduous Forest to the Mount Pinatubo Eruption:

Enhanced Photosynthesis. *Science*, *299*(5615), 2035–2038. https://doi.org/10.1126/science.1078366

Guan, S., Zhang, X., Zhao, W., Duan, Y., Yang, S., Yao, Y., & Jia, K. (2023). A similarity distance-based space-time random forest model for estimating PM2.5 concentrations over China. *Atmospheric Environment*, *313*, 120043. https://doi.org/10.1016/j.atmosenv.2023.120043

Guevara, M., Arroyo-Cruz, C. E., Brunsell, N., Cruz-Gaistardo, C. O., Domke, G. M., Equihua, J., et al. (2020). Soil Organic Carbon Estimates for 30-cm Depth, Mexico and Conterminous USA, 1991-2011. *ORNL DAAC*. https://doi.org/10.3334/ORNLDAAC/1737

Guevara, Mario, Arroyo, C., Brunsell, N., Cruz, C. O., Domke, G., Equihua, J., et al. (2020). Soil Organic Carbon Across Mexico and the Conterminous United States (1991–2010). *Global Biogeochemical Cycles*, *34*(3), e2019GB006219. https://doi.org/10.1029/2019GB006219

Guo, B., Zhang, D., Pei, L., Su, Y., Wang, X., Bian, Y., et al. (2021). Estimating PM2.5 concentrations via random forest method using satellite, auxiliary, and ground-level station dataset at multiple temporal scales across China in 2017. *Science of The Total Environment*, *778*, 146288. https://doi.org/10.1016/j.scitotenv.2021.146288

Guo, H., Du, E., Terrer, C., & Jackson, R. B. (2024). Global distribution of surface soil organic carbon in urban greenspaces. *Nature Communications*, *15*(1), 806. https://doi.org/10.1038/s41467-024-44887-y

Hargrove, W. W., & Hoffman, F. M. (2004). Potential of Multivariate Quantitative Methods for Delineation and Visualization of Ecoregions. *Environmental Management*, *34*(1), S39–S60. https://doi.org/10.1007/s00267-003-1084-0

Hargrove, W. W., Hoffman, F. M., & Hessburg, P. F. (2006). Mapcurves: a quantitative method for comparing categorical maps. *Journal of Geographical Systems*, *8*(2), 187. https://doi.org/10.1007/s10109-006-0025-x

He, C., Kim, H., Hashizume, M., Lee, W., Honda, Y., Kim, S. E., et al. (2022). The effects of night-time warming on mortality burden under future climate change scenarios: a modelling study. *The Lancet Planetary Health*, *6*(8), e648–e657. https://doi.org/10.1016/S2542-5196(22)00139-5

Heisler, J., Glibert, P. M., Burkholder, J. M., Anderson, D. M., Cochlan, W., Dennison, W. C., et al. (2008). Eutrophication and harmful algal blooms: A scientific consensus. *Harmful Algae*, *8*(1), 3–13. https://doi.org/10.1016/j.hal.2008.08.006

Hengl, T., Mendes De Jesus, J., Heuvelink, G. B. M., Ruiperez Gonzalez, M., Kilibarda, M., Blagotić, A., et al. (2017). SoilGrids250m: Global gridded soil information based on machine learning. *PLOS ONE*, *12*(2), e0169748. https://doi.org/10.1371/journal.pone.0169748

Hepburn, C., Adlen, E., Beddington, J., Carter, E. A., Fuss, S., Mac Dowell, N., et al. (2019). The technological and economic prospects for CO2 utilization and removal. *Nature*, *575*(7781), 87–97. https://doi.org/10.1038/s41586-019-1681-6

Heuvelink, G. B. M., Angelini, M. E., Poggio, L., Bai, Z., Batjes, N. H., van den Bosch, R., et al. (2021). Machine learning in space and time for modelling soil organic carbon change. *European Journal of Soil Science*, *72*(4), 1607–1623. https://doi.org/10.1111/ejss.12998

Hewitson, B. C., & Crane. (1996). Climate downscaling: techniques and application. *Climate Research*, *7*, 85–95.

Huang, Y., Jiang, N., Shen, M., & Guo, L. (2020). Effect of preseason diurnal temperature range on the start of vegetation growing season in the Northern Hemisphere. *Ecological Indicators*, *112*, 106161. https://doi.org/10.1016/j.ecolind.2020.106161

Huntzinger, D. N., Michalak, A. M., Schwalm, C., Ciais, P., King, A. W., Fang, Y., et al. (2017). Uncertainty in the response of terrestrial carbon sink to environmental drivers undermines carbon-climate feedback predictions. *Scientific Reports*, *7*(1), 4765. https://doi.org/10.1038/s41598-017-03818-2

Institut National des Sciences de l'Univers. (2021). INDAAF – International Network to study Deposition and Atmospheric chemistry in AFrica. Retrieved November 18, 2021, from https://indaaf.obs-mip.fr/

Intergovernmental Panel on Climate Change. (2012). *Managing the Risks of Extreme Events and Disasters to Advance Climate Change Adaptation.* (Special Report of Working Groups I and II of the Intergovernmental Panel on Climate Change) (p. 582). Cambridge, UK and New York, NY, USA: Cambridge University Press.

IPCC. (2019). 2019 Refinement to the 2006 IPCC Guidelines for National Greenhouse Gas Inventories. IPCC. Retrieved from https://www.ipcc-nggip.iges.or.jp/

IPCC. (2022). *Climate Change 2022: Impacts, Adaptation and Vulnerability* (Scientific Investigations Report). Cambridge University Press: IPCC.

Irvine, P., Emanuel, K., He, J., Horowitz, L. W., Vecchi, G., & Keith, D. (2019). Halving warming with idealized solar geoengineering moderates key climate hazards. *Nature Climate Change*, *9*(4), 295–299. https://doi.org/10.1038/s41558-019-0398-8

Irvine, P. J., & Keith, D. W. (2020). Halving warming with stratospheric aerosol geoengineering moderates policy-relevant climate hazards. *Environmental Research Letters*, *15*(4), 044011. https://doi.org/10.1088/1748-9326/ab76de

Jang, S., & Kavvas, M. L. (2015). Downscaling Global Climate Simulations to Regional Scales: Statistical Downscaling versus Dynamical Downscaling. *Journal of Hydrologic Engineering*, *20*(1), A4014006. https://doi.org/10.1061/(ASCE)HE.1943-5584.0000939

Jia, Y., Yu, G., He, N., Zhan, X., Fang, H., Sheng, W., et al. (2014). Spatial and decadal variations in inorganic nitrogen wet deposition in China induced by human activity. *Scientific Reports*, *4*(1), 3763. https://doi.org/10.1038/srep03763

Kanamitsu, M., Ebisuzaki, W., Woollen, J., Yang, S.-K., Hnilo, J. J., Fiorino, M., & Potter, G. L. (2002). NCEP–DOE AMIP-II Reanalysis (R-2). *Bulletin of the American Meteorological Society*, *83*(11), 1631–1644. https://doi.org/10.1175/BAMS-83-11-1631

Kicklighter, D. W., Melillo, J. M., Monier, E., Sokolov, A. P., & Zhuang, Q. (2019). Future nitrogen availability and its effect on carbon sequestration in Northern Eurasia. *Nature Communications*, *10*(1), 3024. https://doi.org/10.1038/s41467-019-10944-0

Kiktev, D., Sexton, D. M. H., Alexander, L., & Folland, C. K. (2003). Comparison of Modeled and Observed Trends in Indices of Daily Climate Extremes. *Journal of Climate*, *16*(22), 3560–3571. https://doi.org/10.1175/1520-0442(2003)016<3560:COMAOT>2.0.CO;2

Klöwer, M., Allen, M. R., Lee, D. S., Proud, S. R., Gallagher, L., & Skowron, A. (2021). Quantifying aviation's contribution to global warming. *Environmental Research Letters*, *16*(10), 104027. https://doi.org/10.1088/1748-9326/ac286e

Kortetmäki, T., & Oksanen, M. (2023). Right to Food and Geoengineering. *Journal of Agricultural and Environmental Ethics*, *36*(1), 5. https://doi.org/10.1007/s10806-023-09898-7

Kravitz, B., Robock, A., Tilmes, S., Boucher, O., English, J. M., Irvine, P. J., et al. (2015). The Geoengineering Model Intercomparison Project Phase 6 (GeoMIP6): simulation design and preliminary results. *Geoscientific Model Development*, *8*(10), 3379–3392. https://doi.org/10.5194/gmd-8-3379-2015

Kravitz, Ben, Robock, A., Boucher, O., Schmidt, H., Taylor, K. E., Stenchikov, G., & Schulz, M. (2011). The Geoengineering Model Intercomparison Project (GeoMIP). *Atmospheric Science Letters*, *12*(2), 162–167. https://doi.org/10.1002/asl.316

Kreyling, J., Schuerings, J., Malyshev, A. V., Vogt, L., Werner, C., & Jentsch, A. (2015). Nitrogen leaching is enhanced after a winter warm spell but mainly controlled by vegetation composition in temperate zone mesocosms. *Plant and Soil*, *396*(1), 85–96. https://doi.org/10.1007/s11104-015-2587-1

Krotkov, N. A., McLinden, C. A., Li, C., Lamsal, L. N., Celarier, E. A., Marchenko, S. V., et al. (2016). Aura OMI observations of regional SO₂ and NO₂ pollution changes from 2005 to 2015. *Atmospheric Chemistry and Physics*, *16*(7), 4605–4629. https://doi.org/10.5194/acp-16-4605-2016

Labrador, L., Volosciuk, C., & Cole, A. (2020). *Measurement-Model Fusion for Global Total Atmospheric Deposition, a WMO initiative* (Factsheet No. 69). World Meteorological Organization. Retrieved from https://public.wmo.int/en/resources/bulletin/measurement-model-fusion-global-total-atmospheric-deposition-wmo-initiative

Lafferty, D. C., & Sriver, R. L. (2023). Downscaling and bias-correction contribute considerable uncertainty to local climate projections in CMIP6. *Npj Climate and Atmospheric Science*, *6*(1), 1–13. https://doi.org/10.1038/s41612-023-00486-0

Lamarque, J.-F., Dentener, F., McConnell, J., Ro, C.-U., Shaw, M., Vet, R., et al. (2013). Multi-model mean nitrogen and sulfur deposition from the Atmospheric Chemistry and Climate Model Intercomparison Project (ACCMIP): evaluation of historical and projected future changes. *Atmospheric Chemistry and Physics*, *13*(16), 7997–8018. https://doi.org/10.5194/acp-13-7997-2013

Langlois, N., Herbst, J., Mason, K., Nairn, J., & Byard, R. W. (2013). Using the Excess Heat Factor (EHF) to predict the risk of heat related deaths. *Journal of Forensic and Legal Medicine*, *20*(5), 408–411. https://doi.org/10.1016/j.jflm.2012.12.005

Lanning, M., Wang, L., Scanlon, T. M., Vadeboncoeur, M. A., Adams, M. B., Epstein, H. E., & Druckenbrod, D. (2019). Intensified vegetation water use under acid deposition. *Science Advances*, *5*(7), eaav5168. https://doi.org/10.1126/sciadv.aav5168

Larssen, T., & Carmichael, G. R. (2000). Acid rain and acidification in China: the importance of base cation deposition. *Environmental Pollution*, *110*(1), 89–102. https://doi.org/10.1016/S0269-7491(99)00279-1

Latysh, N. E., & Wetherbee, G. A. (2012). Improved mapping of National Atmospheric Deposition Program wet-deposition in complex terrain using PRISM-gridded data sets. *Environmental Monitoring and Assessment*, *184*(2), 913–928. https://doi.org/10.1007/s10661-011-2009-7

Lavaysse, C., Cammalleri, C., Dosio, A., van der Schrier, G., Toreti, A., & Vogt, J. (2018). Towards a monitoring system of temperature extremes in Europe. *Natural Hazards and Earth System Sciences*, *18*(1), 91–104. https://doi.org/10.5194/nhess-18-91-2018

Lawrence, M. G., Schäfer, S., Muri, H., Scott, V., Oschlies, A., Vaughan, N. E., et al. (2018). Evaluating climate geoengineering proposals in the context of the Paris Agreement temperature goals. *Nature Communications*, *9*(1), 3734. https://doi.org/10.1038/s41467-018-05938-3

Lee, D. S., Fahey, D. W., Skowron, A., Allen, M. R., Burkhardt, U., Chen, Q., et al. (2021). The contribution of global aviation to anthropogenic climate forcing for 2000 to 2018. *Atmospheric Environment*, *244*, 117834. https://doi.org/10.1016/j.atmosenv.2020.117834

Lee, Walker, MacMartin, D., Visioni, D., & Kravitz, B. (2020). *Expanding the Design Space of Stratospheric Aerosol Geoengineering to Include Precipitation-Based Objectives and Explore Trade-offs* (preprint). Management of the Earth system: engineering responses to climate change. https://doi.org/10.5194/esd-2020-58

Lee, Whanhee, Kim, Y., Sera, F., Gasparrini, A., Park, R., Michelle Choi, H., et al. (2020). Projections of excess mortality related to diurnal temperature range under climate change scenarios: a multi-country modelling study. *The Lancet Planetary Health*, *4*(11), e512–e521. https://doi.org/10.1016/S2542-5196(20)30222-9

Levelt, P. F., van den Oord, G. H. J., Dobber, M. R., Malkki, A., Visser, H., Vries, J. de, et al. (2006). The ozone monitoring instrument. *IEEE Transactions on Geoscience and Remote Sensing*, *44*(5), 1093–1101. https://doi.org/10.1109/TGRS.2006.872333

Li, C., Joiner, J., Krotkov, N. A., & Bhartia, P. K. (2013). A fast and sensitive new satellite SO2 retrieval algorithm based on principal component analysis: Application to the ozone monitoring instrument. *Geophysical Research Letters*, *40*(23), 6314–6318. https://doi.org/10.1002/2013GL058134

Li, H., Shen, H., Chen, L., Liu, T., Hu, H., Zhao, X., et al. (2016). Effects of shrub encroachment on soil organic carbon in global grasslands. *Scientific Reports*, *6*, 28974. https://doi.org/10.1038/srep28974

Li, R., Cui, L., Zhao, Y., Zhang, Z., Sun, T., Li, J., et al. (2019). Wet deposition of inorganic ions in 320 cities across China: spatio-temporal variation, source apportionment, and dominant factors. *Atmospheric Chemistry and Physics*, *19*(17), 11043–11070. https://doi.org/10.5194/acp-19-11043-2019

Lin, Z., Dai, Y., Mishra, U., Wang, G., Shangguan, W., Zhang, W., & Qin, Z. (2023). Global and regional soil organic carbon estimates: Magnitude and uncertainties. *Pedosphere*. https://doi.org/10.1016/j.pedsph.2023.06.005

Lindvall, J., & Svensson, G. (2015). The diurnal temperature range in the CMIP5 models. *Climate Dynamics*, *44*(1), 405–421. https://doi.org/10.1007/s00382-014-2144-2

Liu, J., Yuan, F., Zuo, Y., Zhou, R., Zhu, X., Li, K., et al. (2022). Warming-induced vegetation growth cancels out soil carbon-climate feedback in the northern Asian permafrost region in the 21st century. *Environmental Research Letters*, *17*(8), 084009. https://doi.org/10.1088/1748-9326/ac7eda

Liu, L., Zhang, X., Xu, W., Liu, X., Zhang, Y., Li, Y., et al. (2020). Fall of oxidized while rise of reduced reactive nitrogen deposition in China. *Journal of Cleaner Production*, *272*, 122875. https://doi.org/10.1016/j.jclepro.2020.122875

Liu, L., Yang, Y., Xi, R., Zhang, X., Xu, W., Liu, X., et al. (2021). Global Wet-Reduced Nitrogen Deposition Derived From Combining Satellite Measurements With Output From a Chemistry Transport Model. *Journal of Geophysical Research: Atmospheres*, *126*(4), e2020JD033977. https://doi.org/10.1029/2020JD033977

Liu, S., Wei, Y., Post, W. M., Cook, R. B., Schaefer, K., & Thornton, M. M. (2014). NACP MsTMIP: Unified North American Soil Map. *ORNL DAAC*. https://doi.org/10.3334/ORNLDAAC/1242

Liu, Z., Kimball, J. S., Parazoo, N. C., Ballantyne, A. P., Wang, W. J., Madani, N., et al. (2020). Increased high-latitude photosynthetic carbon gain offset by respiration carbon loss during an anomalous warm winter to spring transition. *Global Change Biology*, *26*(2), 682–696. https://doi.org/10.1111/gcb.14863

Lohmann, J., Castellana, D., Ditlevsen, P. D., & Dijkstra, H. A. (2021). Abrupt climate change as a rate-dependent cascading tipping point. *Earth System Dynamics*, *12*(3), 819–835. https://doi.org/10.5194/esd-12-819-2021

Long, J. C. S., & Shepherd, J. G. (2014). The Strategic Value of Geoengineering Research. In B. Freedman (Ed.), *Global Environmental Change* (pp. 757–770). Dordrecht: Springer Netherlands. https://doi.org/10.1007/978-94-007-5784-4_24

Lu, Z., Streets, D. G., Zhang, Q., Wang, S., Carmichael, G. R., Cheng, Y. F., et al. (2010). Sulfur dioxide emissions in China and sulfur trends in East Asia since 2000. *Atmospheric Chemistry and Physics*, *10*(13), 6311–6331. https://doi.org/10.5194/acp-10-6311-2010

Luo, M., & Lau, N.-C. (2020). Summer heat extremes in northern continents linked to developing ENSO events. *Environmental Research Letters*, *15*(7), 074042. https://doi.org/10.1088/1748-9326/ab7d07

Luo, X. S., Tang, A. H., Shi, K., Wu, L. H., Li, W. Q., Shi, W. Q., et al. (2014). Chinese coastal seas are facing heavy atmospheric nitrogen deposition. *Environmental Research Letters*, *9*(9), 095007. https://doi.org/10.1088/1748-9326/9/9/095007

Luo, Y., Ahlström, A., Allison, S. D., Batjes, N. H., Brovkin, V., Carvalhais, N., et al. (2016). Toward more realistic projections of soil carbon dynamics by Earth system models. *Global Biogeochemical Cycles*, *30*(1), 40–56. https://doi.org/10.1002/2015GB005239

Matthew Ballew, Marlon, J., Rosenthal, S., Carman, J., Kotcher, J., Maibach, E., & Leiserowitz, A. (2023). Americans are growing more worried about extreme heat. *Yale Program on Climate Change Communication*. Retrieved from https://climatecommunication.yale.edu/publications/worry-about-extreme-heat/

Maurer, E. P., & Pierce, D. W. (2014). Bias correction can modify climate model simulated precipitation changes without adverse effect on the ensemble mean. *Hydrology and Earth System Sciences*, *18*(3), 915–925. https://doi.org/10.5194/hess-18-915-2014

Mazdiyasni, O., AghaKouchak, A., Davis, S. J., Madadgar, S., Mehran, A., Ragno, E., et al. (2017). Increasing probability of mortality during Indian heat waves. *Science Advances*, *3*(6), e1700066. https://doi.org/10.1126/sciadv.1700066

Mazdiyasni, O., Sadegh, M., Chiang, F., & AghaKouchak, A. (2019). Heat wave Intensity Duration Frequency Curve: A Multivariate Approach for Hazard and Attribution Analysis. *Scientific Reports*, *9*(1), 14117. https://doi.org/10.1038/s41598-019-50643-w

McLinden, C. A., Fioletov, V., Boersma, K. F., Kharol, S. K., Krotkov, N., Lamsal, L., et al. (2014). Improved satellite retrievals of NO₂ and SO₂ over the Canadian oil sands and comparisons with surface measurements. *Atmospheric Chemistry and Physics*, *14*(7), 3637–3656. https://doi.org/10.5194/acp-14-3637-2014

McMurray, J. A., McDonnell, T. C., Mebane, A., & Pardo, L. (2021). *Assessment of Atmospheric Nitrogen and Sulfur Deposition Critical Loads for Aquatic and Terrestrial Resources on National Forest System Lands in the Intermountain Region* (Technical Report No. NRS-204) (p. 308). Madison, WI: U.S. Department of Agriculture, Forest Service, Northern Research Station. Retrieved from https://doi. org/10.2737/NRS-GTR-204

Melnikova, I., Boucher, O., Cadule, P., Ciais, P., Gasser, T., Quilcaille, Y., et al. (2021). Carbon Cycle Response to Temperature Overshoot Beyond 2°C: An Analysis of CMIP6 Models - Melnikova - 2021 - Earth's Future - Wiley Online Library. *Earth's Future*, *9*(5). https://doi.org/10.1029/2020EF001967

Mendoza Paz, S., & Willems, P. (2023). The skill of statistical downscaling in future climate with high-resolution climate models as pseudo-reality. *Journal of Hydrology: Regional Studies*, *48*, 101477. https://doi.org/10.1016/j.ejrh.2023.101477

Mondal, A., Khare, D., Kundu, S., Mondal, S., Mukherjee, S., & Mukhopadhyay, A. (2017). Spatial soil organic carbon (SOC) prediction by regression kriging using remote sensing data. *The Egyptian Journal of Remote Sensing and Space Science*, *20*(1), 61–70. https://doi.org/10.1016/j.ejrs.2016.06.004

NADP. (2021). National Atmospheric Deposition Program. Retrieved November 18, 2021, from https://nadp.slh.wisc.edu/

Nahlik, A. M., & Fennessy, M. S. (2016). Carbon storage in US wetlands. *Nature Communications*, *7*(1), 13835. https://doi.org/10.1038/ncomms13835

Nairn, J., Fawcett, R., & Ray, D. (2009). Australian Bureau of Meteorology. Australian Bureau of Meteorology.

Nairn, J. R., & Fawcett, R. J. B. (2015). The Excess Heat Factor: A Metric for Heatwave Intesity and its Use in Classifying Heatwave Severity. *International Journal of Environmental Research and Public Health*, (12), 227–253.

NASA. (2011). Tropical Rainfall Measuring Mission (TRMM). Goddard Earth Sciences Data and Information Services Center (GES DISC). Retrieved from https://disc.gsfc.nasa.gov/datasets/TRMM_3B43_7/summary

National Research Council. (2015). *Climate Intervention: Reflecting Sunlight to Cool Earth*. https://doi.org/10.17226/18988

Nave, L., Johnson, K., van Ingen, C., Agarwal, D., Humphrey, M., & Beekwilder, N. (2016). *International Soil Carbon Network (ISCN) Database v3-1*. International Soil Carbon Network (ISCN). https://doi.org/10.17040/ISCN/1305039

Nave, L. E., DeLyser, K., Domke, G. M., Holub, S. M., Janowiak, M. K., Ontl, T. A., et al. (2022). Soil carbon in the South Atlantic United States: Land use change, forest management, and physiographic context. *Forest Ecology and Management*, *520*, 120410. https://doi.org/10.1016/j.foreco.2022.120410

NCAR, & UCAR. (2022, March). Community Earth System Model - CESM®. Retrieved March 10, 2022, from http://www.cesm.ucar.edu

Niemeier, U., & Timmreck, C. (2015). What is the limit of climate engineering by stratospheric injection of SO_2? *Atmospheric Chemistry and Physics*, *15*(16), 9129–9141. https://doi.org/10.5194/acp-15-9129-2015

NIH. (2022). Effects of Heat - Climate and Human Health [Overviews and Factsheets]. Retrieved March 10, 2022, from https://www.niehs.nih.gov/research/programs/climatechange/health_impacts/heat/index.cfm

Nilsson, J. (1988). Critical Loads for Sulphur and Nitrogen. In P. Mathy (Ed.), *Air Pollution and Ecosystems* (pp. 85–91). Dordrecht: Springer Netherlands. https://doi.org/10.1007/978-94-009-4003-1_11

O'Byrne, G., Martin, R. V., van Donkelaar, A., Joiner, J., & Celarier, E. A. (2010). Surface reflectivity from the Ozone Monitoring Instrument using the Moderate Resolution Imaging Spectroradiometer to eliminate clouds: Effects of snow on ultraviolet and visible trace gas retrievals. *Journal of Geophysical Research: Atmospheres*, *115*(D17). https://doi.org/10.1029/2009JD013079

O'Neill, B. C., Tebaldi, C., van Vuuren, D. P., Eyring, V., Friedlingstein, P., Hurtt, G., et al. (2016). The Scenario Model Intercomparison Project (ScenarioMIP) for CMIP6. *Geoscientific Model Development*, *9*(9), 3461–3482. https://doi.org/10.5194/gmd-9-3461-2016

Padilha, M. C. de C., Vicente, L. E., Demattê, J. A. M., dos Santos Wendriner Loebmann, D. G., Vicente, A. K., Salazar, D. F. U., & Guimarães, C. C. B. (2020). Using Landsat and soil clay content to map soil organic carbon of oxisols and Ultisols near São Paulo, Brazil. *Geoderma Regional*, *21*, e00253. https://doi.org/10.1016/j.geodrs.2020.e00253

Park, J.-E., Son, W.-S., Ryu, Y., Choi, S. B., Kwon, O., & Ahn, I. (2020). Effects of temperature, humidity, and diurnal temperature range on influenza incidence in a temperate region. *Influenza and Other Respiratory Viruses*, *14*(1), 11–18. https://doi.org/10.1111/irv.12682

Patton, N. R., Lohse, K. A., Seyfried, M. S., Godsey, S. E., & Parsons, S. B. (2019). Topographic controls of soil organic carbon on soil-mantled landscapes. *Scientific Reports*, *9*(1), 6390. https://doi.org/10.1038/s41598-019-42556-5

Paustian, K., Larson, E., Kent, J., Marx, E., & Swan, A. (2019). Soil C Sequestration as a Biological Negative Emission Strategy. *Frontiers in Climate*, *1*. Retrieved from https://www.frontiersin.org/article/10.3389/fclim.2019.00008

Pavlovic, N. R., Chang, S. Y., Huang, J., Craig, K., Clark, C., Horn, K., & Driscoll, C. T. (2023). Empirical nitrogen and sulfur critical loads of U.S. tree species and their uncertainties with machine learning. *Science of The Total Environment*, *857*, 159252. https://doi.org/10.1016/j.scitotenv.2022.159252

Peng, R. D., Bobb, J. F., Tebaldi, C., McDaniel, L., Bell, M. L., & Dominici, F. (2011). Toward a Quantitative Estimate of Future Heat Wave Mortality under Global Climate Change. *Environmental Health Perspectives*, *119*(5), 701–706. https://doi.org/10.1289/ehp.1002430

Perkins, S. E., & Alexander, L. V. (2013). On the Measurement of Heat Waves. *Journal of Climate*, *26*(13), 4500–4517. https://doi.org/10.1175/JCLI-D-12-00383.1

Pfleiderer, P., Schleussner, C.-F., Kornhuber, K., & Coumou, D. (2019). Summer weather becomes more persistent in a 2 °C world. *Nature Climate Change*, *9*(9), 666–671. https://doi.org/10.1038/s41558-019-0555-0

Philip, S. Y., Kew, S. F., van Oldenborgh, G. J., Anslow, F. S., Seneviratne, S. I., Vautard, R., et al. (2021). Rapid attribution analysis of the extraordinary heatwave on the Pacific Coast of the US and Canada June 2021. *Earth System Dynamics Discussions*, 1–34. https://doi.org/10.5194/esd-2021-90

Poggio, L., de Sousa, L. M., Batjes, N. H., Heuvelink, G. B. M., Kempen, B., Ribeiro, E., & Rossiter, D. (2021). SoilGrids 2.0: producing soil information for the globe with quantified spatial uncertainty. *SOIL*, *7*(1), 217–240. https://doi.org/10.5194/soil-7-217-2021

Provencher, L., Byer, S., Frid, L., Senthivasan, S., Badik, K. J., & Szabo, K. (2023). Carbon Sequestration in Degraded Intermountain West Rangelands, United States. *Rangeland Ecology & Management*, *90*, 22–34. https://doi.org/10.1016/j.rama.2023.05.004

Pye, H. O. T., Nenes, A., Alexander, B., Ault, A. P., Barth, M. C., Clegg, S. L., et al. (2020). The acidity of atmospheric particles and clouds. *Atmospheric Chemistry and Physics*, *20*(8), 4809–4888. https://doi.org/10.5194/acp-20-4809-2020

Qu, L., Xiao, H., Zheng, N., Zhang, Z., & Xu, Y. (2017). Comparison of four methods for spatial interpolation of estimated atmospheric nitrogen deposition in South China. *Environmental Science and Pollution Research*, *24*(3), 2578–2588. https://doi.org/10.1007/s11356-016-7995-0

R Core Team. (2022). R: A Language and Environment for Statistical Computing (Version 3.6.0). R Foundation for Statistical Computing. Retrieved from http://R-project.org/

Raei, E., Nikoo, M. R., AghaKouchak, A., Mazdiyasni, O., & Sadegh, M. (2018). GHWR, a multi-method global heatwave and warm-spell record and toolbox. *Scientific Data*, *5*(1), 180206. https://doi.org/10.1038/sdata.2018.206

Ramcharan, A., Hengl, T., Nauman, T., Brungard, C., Waltman, S., Wills, S., & Thompson, J. (2018). Soil Property and Class Maps of the Conterminous United States at 100-Meter Spatial Resolution. *Soil Science Society of America Journal*, *82*(1), 186–201. https://doi.org/10.2136/sssaj2017.04.0122

Rastogi, D., Kao, S.-C., & Ashfaq, M. (2022). How May the Choice of Downscaling Techniques and Meteorological Reference Observations Affect Future Hydroclimate Projections? *Earth's Future*, *10*(8), e2022EF002734. https://doi.org/10.1029/2022EF002734

Reichstein, M., Bahn, M., Ciais, P., Frank, D., Mahecha, M. D., Seneviratne, S. I., et al. (2013). Climate extremes and the carbon cycle. *Nature*, *500*(7462), 287–295. https://doi.org/10.1038/nature12350

Ren, W., Banger, K., Tao, B., Yang, J., Huang, Y., & Tian, H. (2020). Global pattern and change of cropland soil organic carbon during 1901-2010: Roles of climate, atmospheric chemistry, land use and management. *Geography and Sustainability*, *1*(1), 59–69. https://doi.org/10.1016/j.geosus.2020.03.001

Riahi, K., Rao, S., Krey, V., Cho, C., Chirkov, V., Fischer, G., et al. (2011). RCP 8.5—A scenario of comparatively high greenhouse gas emissions. *Climatic Change*, *109*(1), 33. https://doi.org/10.1007/s10584-011-0149-y

Riahi, K., van Vuuren, D. P., Kriegler, E., Edmonds, J., O'Neill, B. C., Fujimori, S., et al. (2017). The Shared Socioeconomic Pathways and their energy, land use, and greenhouse gas emissions implications: An overview. *Global Environmental Change*, *42*, 153–168. https://doi.org/10.1016/j.gloenvcha.2016.05.009

Robinson, S. I., O'Gorman, E. J., Frey, B., Hagner, M., & Mikola, J. (2022). Soil organic matter, rather than temperature, determines the structure and functioning of subarctic decomposer communities. *Global Change Biology*, *28*(12), 3929–3943. https://doi.org/10.1111/gcb.16158

Robiou du Pont, Y., & Meinshausen, M. (2018). Warming assessment of the bottom-up Paris Agreement emissions pledges. *Nature Communications*, *9*(1), 4810. https://doi.org/10.1038/s41467-018-07223-9

Rubin, H. J., Lutz, D. A., Steele, B. G., Cottingham, K. L., Weathers, K. C., Ducey, M. J., et al. (2021). Remote Sensing of Lake Water Clarity: Performance and Transferability of Both Historical Algorithms and Machine Learning. *Remote Sensing*, *13*(8), 1434. https://doi.org/10.3390/rs13081434

Rubin, H. J., Fu, J. S., Dentener, F., Li, R., Huang, K., & Fu, H. (2023). Global nitrogen and sulfur deposition mapping using a measurement–model fusion approach. *Atmospheric Chemistry and Physics*, *23*(12), 7091–7102. https://doi.org/10.5194/acp-23-7091-2023

Russo, S., Dosio, A., Graversen, R. G., Sillmann, J., Carrao, H., Dunbar, M. B., et al. (2014). Magnitude of extreme heat waves in present climate and their projection in a warming world. *Journal of Geophysical Research: Atmospheres*, *119*(22), 12,500-12,512. https://doi.org/10.1002/2014JD022098

Sahu, S. K., Gelfand, A. E., & Holland, D. M. (2010). Fusing point and areal level space–time data with application to wet deposition. *Journal of the Royal Statistical Society: Series C (Applied Statistics)*, *59*(1), 77–103. https://doi.org/10.1111/j.1467-9876.2009.00685.x

Sanderman, J., Hengl, T., & Fiske, G. J. (2017). Soil carbon debt of 12,000 years of human land use. *Proceedings of the National Academy of Sciences*, *114*(36), 9575–9580. https://doi.org/10.1073/pnas.1706103114

Scheffers, B. R., De Meester, L., Bridge, T. C. L., Hoffmann, A. A., Pandolfi, J. M., Corlett, R. T., et al. (2016). The broad footprint of climate change from genes to biomes to people. *Science, 354*(6313), aaf7671. https://doi.org/10.1126/science.aaf7671

Schillaci, C., Lombardo, L., Saia, S., Fantappiè, M., Märker, M., & Acutis, M. (2017). Modelling the topsoil carbon stock of agricultural lands with the Stochastic Gradient Treeboost in a semi-arid Mediterranean region. *Geoderma*, *286*, 35–45. https://doi.org/10.1016/j.geoderma.2016.10.019

Schultz, P. A., & Kasting, J. F. (1997). Optimal reductions in CO2 emissions. *Energy Policy*, *25*(5), 491–500. https://doi.org/10.1016/S0301-4215(97)00027-X

Schulzweida, U. (2021). CDO User Guide. https://doi.org/10.5281/zenodo.5614769

Schwede, D., Zhang, L., Vet, R., & Lear, G. (2011). An intercomparison of the deposition models used in the CASTNET and CAPMoN networks. *Atmospheric Environment*, *45*(6), 1337–1346. https://doi.org/10.1016/j.atmosenv.2010.11.050

Schwede, D., Cole, A., Vet, R., & Lear, G. (2019). Ongoing U.S. - Canada Collaboration on Nitrogen and Sulfur Deposition, 5.

Schwede, D. B., & Lear, G. G. (2014). A novel hybrid approach for estimating total deposition in the United States. *Atmospheric Environment, 92*, 207–220. https://doi.org/10.1016/j.atmosenv.2014.04.008

Séférian, R., Nabat, P., Michou, M., Saint-Martin, D., Voldoire, A., Colin, J., et al. (2019). Evaluation of CNRM Earth System Model, CNRM-ESM2-1: Role of Earth System

Processes in Present-Day and Future Climate. *Journal of Advances in Modeling Earth Systems*, *11*(12), 4182–4227. https://doi.org/10.1029/2019MS001791

Seneviratne, S. I., Zhang, X., Adnan, M., Badi, W., Dereczynski, C., Di Luca, A., et al. (2021). Chapter 11: Weather and Climate Extreme Events in a Changing Climate. In J. Chan, A. Sorteberrg, & C. Vera (Eds.), *Climate Change 2021: The Physical Science Basis. Contributions of Working Group I to th Sixth Assessment Report of the Intergovernmental Panel on Climate Change* (pp. 1513–1766). Cambridge, UK and New York, NY, USA: Cambridge University Press.

Shepherd, J. G. (2012). Geoengineering the climate: an overview and update. *Philosophical Transactions of the Royal Society A: Mathematical, Physical and Engineering Sciences*, *370*(1974), 4166–4175. https://doi.org/10.1098/rsta.2012.0186

Simpson, I. R., Tilmes, S., Richter, J. H., Kravitz, B., MacMartin, D. G., Mills, M. J., et al. (2019). The Regional Hydroclimate Response to Stratospheric Sulfate Geoengineering and the Role of Stratospheric Heating. *Journal of Geophysical Research: Atmospheres*, *124*(23), 12587–12616. https://doi.org/10.1029/2019JD031093

Sirois, A. (1990). The effects of missing data on the calculation of precipitation-weighted-mean concentrations in wet deposition. *Atmospheric Environment. Part A. General Topics*, *24*(9), 2277–2288. https://doi.org/10.1016/0960-1686(90)90321-D

Smith, S. J., Andres, R., Conception, E., & Lurz, J. (2004). *Historical Sulfur Dioxide Emissions 1850-2000: Methods and Results* (No. PNNL-14537, 15020102) (p. PNNL-14537, 15020102). https://doi.org/10.2172/15020102

Smith, W., & Henly, C. (2021). Updated and outdated reservations about research into stratospheric aerosol injection. *Climatic Change*, *164*(3), 39. https://doi.org/10.1007/s10584-021-03017-z

Smith, W., & Wagner, G. (2018). Stratospheric aerosol injection tactics and costs in the first 15 years of deployment. *Environmental Research Letters*, *13*(12), 124001. https://doi.org/10.1088/1748-9326/aae98d

Sohl, T., Reker, R., Bouchard, M., Sayler, K., Dornbierer, J., Wika, S., et al. (2016). Modeled historical land use and land cover for the conterminous United States. *Journal of Land Use Science*, *11*(4), 476–499. https://doi.org/10.1080/1747423X.2016.1147619

Sohl, T. L., Sayler, K. L., Bouchard, M. A., Reker, R. R., Friesz, A. M., Bennett, S. L., et al. (2014). Spatially explicit modeling of 1992–2100 land cover and forest stand age for the conterminous United States. *Ecological Applications*, *24*(5), 1015–1036. https://doi.org/10.1890/13-1245.1

Sothe, C., Gonsamo, A., Arabian, J., & Snider, J. (2022). Large scale mapping of soil organic carbon concentration with 3D machine learning and satellite observations. *Geoderma*, *405*, 115402. https://doi.org/10.1016/j.geoderma.2021.115402

Staddon, P. L., Montgomery, H. E., & Depledge, M. H. (2014). Climate warming will not decrease winter mortality. *Nature Climate Change*, *4*(3), 190–194. https://doi.org/10.1038/nclimate2121

Stewart, A. J., Halabisky, M., Babcock, C., Butman, D. E., D'Amore, D. V., & Moskal, L. M. (2024). Revealing the hidden carbon in forested wetland soils. *Nature Communications*, *15*(1), 726. https://doi.org/10.1038/s41467-024-44888-x

Sun, K., Gao, Y., Guo, X., Zhang, J., Zeng, X., Ma, M., et al. (2022). The enhanced role of atmospheric reduced nitrogen deposition in future over East Asia–Northwest Pacific. *Science of The Total Environment*, *833*, 155146. https://doi.org/10.1016/j.scitotenv.2022.155146

Sundquist, E. T., Ackerman, K. V., Bliss, N. B., Kellndorfer, J. M., Reeves, M. C., & Rollins, M. G. (2009). *Rapid Assessment of U.S. Forest and Soil Organic Carbon Storage and Forest Biomass Carbon Sequestration Capacity* (Open-File Report No. 1283) (p. 23). US Geological Survey, US Department of the Interior.

Tadiello, T., Perego, A., Valkama, E., Schillaci, C., & Acutis, M. (2022). Computation of total soil organic carbon stock and its standard deviation from layered soils. *MethodsX*, *9*, 101662. https://doi.org/10.1016/j.mex.2022.101662

Tan, J., Fu, J. S., Dentener, F., Sun, J., Emmons, L., Tilmes, S., et al. (2018). Multi-model study of HTAP II on sulfur and nitrogen deposition. *Atmospheric Chemistry and Physics, 18*(9), 6847–6866. https://doi.org/10.5194/acp-18-6847-2018

Tan, Z., Liu, S., Sohl, T. L., Wu, Y., & Young, C. J. (2015). Ecosystem carbon stocks and sequestration potential of federal lands across the conterminous United States. *Proceedings of the National Academy of Sciences*, *112*(41), 12723–12728. https://doi.org/10.1073/pnas.1512542112

Tao, F., Zhou, Z., Huang, Y., Li, Q., Lu, X., Ma, S., et al. (2020). Deep Learning Optimizes Data-Driven Representation of Soil Organic Carbon in Earth System Model Over the Conterminous United States. *Frontiers in Big Data*, *3*. Retrieved from https://www.frontiersin.org/article/10.3389/fdata.2020.00017

Teng, H., Branstator, G., Wang, H., Meehl, G. A., & Washington, W. M. (2013). Probability of US heat waves affected by a subseasonal planetary wave pattern. *Nature Geoscience*, *6*(12), 1056–1061. https://doi.org/10.1038/ngeo1988

Thornton, M. M., Shrestha, R., Wei, Y., Thornton, P. E., Kao, S., & Wilson, B. E. (2020). Daymet: Daily Surface Weather Data on a 1-km Grid for North America, Version 4. ORNL Distributed Active Archive Center. https://doi.org/10.3334/ORNLDAAC/1840

Thornton, P. E., Shrestha, R., Thornton, M., Kao, S.-C., Wei, Y., & Wilson, B. E. (2021). Gridded daily weather data for North America with comprehensive uncertainty quantification. *Scientific Data*, *8*(1), 190. https://doi.org/10.1038/s41597-021-00973-0

Tian, Z., Liu, F., Liang, Y., & Zhu, X. (2022). Mapping soil erodibility in southeast China at 250 m resolution: Using environmental variables and random forest regression with limited samples. *International Soil and Water Conservation Research*, *10*(1), 62–74. https://doi.org/10.1016/j.iswcr.2021.06.005

Tifafi, M., Guenet, B., & Hatte, C. (2018). Large Differences in Global and Regional Total Soil Carbon Stock Estimates Based on SoilGrids, HWSD, and NCSCD: Intercomparison and Evaluation Based on Field Data From USA, England, Wales, and France. *Global Biogeochemical Cycles*, *32*, 42–56. https://doi.org/doi/10.1002/2017GB005678

Tilmes, S., Mills, M. J., Niemeier, U., Schmidt, H., Robock, A., Kravitz, B., et al. (2015). A new Geoengineering Model Intercomparison Project (GeoMIP) experiment designed for climate and chemistry models. *Geoscientific Model Development*, *8*(1), 43–49. https://doi.org/10.5194/gmd-8-43-2015

Tilmes, Simone, MacMartin, D. G., Lenaerts, J. T. M., van Kampenhout, L., Muntjewerf, L., Xia, L., et al. (2020). Reaching 1.5 and 2.0 °C global surface temperature targets using stratospheric aerosol geoengineering. *Earth System Dynamics*, *11*(3), 579–601. https://doi.org/10.5194/esd-11-579-2020

Tilmes, Simone, Visioni, D., Jones, A., Haywood, J., Séférian, R., Nabat, P., et al. (2022). Stratospheric ozone response to sulfate aerosol and solar dimming climate interventions based on the G6 Geoengineering Model Intercomparison Project (GeoMIP) simulations. *Atmospheric Chemistry and Physics*, *22*(7), 4557–4579. https://doi.org/10.5194/acp-22-4557-2022

Timmermans, B., Wehner, M., Cooley, D., O'Brien, T., & Krishnan, H. (2019). An evaluation of the consistency of extremes in gridded precipitation data sets. *Climate Dynamics*, *52*(11), 6651–6670. https://doi.org/10.1007/s00382-018-4537-0

Tjiputra, J. F., Grini, A., & Lee, H. (2016). Impact of idealized future stratospheric aerosol injection on the large-scale ocean and land carbon cycles. *Journal of Geophysical Research: Biogeosciences*, *121*(1), 2–27. https://doi.org/10.1002/2015JG003045

Tollefson. (2019). The hard truths of climate change — by the numbers. *Nature*, *573*(7774), 324+.

Tørseth, K., Aas, W., Breivik, K., Fjæraa, A. M., Fiebig, M., Hjellbrekke, A. G., et al. (2012). Introduction to the European Monitoring and Evaluation Programme (EMEP) and observed atmospheric composition change during 1972 - 2009. *Atmospheric Chemistry and Physics*, *12*(12), 5447–5481. https://doi.org/10.5194/acp-12-5447-2012

Townshend, J. R. G. (1992). Improved global data for land applications. A proposal for a new high resolution data set. Report of the Land Cover Working Group of IGBP-DIS. *Global Change Report (Sweden)*. Retrieved from https://scholar.google.com/scholar_lookup?title=Improved+global+data+for+land+applications.+A+proposal+for+a+new+high+resolution+data+set.+Report+of+the+Land+Cover+Working+Group+of+IGBP-DIS&author=Townshend%2C+J.R.G.+%28ed.%29&publication_year=1992

Tracy, S. M., Moch, J. M., Eastham, S. D., & Buonocore, J. J. (2022). Stratospheric aerosol injection may impact global systems and human health outcomes. *Elementa: Science of the Anthropocene*, *10*(1), 00047. https://doi.org/10.1525/elementa.2022.00047

Tye, M. R., Dagon, K., Molina, M. J., Richter, J. H., Visioni, D., Kravitz, B., & Tilmes, S. (2022). Indices of extremes: geographic patterns of change in extremes and associated vegetation impacts under climate intervention. *Earth System Dynamics*, *13*(3), 1233–1257. https://doi.org/10.5194/esd-13-1233-2022

Uhran, B., Windham-Myers, L., Bliss, N., Nahlik, A. M., Sundquist, E. T., & Stagg, C. L. (2021). Improved Wetland Soil Organic Carbon Stocks of the Conterminous U.S.

Through Data Harmonization. *Frontiers in Soil Science*, *1*. https://doi.org/10.3389/fsoil.2021.706701

Uludere Aragon, N. Z., Parker, N. C., VanLoocke, A., Bagley, J., Wang, M., & Georgescu, M. (2023). Sustainable land use and viability of biojet fuels. *Nature Sustainability*, *6*(2), 158–168. https://doi.org/10.1038/s41893-022-00990-w

US EPA. (2015a, June 18). Clean Air Status and Trends Network (CASTNET) [Collections and Lists]. Retrieved November 18, 2021, from https://www.epa.gov/castnet

US EPA, O. (2015b, June 2). National Emissions Inventory (NEI) [Other Policies and Guidance]. Retrieved February 18, 2021, from https://www.epa.gov/air-emissions-inventories/national-emissions-inventory-nei

US EPA, O. (2015c, November 6). Climate Change Indicators in the United States [Reports and Assessments]. Retrieved August 1, 2023, from https://www.epa.gov/climate-indicators

US EPA, O. (2016, July 1). Climate Change Indicators: Heat-Related Deaths [Reports and Assessments]. Retrieved March 10, 2022, from https://www.epa.gov/climate-indicators/climate-change-indicators-heat-related-deaths

Vaudour, E., Gomez, C., Fouad, Y., & Lagacherie, P. (2019). Sentinel-2 image capacities to predict common topsoil properties of temperate and Mediterranean agroecosystems. *Remote Sensing of Environment*, *223*, 21–33. https://doi.org/10.1016/j.rse.2019.01.006

Védère, C., Lebrun, M., Honvault, N., Aubertin, M.-L., Girardin, C., Garnier, P., et al. (2022). How does soil water status influence the fate of soil organic matter? A review of processes across scales. *Earth-Science Reviews*, *234*, 104214. https://doi.org/10.1016/j.earscirev.2022.104214

Venter, Z. S., Hawkins, H.-J., Cramer, M. D., & Mills, A. J. (2021). Mapping soil organic carbon stocks and trends with satellite-driven high resolution maps over South Africa. *Science of The Total Environment*, *771*, 145384. https://doi.org/10.1016/j.scitotenv.2021.145384

Vet, R., Artz, R. S., Carou, S., Shaw, M., Ro, C.-U., Aas, W., et al. (2014). A global assessment of precipitation chemistry and deposition of sulfur, nitrogen, sea salt, base cations, organic acids, acidity and pH, and phosphorus. *Atmospheric Environment*, *93*, 3–100. https://doi.org/10.1016/j.atmosenv.2013.10.060

Viscarra Rossel, R. A., Lee, J., Behrens, T., Luo, Z., Baldock, J., & Richards, A. (2019). Continental-scale soil carbon composition and vulnerability modulated by regional environmental controls. *Nature Geoscience*, *12*(7), 547–552. https://doi.org/10.1038/s41561-019-0373-z

Vishwakarma, S., Zhang, X., Dobermann, A., Heffer, P., & Zhou, F. (2023). Global nitrogen deposition inputs to cropland at national scale from 1961 to 2020. *Scientific Data*, *10*(1), 488. https://doi.org/10.1038/s41597-023-02385-8

Visioni, D., Pitari, G., Tuccella, P., & Curci, G. (2017). *Quantification of sulfur deposition changes under sulfate geoengineering conditions* (preprint). Aerosols/Atmospheric Modelling/Stratosphere/Physics (physical properties and processes). https://doi.org/10.5194/acp-2017-987

Visioni, D., Pitari, G., Tuccella, P., & Curci, G. (2018). Sulfur deposition changes under sulfate geoengineering conditions: quasi-biennial oscillation effects on the transport and lifetime of stratospheric aerosols. *Atmospheric Chemistry and Physics*, *18*(4), 2787–2808. https://doi.org/10.5194/acp-18-2787-2018

Visioni, D., Slessarev, E., MacMartin, D. G., Mahowald, N. M., Goodale, C. L., & Xia, L. (2020). What goes up must come down: impacts of deposition in a sulfate geoengineering scenario. *Environmental Research Letters*, *15*(9), 094063. https://doi.org/10.1088/1748-9326/ab94eb

Visioni, D., MacMartin, D. G., Kravitz, B., Boucher, O., Jones, A., Lurton, T., et al. (2021). Identifying the sources of uncertainty in climate model simulations of solar radiation modification with the G6sulfur and G6solar Geoengineering Model Intercomparison Project (GeoMIP) simulations. *Atmospheric Chemistry and Physics*, *21*(13), 10039–10063. https://doi.org/10.5194/acp-21-10039-2021

Visioni, D., Bednarz, E. M., Lee, W. R., Kravitz, B., Jones, A., Haywood, J. M., & MacMartin, D. G. (2023). Climate response to off-equatorial stratospheric sulfur injections in three Earth system models – Part 1: Experimental protocols and surface changes. *Atmospheric Chemistry and Physics*, *23*(1), 663–685. https://doi.org/10.5194/acp-23-663-2023

Vitousek, P. M. (1992). Global Environmental Change: An Introduction. *Annual Review of Ecology and Systematics*, *23*(1), 1–14. https://doi.org/10.1146/annurev.es.23.110192.000245

Vose, R. S., Applequist, S., Squires, M., Durre, I., Menne, M. J., Williams, C. N., et al. (2014). Improved Historical Temperature and Precipitation Time Series for U.S. Climate

Divisions. *Journal of Applied Meteorology and Climatology*, *53*(5), 1232–1251. https://doi.org/10.1175/JAMC-D-13-0248.1

de Vries, W., Solberg, S., Dobbertin, M., Sterba, H., Laubhann, D., van Oijen, M., et al. (2009). The impact of nitrogen deposition on carbon sequestration by European forests and heathlands. *Forest Ecology and Management*, *258*(8), 1814–1823. https://doi.org/10.1016/j.foreco.2009.02.034

Walker, J. T., Beachley, G., Amos, H. M., Baron, J. S., Bash, J., Baumgardner, R., et al. (2019). Toward the improvement of total nitrogen deposition budgets in the United States. *Science of The Total Environment*, *691*, 1328–1352. https://doi.org/10.1016/j.scitotenv.2019.07.058

Walton, D., Berg, N., Pierce, D., Maurer, E., Hall, A., Lin, Y.-H., et al. (2020). Understanding Differences in California Climate Projections Produced by Dynamical and Statistical Downscaling. *Journal of Geophysical Research: Atmospheres*, *125*(19), e2020JD032812. https://doi.org/10.1029/2020JD032812

Wang, M., Guo, X., Zhang, S., Xiao, L., Mishra, U., Yang, Y., et al. (2022). Global soil profiles indicate depth-dependent soil carbon losses under a warmer climate. *Nature Communications*, *13*(1), 5514. https://doi.org/10.1038/s41467-022-33278-w

Wang, M., Zhang, S., Guo, X., Xiao, L., Yang, Y., Luo, Y., et al. (2024). Responses of soil organic carbon to climate extremes under warming across global biomes. *Nature Climate Change*, *14*(1), 98–105. https://doi.org/10.1038/s41558-023-01874-3

Wang, Z., Kumar, J., Weintraub-Leff, S. R., Todd-Brown, K., Mishra, U., & Sihi, D. (2024). Upscaling Soil Organic Carbon Measurements at the Continental Scale Using Multivariate Clustering Analysis and Machine Learning. *Journal of Geophysical Research: Biogeosciences*, *129*(2), e2023JG007702. https://doi.org/10.1029/2023JG007702

Watanabe, S., Kotsuki, S., Kanae, S., Tanaka, K., & Higuchi, A. (2020). Snow water scarcity induced by record-breaking warm winter in 2020 in Japan. *Scientific Reports*, *10*(1), 18541. https://doi.org/10.1038/s41598-020-75440-8

Wei, J., Huang, W., Li, Z., Xue, W., Peng, Y., Sun, L., & Cribb, M. (2019). Estimating 1-km-resolution PM2.5 concentrations across China using the space-time random forest approach. *Remote Sensing of Environment*, *231*(1112221). https://doi.org/DOI:10.1016/j.rse.2019.111221

Wen, Z., Xu, W., Li, Q., Han, M., Tang, A., Zhang, Y., et al. (2020). Changes of nitrogen deposition in China from 1980 to 2018. *Environment International*, *144*, 106022. https://doi.org/10.1016/j.envint.2020.106022

Werner, A. T., & Cannon, A. J. (2016). Hydrologic extremes – an intercomparison of multiple gridded statistical downscaling methods. *Hydrology and Earth System Sciences*, *20*(4), 1483–1508. https://doi.org/10.5194/hess-20-1483-2016

Whitburn, S., Van Damme, M., Clarisse, L., Bauduin, S., Heald, C. L., Hadji-Lazaro, J., et al. (2016). A flexible and robust neural network IASI-NH3 retrieval algorithm. *Journal of Geophysical Research: Atmospheres*, *121*(11), 6581–6599. https://doi.org/10.1002/2016JD024828

Wieder, W. R., Pierson, D., Earl, S., Lajtha, K., Baer, S. G., Ballantyne, F., et al. (2021). SoDaH: the SOils DAta Harmonization database, an open-source synthesis of soil data from research networks, version 1.0. *Earth System Science Data*, *13*(5), 1843–1854. https://doi.org/10.5194/essd-13-1843-2021

Wootten, A. M., Dixon, K. W., Adams-Smith, D. J., & McPherson, R. A. (2024). False springs and spring phenology: Propagating effects of downscaling technique and training data. *International Journal of Climatology*, *44*(6), 2021–2040. https://doi.org/10.1002/joc.8438

World Health Organization. (2022). Heatwaves [Overviews and Factsheets]. Retrieved March 10, 2022, from https://www.who.int/westernpacific/health-topics/heatwaves

World Meteorological Organization. (2021). *Measurement-Model Fusion for Global Total Atmospheric Deposition Initiative: Implementation Plan for 2021-2026* (GAW Report No. 269) (pp. 1–52). Geneva, Switzerland: World Meteorological Organization. Retrieved from https://library.wmo.int/doc_num.php?explnum_id=10831

Wu, D., Zhao, X., Liang, S., Zhou, T., Huang, K., Tang, B., & Zhao, W. (2015). Time-lag effects of global vegetation responses to climate change. *Global Change Biology*, *21*(9), 3520–3531. https://doi.org/10.1111/gcb.12945

Wu, J., Zhou, Y., Gao, Y., Fu, J. S., Johnson, B. A., Huang, C., et al. (2014). Estimation and Uncertainty Analysis of Impacts of Future Heat Waves on Mortality in the Eastern

United States. *Environmental Health Perspectives*, *122*(1), 10–16. https://doi.org/10.1289/ehp.1306670

Wyden, R. The North American Grasslands Conservation Act, Pub. L. No. S. 4639 (2022). Retrieved from https://actforgrasslands.org/bill-introduction/

Xiong, X., Grunwald, S., Myers, D. B., Ross, C. W., Harris, W. G., & Comerford, N. B. (2014). Interaction effects of climate and land use/land cover change on soil organic carbon sequestration. *Science of The Total Environment*, *493*, 974–982. https://doi.org/10.1016/j.scitotenv.2014.06.088

Xu, W., Luo, X. S., Pan, Y. P., Zhang, L., Tang, A. H., Shen, J. L., et al. (2015). Quantifying atmospheric nitrogen deposition through a nationwide monitoring network across China. *Atmospheric Chemistry and Physics*, *15*(21), 12345–12360. https://doi.org/10.5194/acp-15-12345-2015

Xu, Wen, Zhang, L., & Liu, X. (2019). A database of atmospheric nitrogen concentration and deposition from the nationwide monitoring network in China. *Scientific Data*, *6*(1), 51. https://doi.org/10.1038/s41597-019-0061-2

Xu, Y., Lin, L., Tilmes, S., Dagon, K., Xia, L., Diao, C., et al. (2020). Climate engineering to mitigate the projected 21st-century terrestrial drying of the Americas: a direct comparison of carbon capture and sulfur injection. *Earth System Dynamics*, *11*(3), 673–695. https://doi.org/10.5194/esd-11-673-2020

Yan, H.-H., Li, X.-J., Zhang, X.-Y., Wang, W.-H., Chen, L.-F., Zhang, M.-G., & Xu, J. (2016). Comparative Analysis and Verification of Remote Sensing Retrieval Algorithms for Total Atmospheric SO2 Column. *Acta Physica Sinica*, *65*(8). https://doi.org/10.7498/aps.65.084204

Yang, C., Feng, M., Song, L., Wang, C., Yang, W., Xie, Y., et al. (2021). Study on hyperspectral estimation model of soil organic carbon content in the wheat field under different water treatments. *Scientific Reports*, *11*(1), 18582. https://doi.org/10.1038/s41598-021-98143-0

Yang, C.-E., Hoffman, F. M., Ricciuto, D. M., Tilmes, S., Xia, L., MacMartin, D. G., et al. (2020). Assessing terrestrial biogeochemical feedbacks in a strategically geoengineered climate. *Environmental Research Letters*, *15*(10), 104043. https://doi.org/10.1088/1748-9326/abacf7

Yang, L., He, X., Shen, F., Zhou, C., Zhu, A.-X., Gao, B., et al. (2020). Improving prediction of soil organic carbon content in croplands using phenological parameters extracted from NDVI time series data. *Soil and Tillage Research*, *196*, 104465. https://doi.org/10.1016/j.still.2019.104465

Yang, Z., Dominguez, F., & Zeng, X. (2019). Large and local-scale features associated with heat waves in the United States in reanalysis products and the NARCCAP model ensemble. *Climate Dynamics*, *52*(3), 1883–1901. https://doi.org/10.1007/s00382-018-4414-x

Yu, W., Weintraub, S. R., & Hall, S. J. (2021). Climatic and Geochemical Controls on Soil Carbon at the Continental Scale: Interactions and Thresholds - Yu - 2021 - Global Biogeochemical Cycles - Wiley Online Library. *Global Biogeochemical Cycles*, *35*(3). https://doi.org/DOI:10.1029/2020GB006781

Zhang, L., Jacob, D. J., Knipping, E. M., Kumar, N., Munger, J. W., Carouge, C. C., et al. (2012). Nitrogen deposition to the United States: distribution, sources, and processes. *Atmospheric Chemistry and Physics*, *12*(10), 4539–4554. https://doi.org/10.5194/acp-12-4539-2012

Zhang, Lei, Xu, Y., Meng, C., Li, X., Liu, H., & Wang, C. (2020). Comparison of Statistical and Dynamic Downscaling Techniques in Generating High-Resolution Temperatures in China from CMIP5 GCMs. *Journal of Applied Meteorology and Climatology*, *59*(2), 207–235. https://doi.org/10.1175/JAMC-D-19-0048.1

Zhang, M., Leon, C. de, & Migliaccio, K. (2018). Evaluation and comparison of interpolated gauge rainfall data and gridded rainfall data in Florida, USA. *Hydrological Sciences Journal*, *63*(4), 561–582. https://doi.org/10.1080/02626667.2018.1444767

Zhang, X. Y., Chuai, X. W., Liu, L., Zhang, W. T., Lu, X. H., Zhao, L. M., & Chen, D. M. (2018). Decadal Trends in Wet Sulfur Deposition in China Estimated From OMI SO2 Columns. *Journal of Geophysical Research: Atmospheres*, *123*(18), 10,796-10,811. https://doi.org/10.1029/2018JD028770

Zhang, Y., Mathur, R., Bash, J. O., Hogrefe, C., Xing, J., & Roselle, S. J. (2018). Long-term trends in total inorganic nitrogen and sulfur deposition in the US from 1990 to 2010. *Atmospheric Chemistry and Physics*, *18*(12), 9091–9106. https://doi.org/10.5194/acp-18-9091-2018

Zhang, Y., Foley, K. M., Schwede, D. B., Bash, J. O., Pinto, J. P., & Dennis, R. L. (2019). A Measurement-Model Fusion Approach for Improved Wet Deposition Maps and Trends. *Journal of Geophysical Research: Atmospheres*, *124*(7), 4237–4251. https://doi.org/10.1029/2018JD029051

Zhao, Y., Zhang, L., Chen, Y., Liu, X., Xu, W., Pan, Y., & Duan, L. (2017). Atmospheric nitrogen deposition to China: A model analysis on nitrogen budget and critical load exceedance. *Atmospheric Environment*, *153*, 32–40. https://doi.org/10.1016/j.atmosenv.2017.01.018

Zhou, K., Zhao, Y., Zhang, L., & Xi, M. (2021). Declining dry deposition of NO2 and SO2 with diverse spatiotemporal patterns in China from 2013 to 2018. *Atmospheric Environment*, *262*, 118655. https://doi.org/10.1016/j.atmosenv.2021.118655

Zhou, X., Zhou, L., Nie, Y., Fu, Y., Du, Z., Shao, J., et al. (2016). Similar responses of soil carbon storage to drought and irrigation in terrestrial ecosystems but with contrasting mechanisms: A meta-analysis. *Agriculture, Ecosystems & Environment*, *228*, 70–81. https://doi.org/10.1016/j.agee.2016.04.030

Zhou, Y., Hartemink, A. E., Shi, Z., Liang, Z., & Lu, Y. (2019). Land use and climate change effects on soil organic carbon in North and Northeast China. *Science of The Total Environment*, *647*, 1230–1238. https://doi.org/10.1016/j.scitotenv.2018.08.016

Zhu, J., Chen, Z., Wang, Q., Xu, L., He, N., Jia, Y., et al. (2020). Potential transition in the effects of atmospheric nitrogen deposition in China. *Environmental Pollution*, *258*, 113739. https://doi.org/10.1016/j.envpol.2019.113739

Zomer, R. J., Bossio, D. A., Sommer, R., & Verchot, L. V. (2017). Global Sequestration Potential of Increased Organic Carbon in Cropland Soils. *Scientific Reports*, *7*(1), 15554. https://doi.org/10.1038/s41598-017-15794-8

Zuo, J., Pullen, S., Palmer, J., Bennetts, H., Chileshe, N., & Ma, T. (2015). Impacts of heat waves and corresponding measures: a review. *Journal of Cleaner Production*, *92*, 1–12. https://doi.org/10.1016/j.jclepro.2014.12.078

Appendix

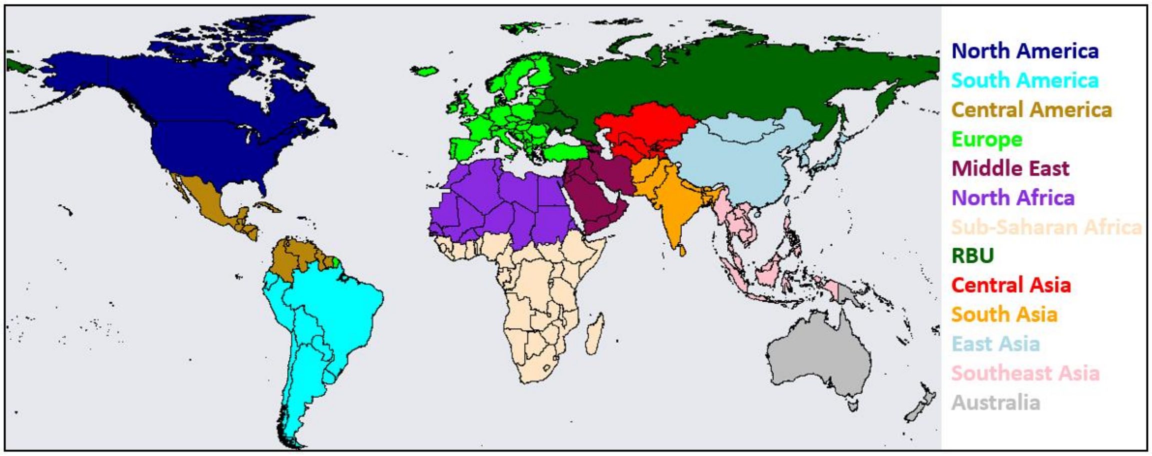

Figure S2.1. A world map showing the regions used to calculate the totals presented in Table 2.1. This figure is adapted from Tan et al., 2018, based on their region divisions. RBU is Russia, Belarus, Ukraine.

Table S2.1. 2010 adjusted global wet and dry deposition in Tg N or Tg S. MMM indicates Tan et al.'s 2018 multi-model mean and MMF is this measurement-model fusion work with a 1^{o} interpolation distance. Total N deposition is 112.02 Tg N and total S deposition is 88.60 Tg S. Coastal means deposition on sea within 1 degree of the coastline. RBU is an abbreviation for Russia, Belarus, and Ukraine. Open ocean does not include near-land "coastal" waters. The regions can be seen in the world map in Figure S2.1. Regional changes greater than or equal to 10% are bolded and italicized.

	Non-Coastal		Coastal		Non-Coastal		Coastal		Non-Coastal		Coastal	
	MMM	MMF	MMM	MMF	MMM	MMF	MMM	MMF	MMM	MMF	MMM	MMF
Region	**Total NH_x**				**Total NO_y**				**Total SO_x**			
North America	3.40	3.50	0.40	***0.30***	4.40	4.44	0.80	0.90	4.70	***5.66***	1.30	***1.68***
Europe	2.50	2.67	0.80	***1.14***	2.60	2.42	1.20	***1.75***	2.70	2.51	1.50	***3.18***
South Asia	8.60	8.60	1.00	1.00	3.60	3.60	0.70	0.70	3.70	3.70	1.00	1.00
East Asia	6.70	6.71	1.00	1.04	8.30	7.90	2.20	***2.44***	11.20	11.89	2.90	***4.09***
Southeast Asia	3.20	***2.25***	1.60	***2.12***	1.90	***1.10***	1.40	1.44	2.40	***0.81***	2.80	***0.56***
Australia	0.40	0.40	0.40	0.40	0.60	0.60	0.40	0.40	1.00	1.00	1.50	1.50
North Africa	0.70	0.70	0.20	0.20	1.40	1.40	0.40	0.40	1.00	1.00	0.50	0.50
Sub-Saharan Africa	3.40	3.40	0.40	0.40	4.70	4.70	0.60	0.60	2.70	2.70	0.70	0.70
Middle East	0.50	***0.38***	0.10	0.10	1.40	1.40	0.30	0.30	1.70	***3.18***	0.60	0.60
Central America	1.40	1.40	0.60	0.60	1.20	1.20	0.80	0.80	1.40	1.40	1.40	1.40
South America	3.80	3.80	0.30	0.30	3.40	3.40	0.30	0.30	2.40	2.40	0.60	0.60
RBU	1.80	1.66	0.30	***0.08***	2.40	***2.12***	0.50	0.46	3.60	***5.10***	0.90	***1.17***
Central Asia	0.50	0.50	0.00	0.00	0.60	0.60	0.00	0.00	1.20	***1.87***	0.10	0.10
Antarctica	0.10	0.10	0.00	0.00	0.10	0.10	0.00	0.00	1.40	1.40	0.00	0.00
Continental	37.00	36.07	7.10	7.68	36.70	34.98	9.70	10.49	41.00	44.62	15.60	17.08
Open Oceans	9.90	9.90			12.90	12.90			26.90	26.90		
Global	46.90	45.97	7.10	7.68	49.60	47.88	9.70	10.49	67.90	71.52	15.60	17.08

Table S2.2. 2010 adjusted global wet and dry deposition in Tg N or Tg S.MMM indicates Tan et al.'s 2018 multi-model mean and MMF is this measurement-model fusion work with a 5º interpolation distance. Total N deposition is 120.36 Tg N and total S deposition is 89.93 Tg S. Coastal means deposition on sea within 1 degree of the coastline. RBU is an abbreviation for Russia, Belarus, and Ukraine. Open ocean does not include near-land "coastal" waters. The regions can be seen in the world map in Figure S2.1. Regional changes greater than or equal to 10% are bolded and italicized.

	Non-Coastal		Coastal		Non-Coastal		Coastal		Non-Coastal		Coastal	
	MMM	MMF	MMM	MMF	MMM	MMF	MMM	MMF	MMM	MMF	MMM	MMF
Region	**Total NH_x**				**Total NO_y**				**Total SO_x**			
North America	3.40	3.66	0.40	***0.30***	4.40	4.54	0.80	***0.90***	4.70	***5.67***	1.30	***1.69***
Europe	2.50	2.68	0.80	***1.14***	2.60	2.42	1.20	***1.75***	2.70	2.51	1.50	***3.18***
South Asia	8.60	8.60	1.00	1.00	3.60	3.60	0.70	0.70	3.70	3.70	1.00	1.00
East Asia	6.70	***5.96***	1.00	1.04	8.30	***6.80***	2.20	***2.44***	11.20	11.89	2.90	***4.10***
Southeast Asia	3.20	***1.25***	1.60	***2.12***	1.90	***0.60***	1.40	1.44	2.40	***0.81***	2.80	***0.57***
Australia	0.40	0.40	0.40	0.40	0.60	0.60	0.40	0.40	1.00	1.00	1.50	1.50
North Africa	0.70	0.70	0.20	0.20	1.40	1.40	0.40	0.40	1.00	1.00	0.50	0.50
Sub-Saharan Africa	3.40	3.40	0.40	0.40	4.70	4.70	0.60	0.60	2.70	2.70	0.70	0.70
Middle East	0.50	***0.38***	0.10	0.10	1.40	***1.11***	0.30	0.30	1.70	***3.18***	0.60	0.60
Central America	1.40	1.40	0.60	0.60	1.20	1.20	0.80	0.80	1.40	1.40	1.40	1.40
South America	3.80	3.80	0.30	0.30	3.40	3.40	0.30	0.30	2.40	2.40	0.60	0.60
RBU	1.80	***1.08***	0.30	***0.77***	2.40	***1.36***	0.50	0.50	3.60	***5.10***	0.90	***1.17***
Central Asia	0.50	***0.32***	0.00	0.00	0.60	0.60	0.00	0.00	1.20	***1.86***	0.10	0.10
Antarctica	0.10	0.10	0.00	0.00	0.10	0.10	0.00	0.00	1.40	1.40	0.00	0.00
Continental	37.00	33.73	7.10	***8.37***	36.70	***32.43***	9.70	10.53	41.00	44.62	15.60	***17.11***
Open Oceans	9.90	***16.00***			12.90	***19.30***			26.90	28.20		
Global	46.90	49.73	7.10	***8.37***	49.60	51.73	9.70	10.53	67.90	72.82	15.60	***17.11***

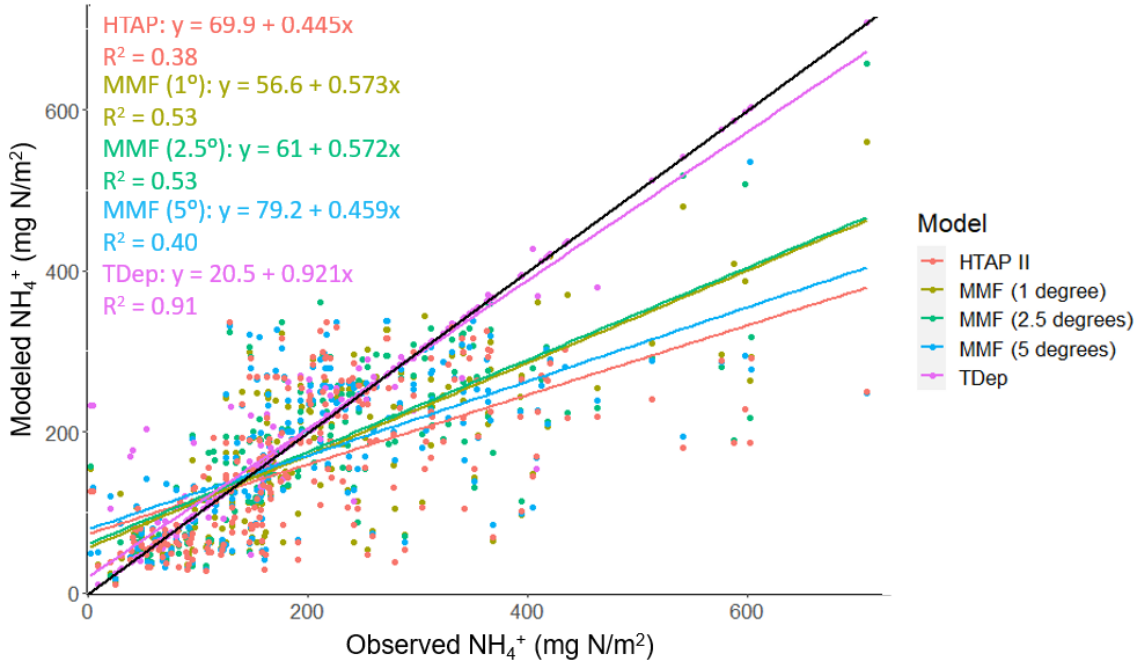

Figure S2.2. Observed and modeled wet NH_4^+ deposition in the US in 2010.Each NADP/NTN wet deposition measurement and the associated HTAP II, TDep, or MMF NH_4 wet deposition value. The black line is the 1:1 line.

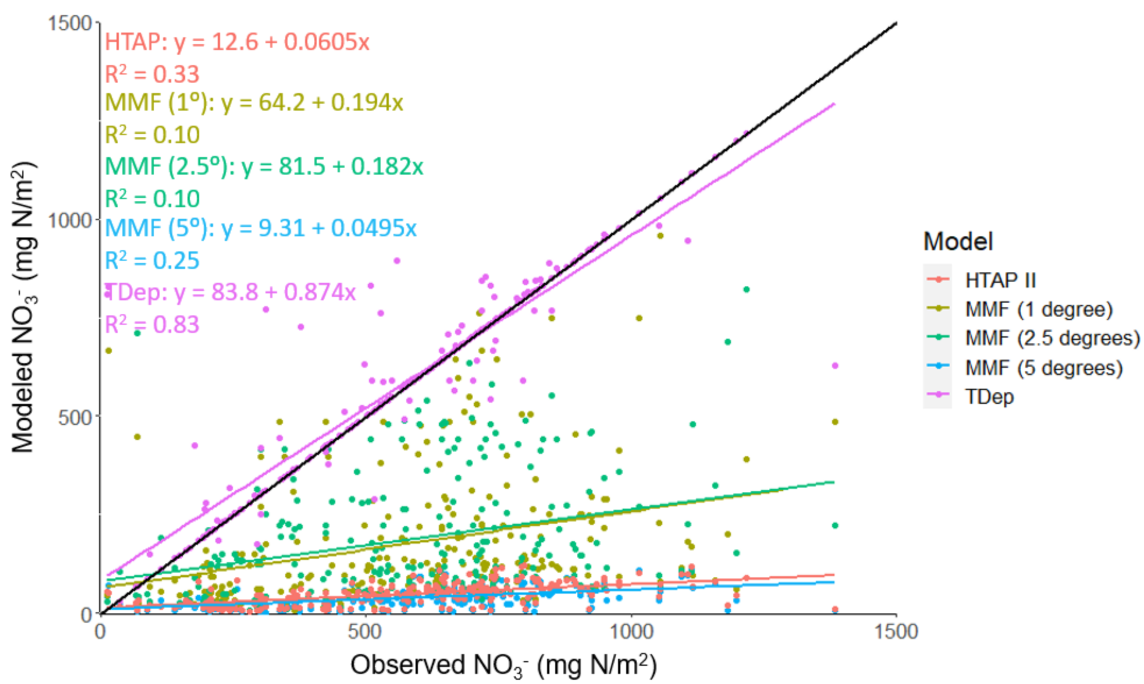

Figure S2.3. Observed and modeled wet NO_3^- deposition in the US in 2010.Each NADP/NTN wet deposition measurement and the associated HTAP II, TDep, or MMF NO_3 wet deposition value. The black line is the 1:1 line.

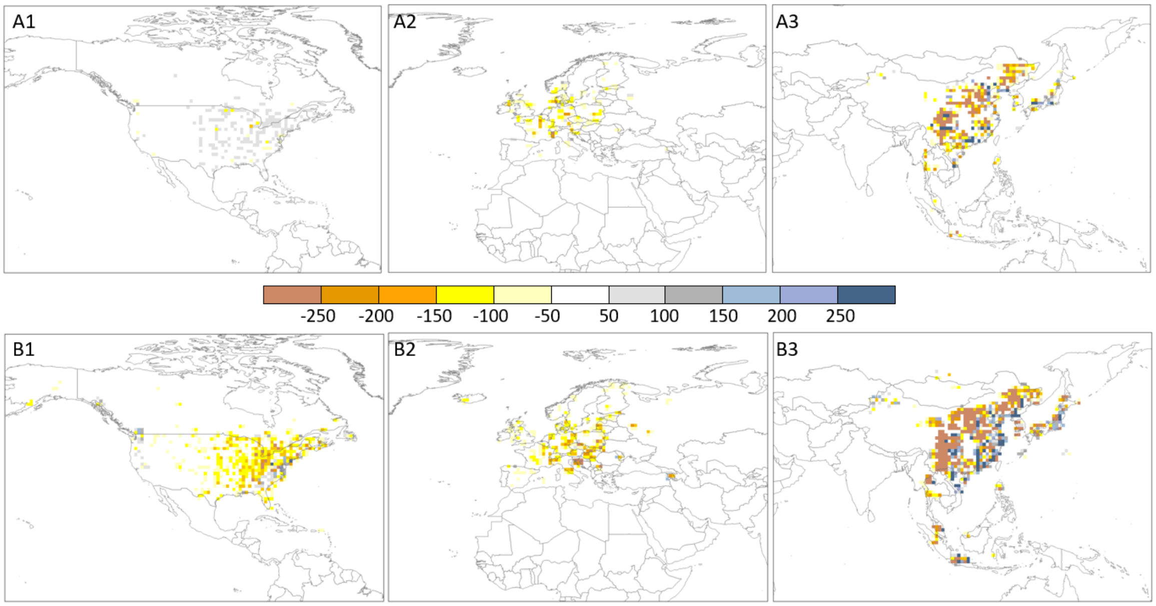

Figure S2.4. The difference between MMF and MMM deposition with a 1-degree interpolation distance. A) MMF minus MMM reactive nitrogen deposition in North America (A1) Europe (A2) and East Asia (A3) in mg/m^2. B) MMF minus MMM sulfate deposition in North America (B1) Europe (B2) and East Asia (B3) in mg/m^2.

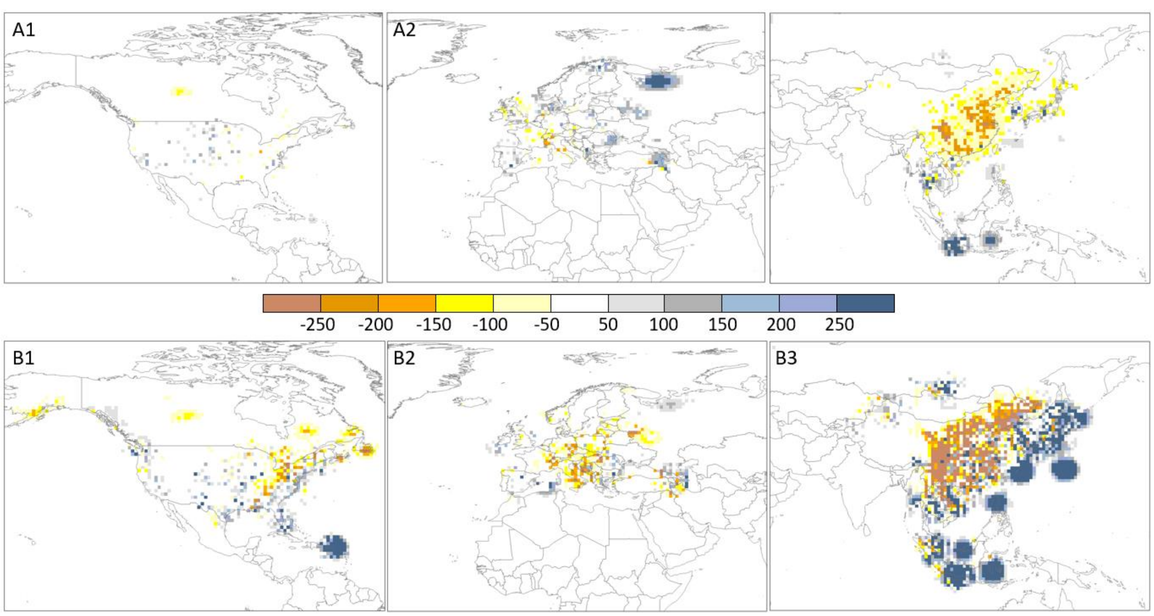

Figure S2.5. The difference between MMF and MMM deposition with a 5-degree interpolation distance. A) MMF minus MMM reactive nitrogen deposition in North America (A1) Europe (A2) and East Asia (A3) in mg/m^2. B) MMF minus MMM sulfate deposition in North America (B1) Europe (B2) and East Asia (B3) in mg/m^2.

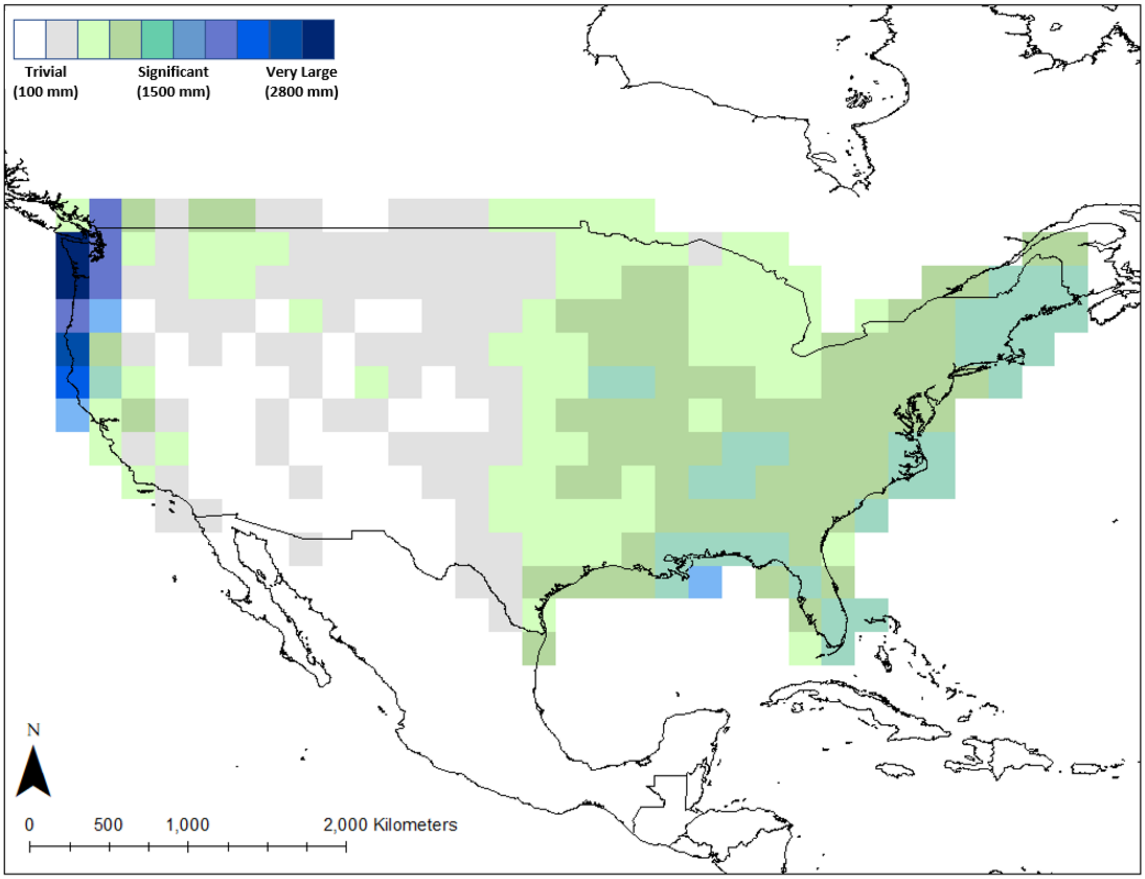

Figure S2.6. The difference between aggregated PRISM precipitation (1.9x1.9 degree) and modeled CAM-chem precipitation (1.9x1.9 degree) over the US in 2010. The greatest differences are in coastal areas.

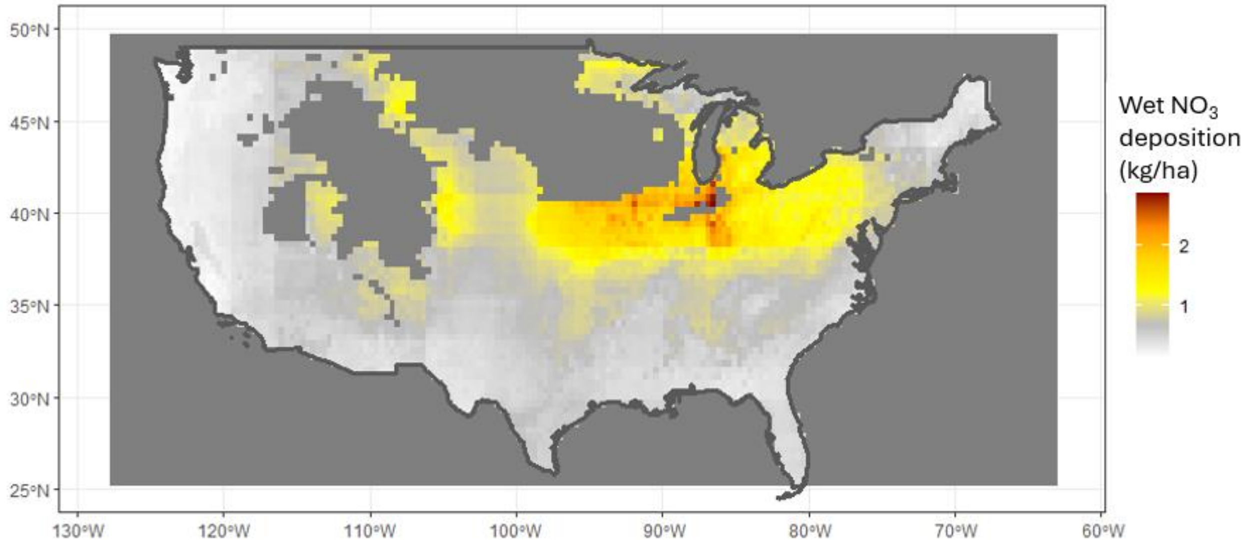

Figure S3.1. Modeled wet NO_3 deposition in January 2010 from the STRF model. Missing areas over the Rocky Mountains and the northern Midwest indicate a lack of measurements from OMI for the month of January.

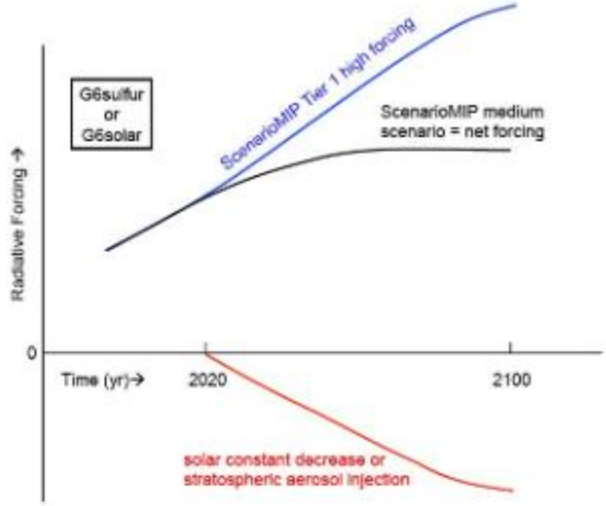

Figure S4.1. The trajectory of the G6Sulfur scenario. Copied from GeoMIP at Rutgers University (http://climate.envsci.rutgers.edu/geomip/geomip6.html).

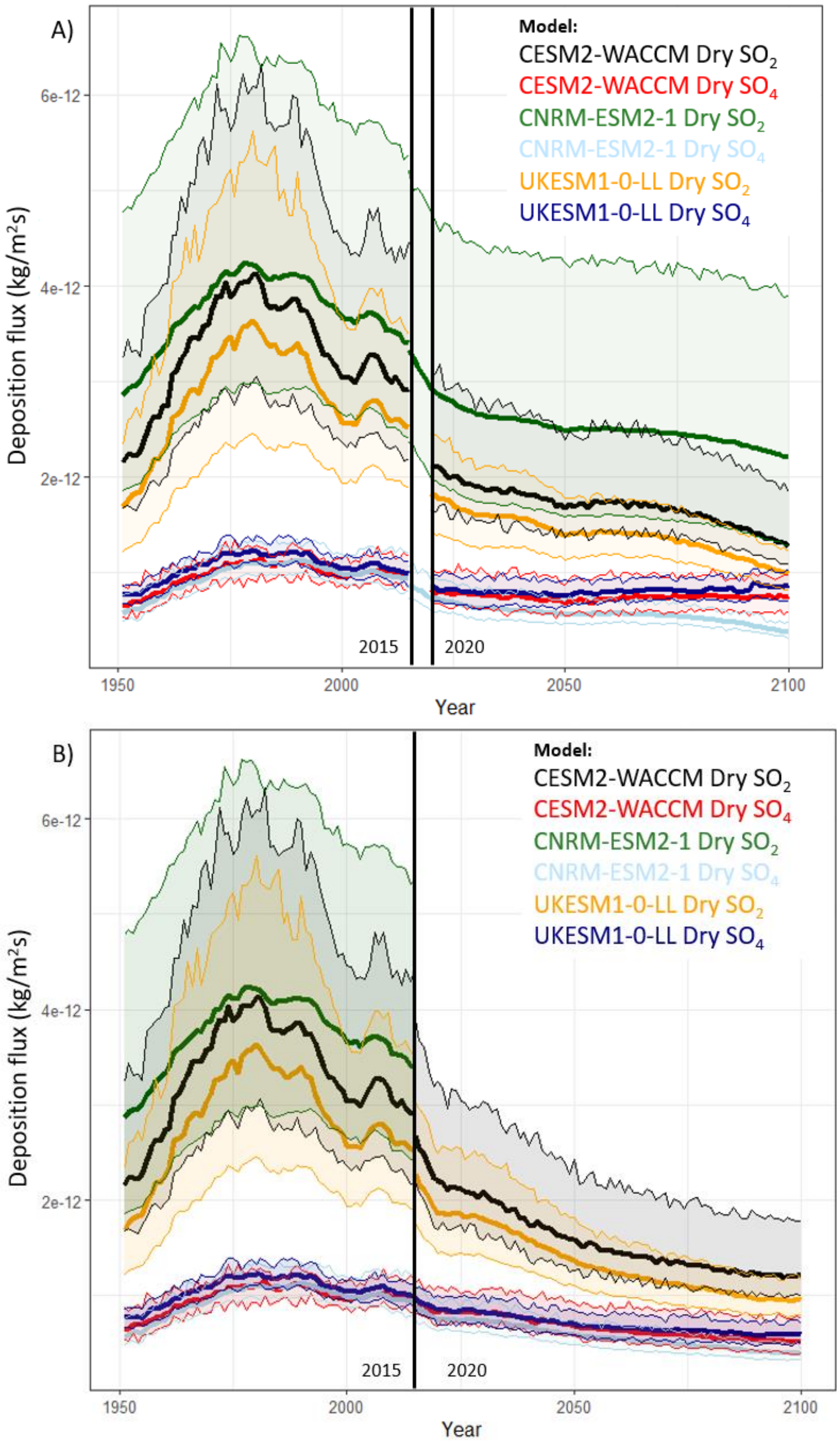

Figure S4.2. Historical and projected A) G6Sulfur, B) SSP2-4.5, and C) SSP5-8.5 dry SO2 and SO42- deposition flux.

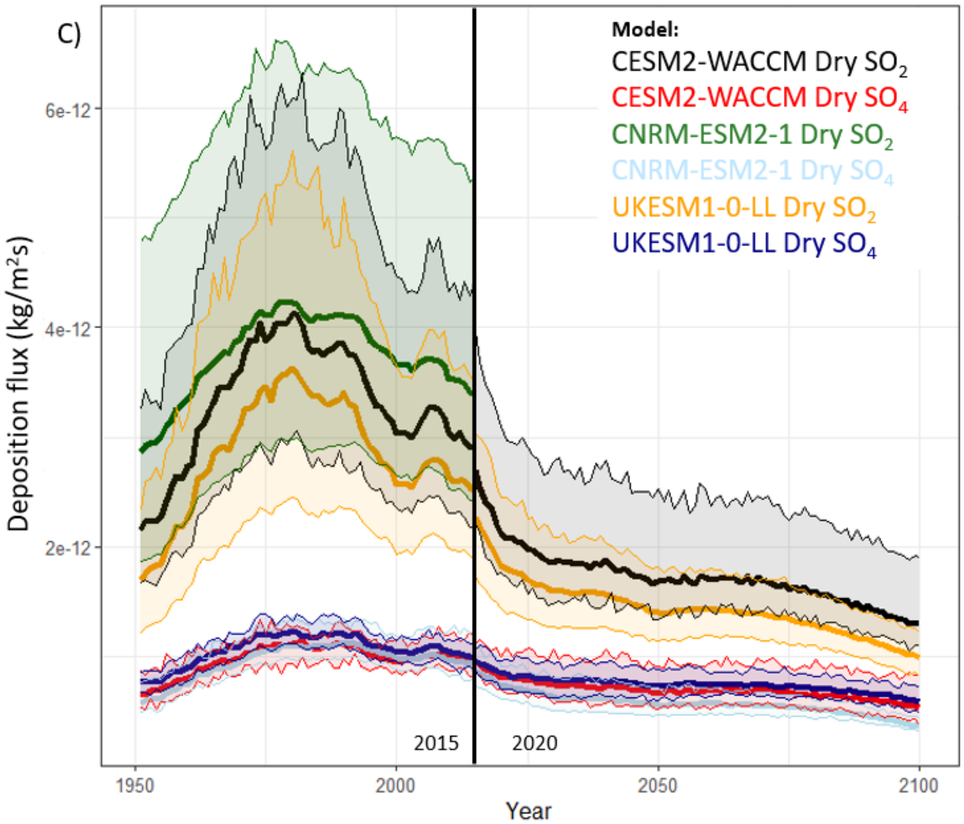

Figure S4.2 (Continued)

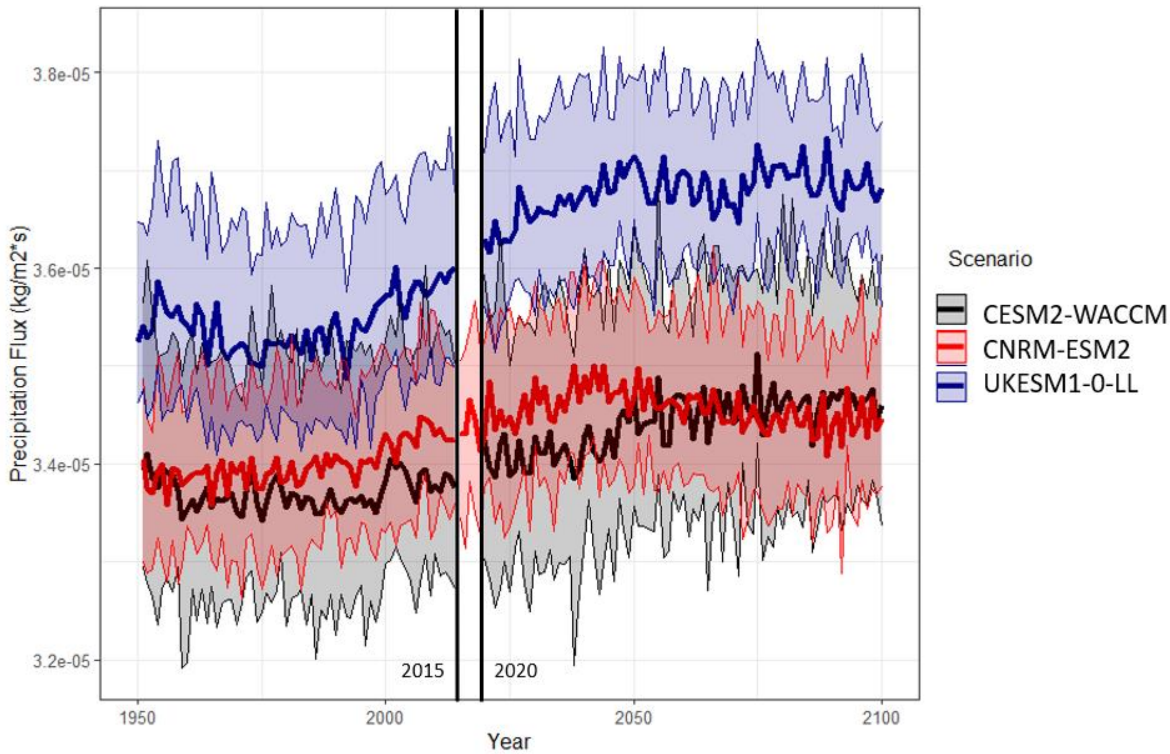

Figure S4.3. Precipitation flux from G6Sulfur GCM projections.

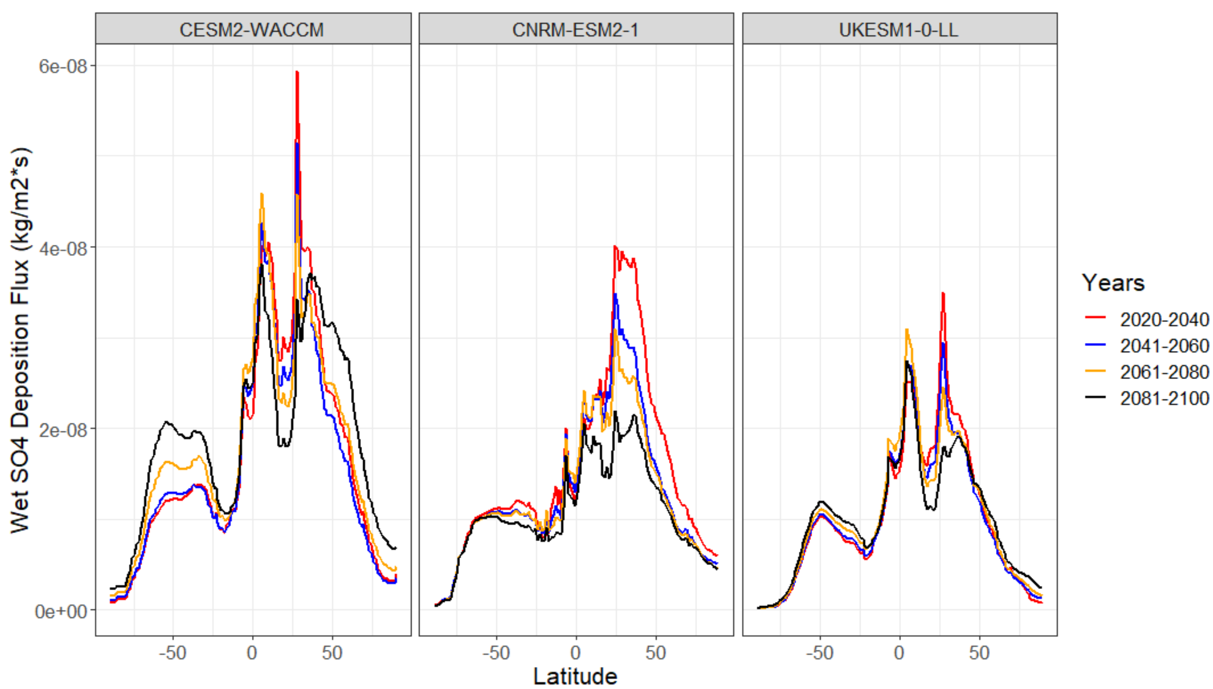

Figure S4.4. Projected total S deposition (wet SO2, wet SO42-, dry SO2, dry SO42-) from each G6Sulfur model averaged over 20-year slices.

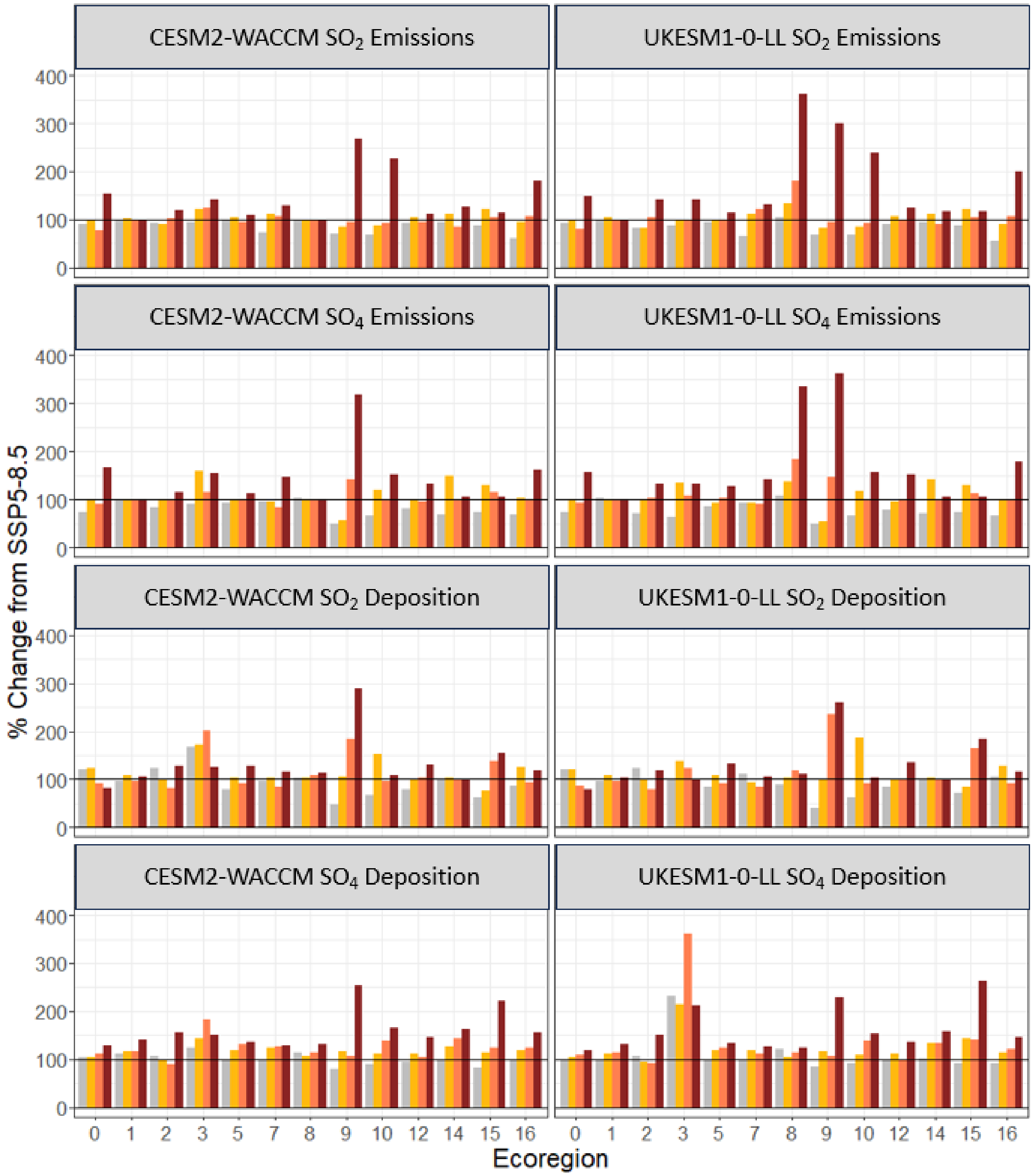

Figure S4.5. The percent change from SSP5-8.5 to G6Sulfur for CESM2-WACCM and UKESM1-0-LL SO2 and SO42- deposition by ecoregion, calculated as a difference in total deposition in Tg-S/yr.

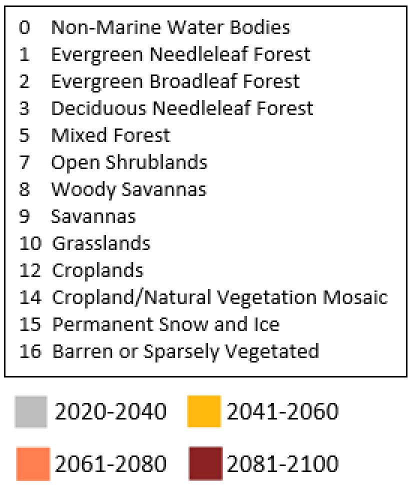

Figure S4.5 (Continued)

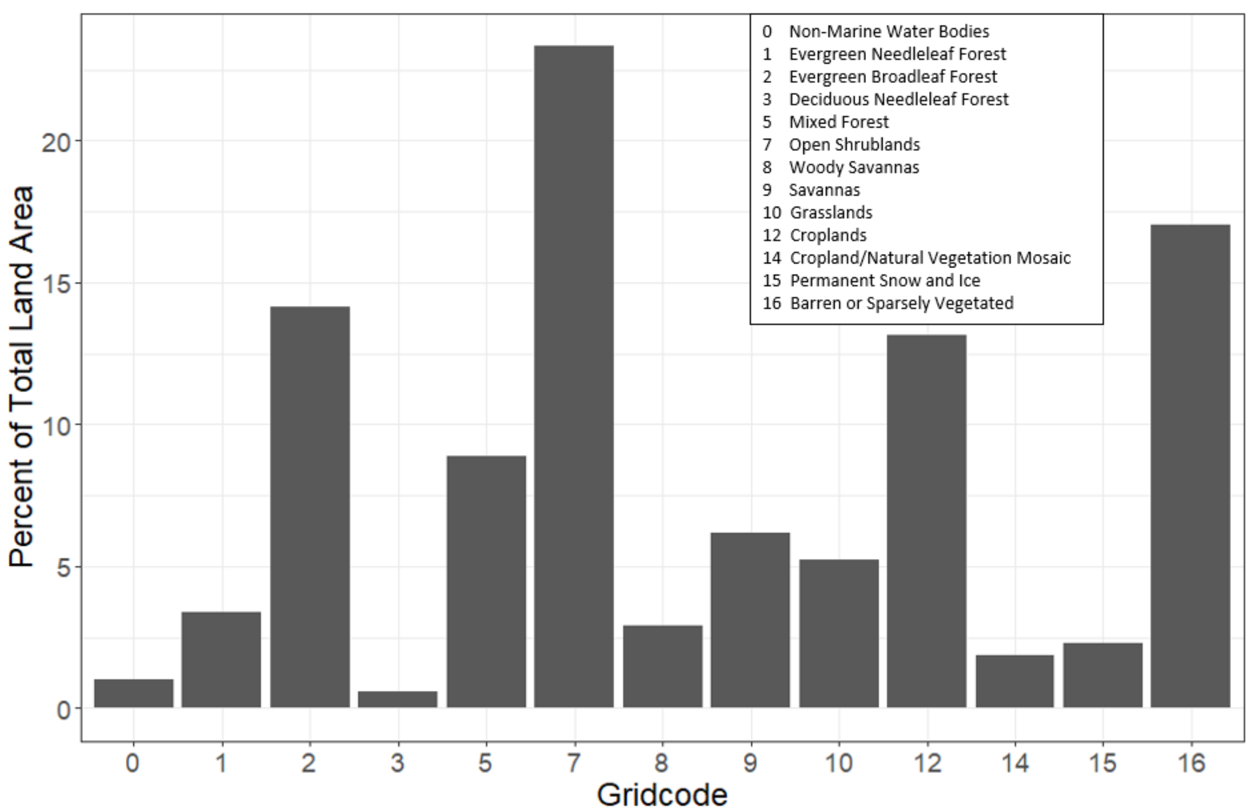

Figure S4.6. Percent of total land area by ecoregion for CESM2-WACCM.

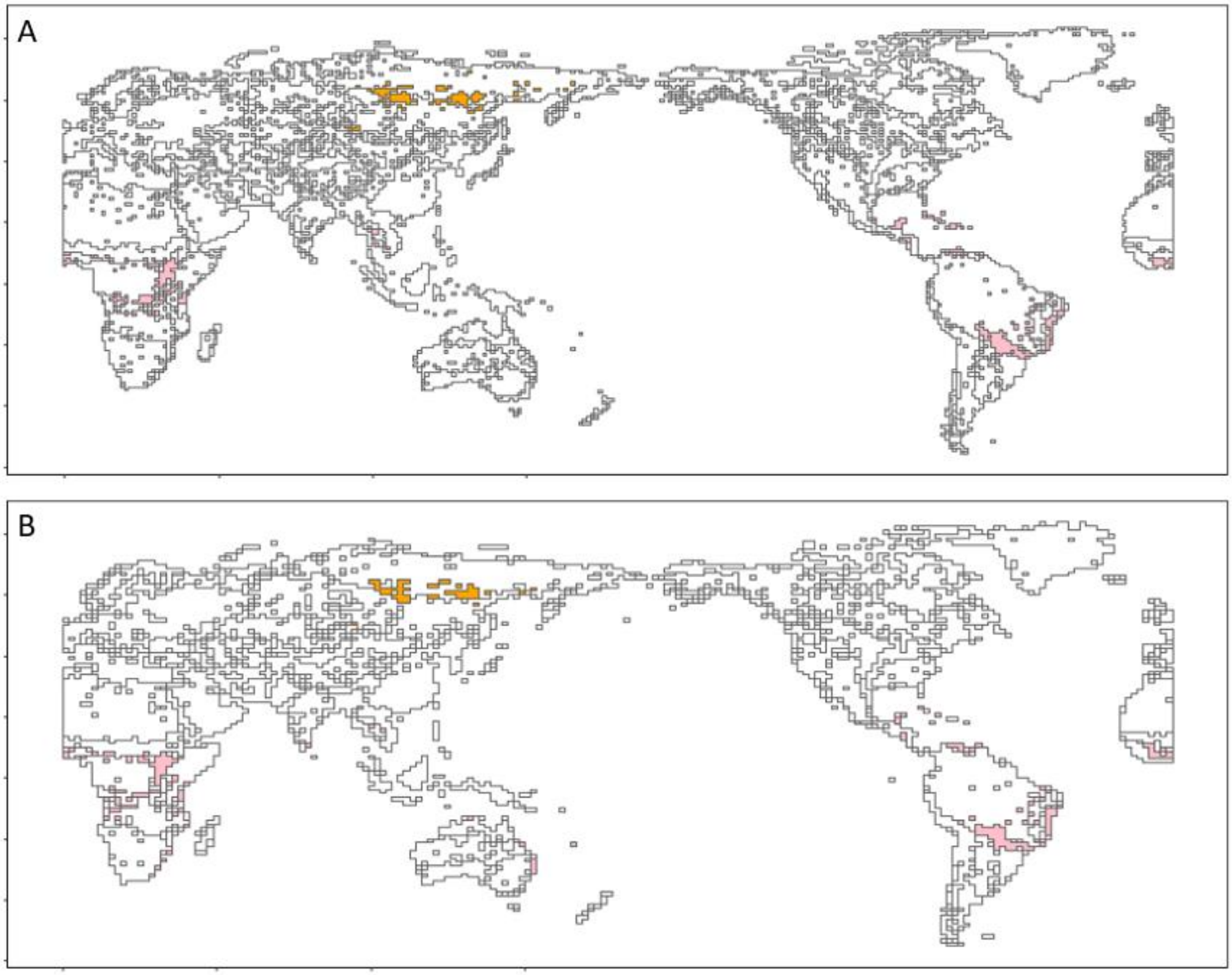

Figure S4.7 Ecoregion 3 (deciduous needleleaf forests) in orange and 8 in pink (woody savannas) according to the A) CESM-WACCM and B) UKESM1-0-LL IGBP ecoregion maps.

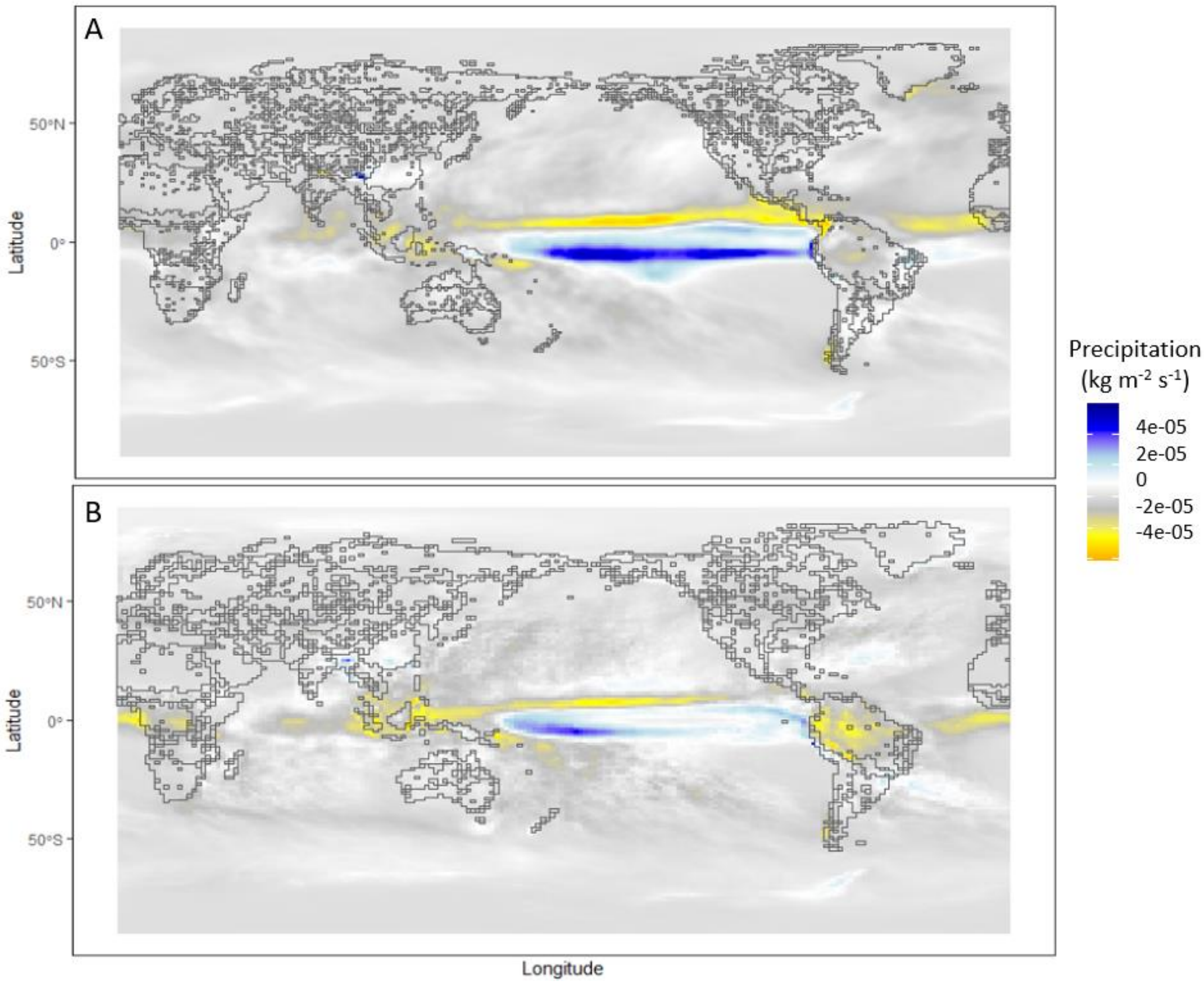

Figure S4.8 The difference in precipitation flux from 2020-2040 to 2080-2100 under G6 Sulfur according to the A) CESM-WACCM and B) UKESM1-0-LL IGBP models.

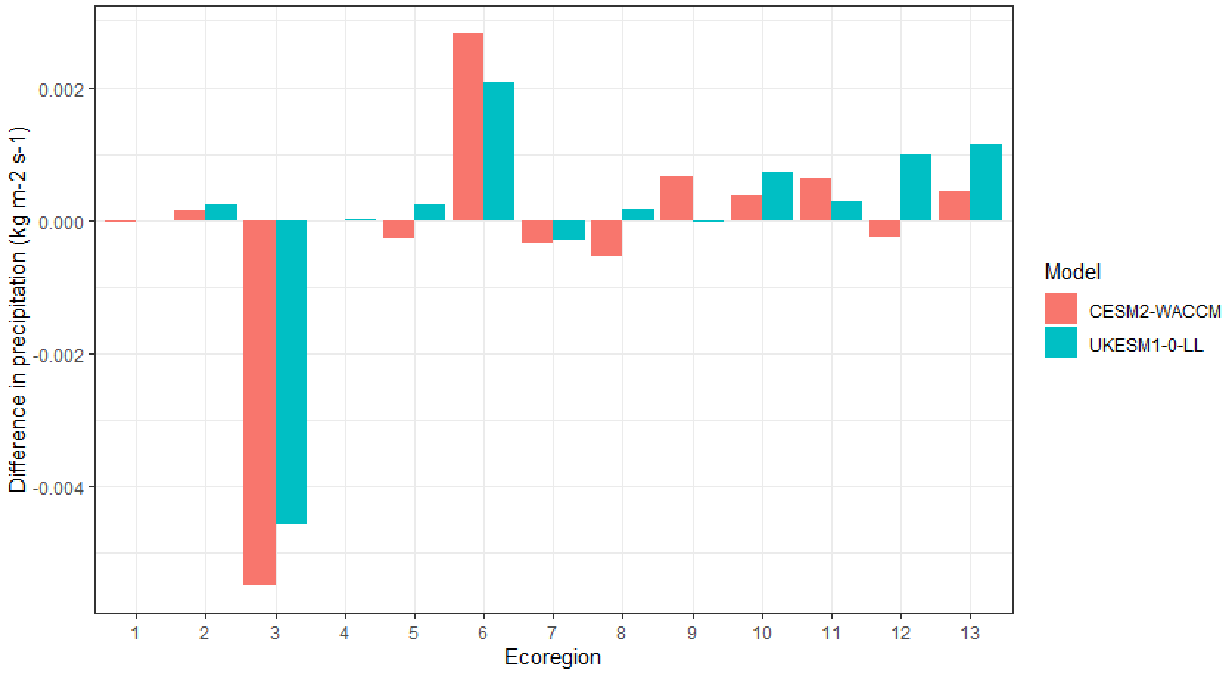

Figure S4.9. The difference in precipitation flux from 2020-2040 to 2080-2100 under G6 Sulfur according to the CESM-WACCM and UKESM1-0-LL models by IGBP ecoregion.

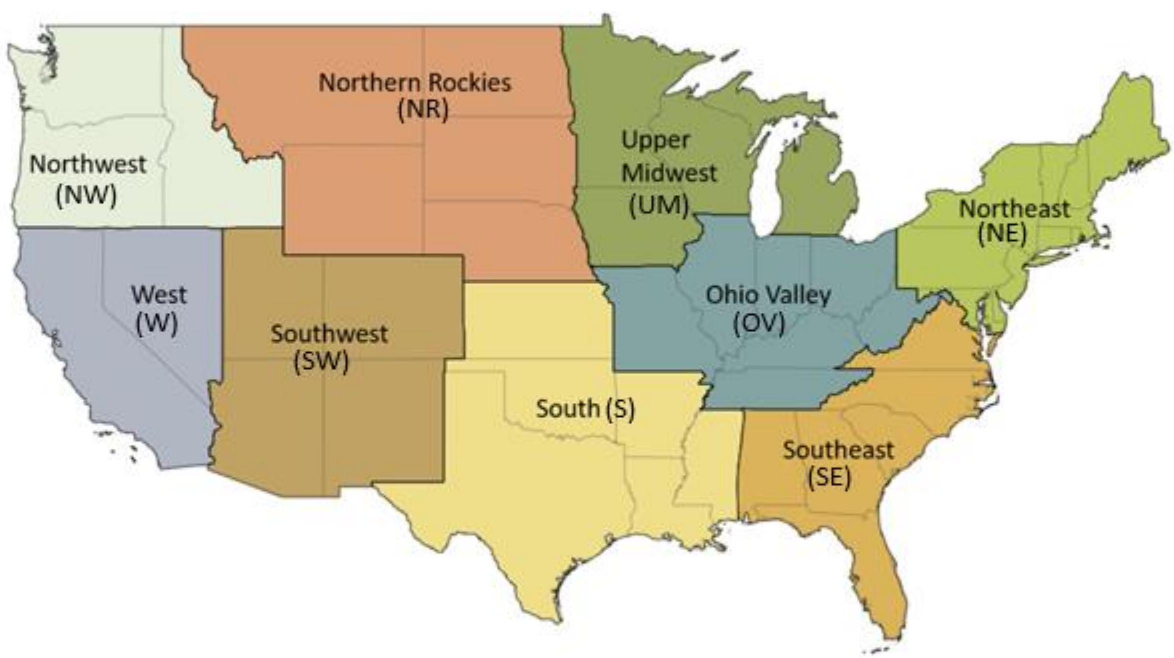

Figure S5.1. Study Area: The Conterminous US (CONUS). National Center for Environmental Information (NCEI) climate regions in the USA.

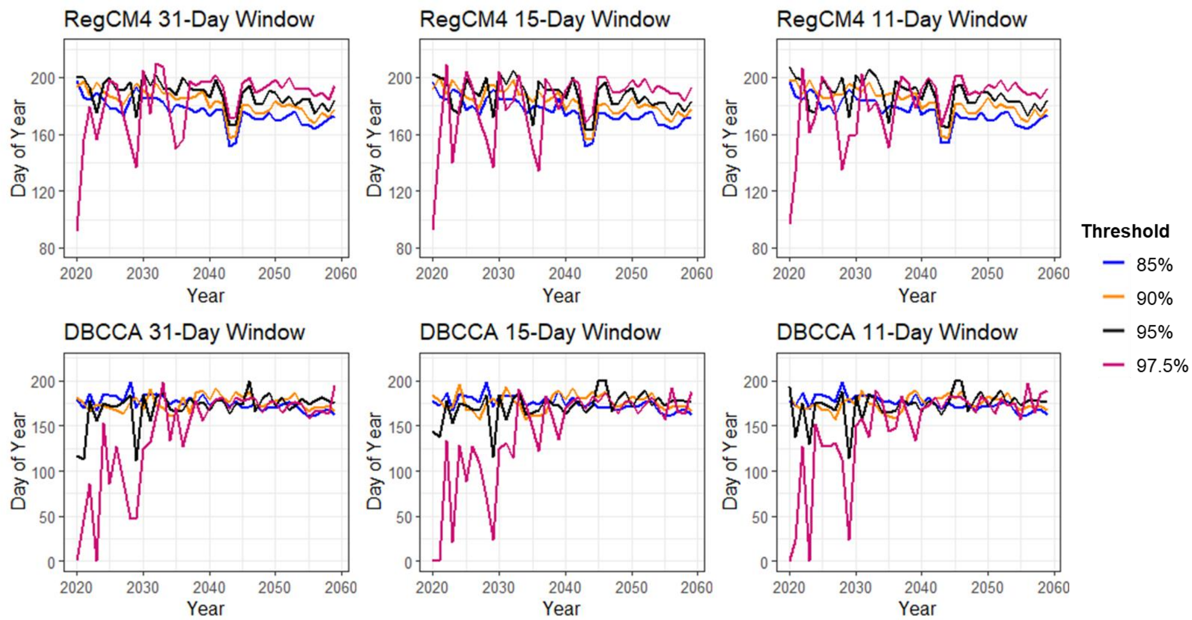

Figure S5.2. Predicted start day of the longest and hottest heat wave by threshold and window for each year in the US.

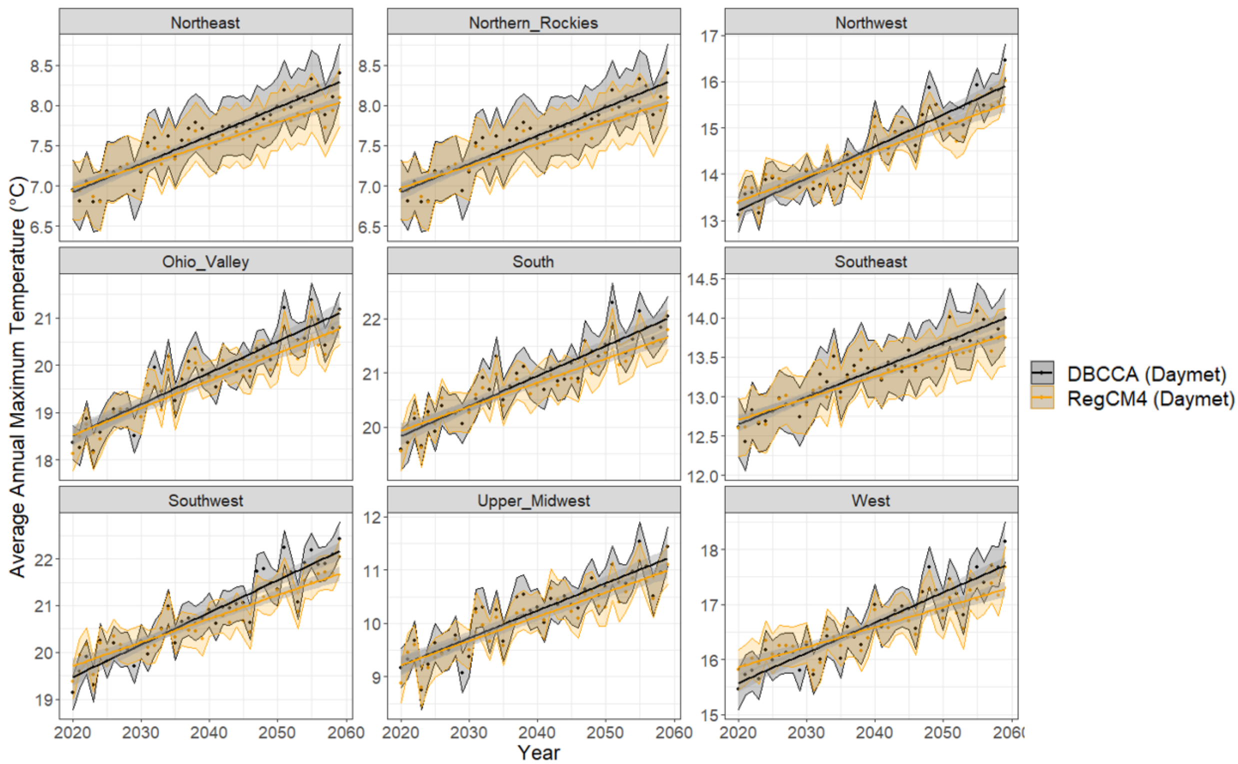

Figure S5.3. Average annual maximum temperature trends in the US. The daily maximum temperature is averaged by region for each year from 1980–2059. The y-axes vary by region. The shaded regions are the 95% confidence interval for the corresponding scenario. Daymet reference data were used for both the statistical (DBCCA) and dynamical (RegCM4) downscaling. The average annual minimum temperature is shown in Figure S5.4.

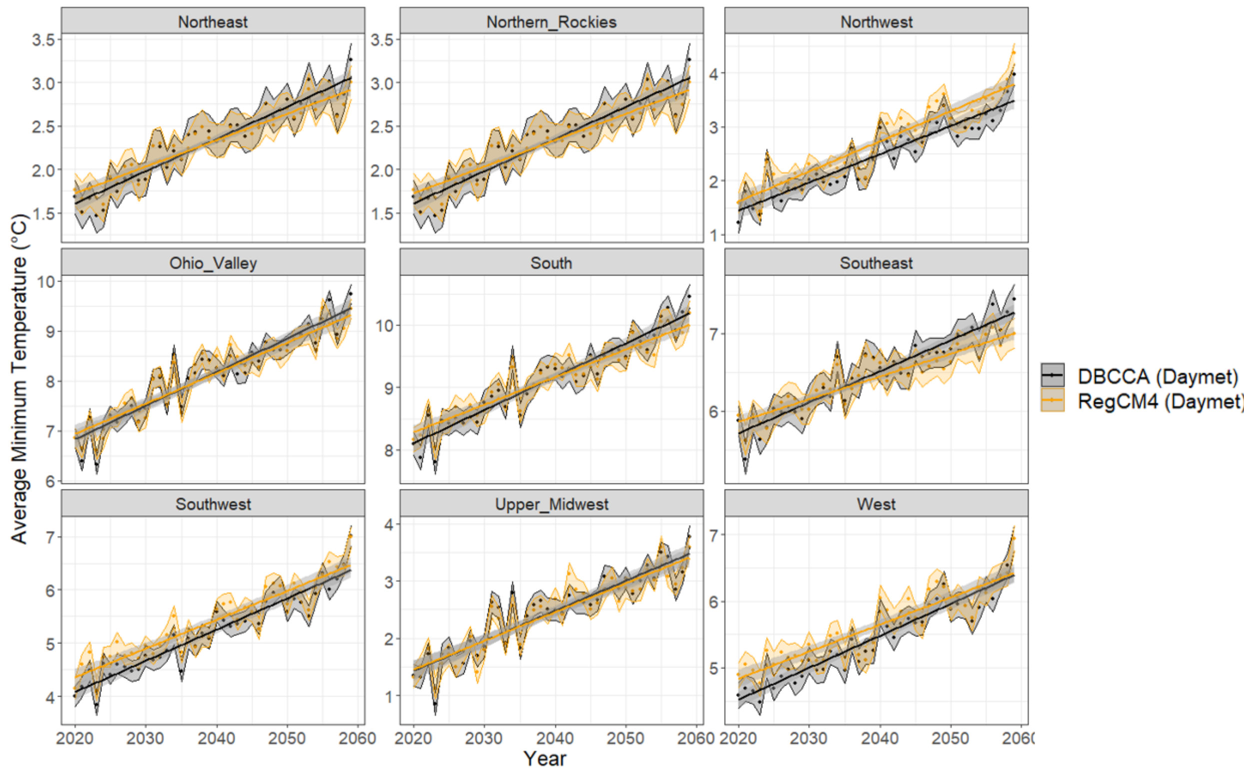

Figure S5.4. Average annual minimum temperature trends in the US. Daily minimum temperature is averaged by region for each year from 1980-2059. The y-axes vary by region. The shaded regions are the 95% confidence interval for the corresponding scenario. Daymet reference data were used for both the statistical (DBCCA) and dynamical (RegCM4) downscaling.

Table S5.1. The six CMIP6 global climate models used in this work (Rastogi et al., 2022).

GCM Name	Spatial Resolution	GCM Institute
ACCESS-CM2	144x192	The commonwealth Scientific and Industrial Research Organization, Australia
BCC-CSM2-MR	160x320	Beijing Climate Center
CNRM-ESM2-1	256x128	French Centre National de la Recherche Scientifique
MRI-ESM2-0	160x320	Meteorological Research Institute Japan
MPI-ESM1-2-HR	192x384	The German Climate Computing Center
NorESM2-MM	192x288	Multi-institutional, Coordinated Climate Research Project in Norway

Table S5.2. The 8 models and observations compared in Figure 5.2.

Dataset	Description	Source	Horizontal Grid Spacing
CMIP6-Raw	6-model ensemble (See Table S5.1)	World Climate Research Program	1º
Daymet	Daily surface meteorological summaries	Oak Ridge National Lab Distributed Active Archive Center	1 km
CMIP6-DBCCA	Statistical downscaling of CMIP6 with DBCCA and Daymet meteorology	Werner & Cannon, 2016	1/24º
NClimGrid	Monthly global climate observations	Global Historical Climatology Network	1/24º
PRISM	Daily climate estimates based on observations	PRISM Climate Group, Oregon State University	1/24º
CMIP6-RegCM4	Dynamical downscaling of CMIP6 with RegCM4 and Daymet meteorology	Giorgi et al. 2012	1/24º

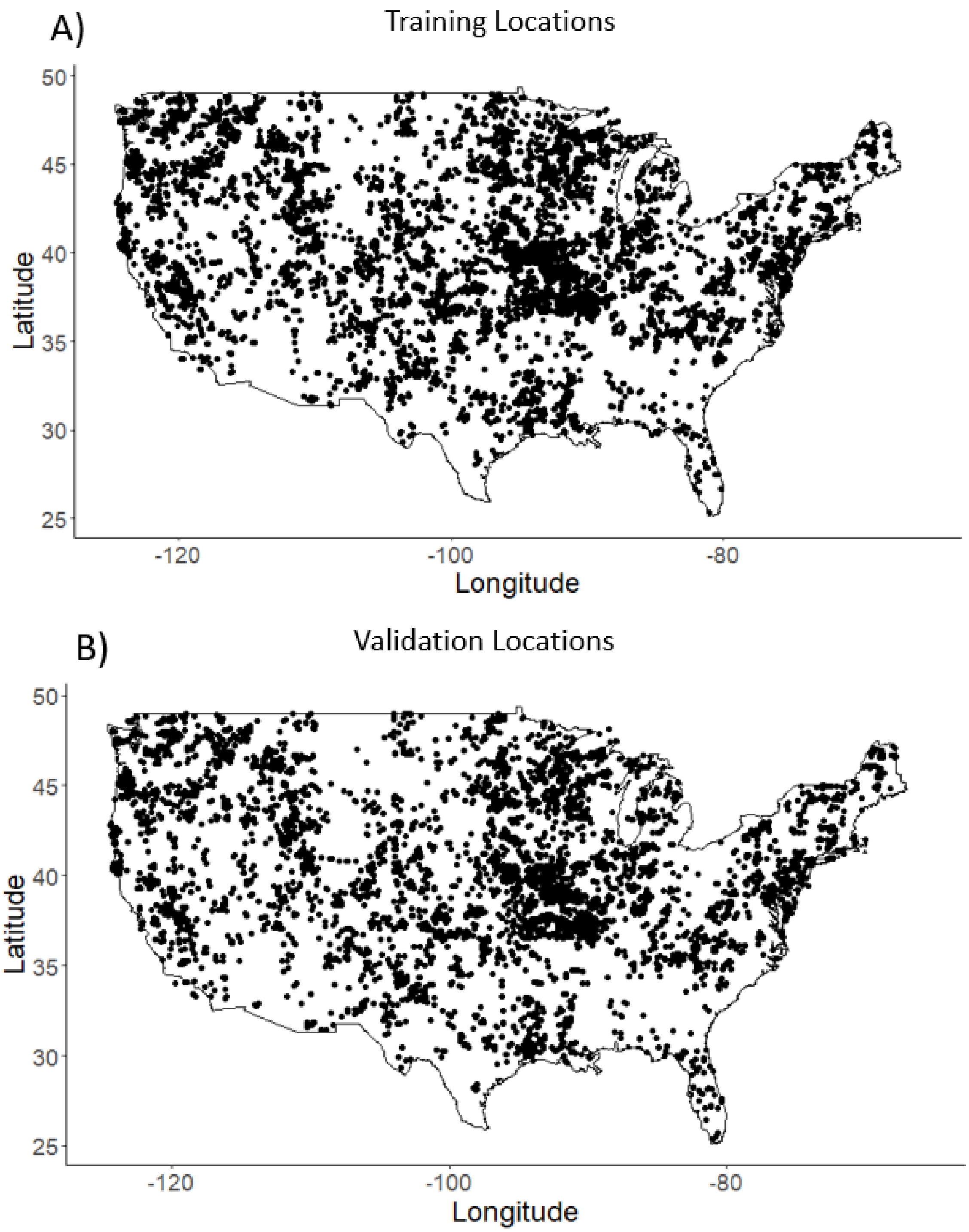

Figure S6.1 A) Locations of the training dataset (80%). B) Locations of the validation dataset (20%).

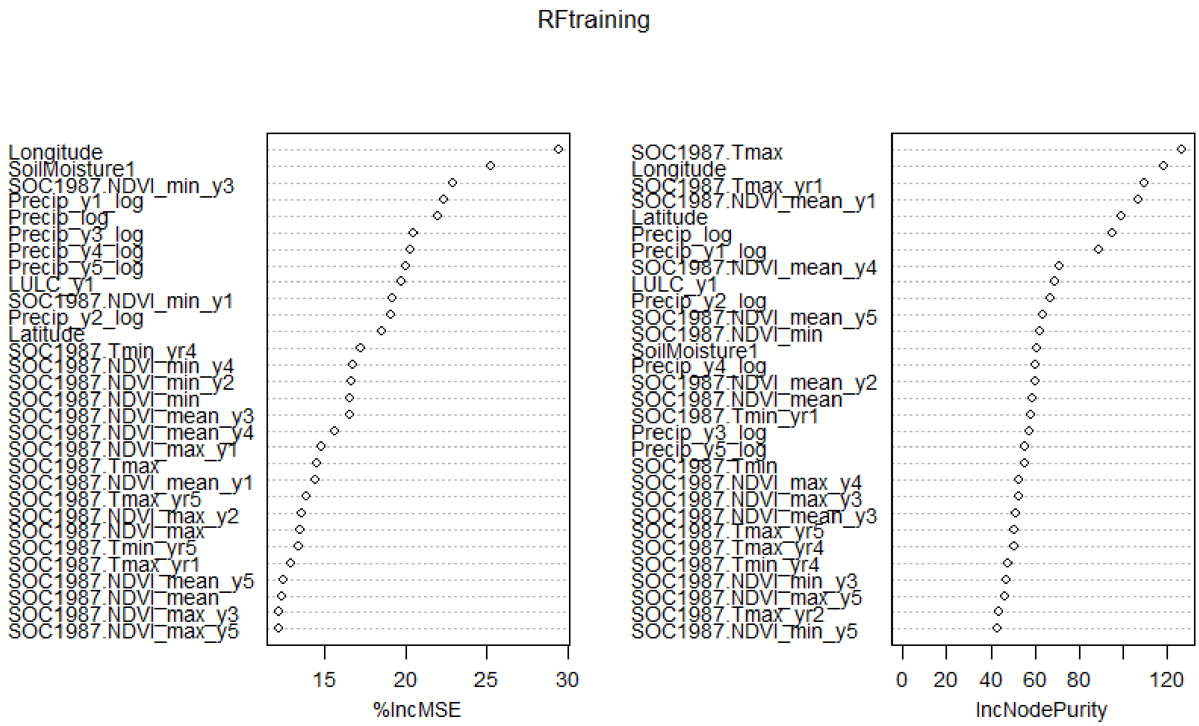

Figure S6.2. Variable importance in the random forest model.

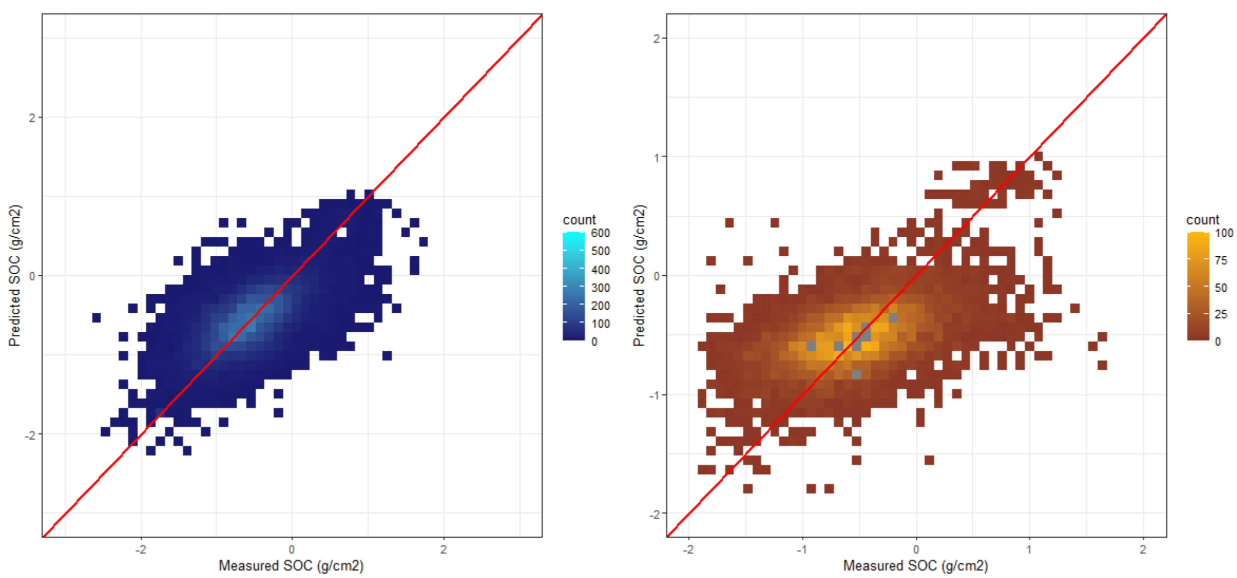

Figure S6.3. The fit of the random forest model.

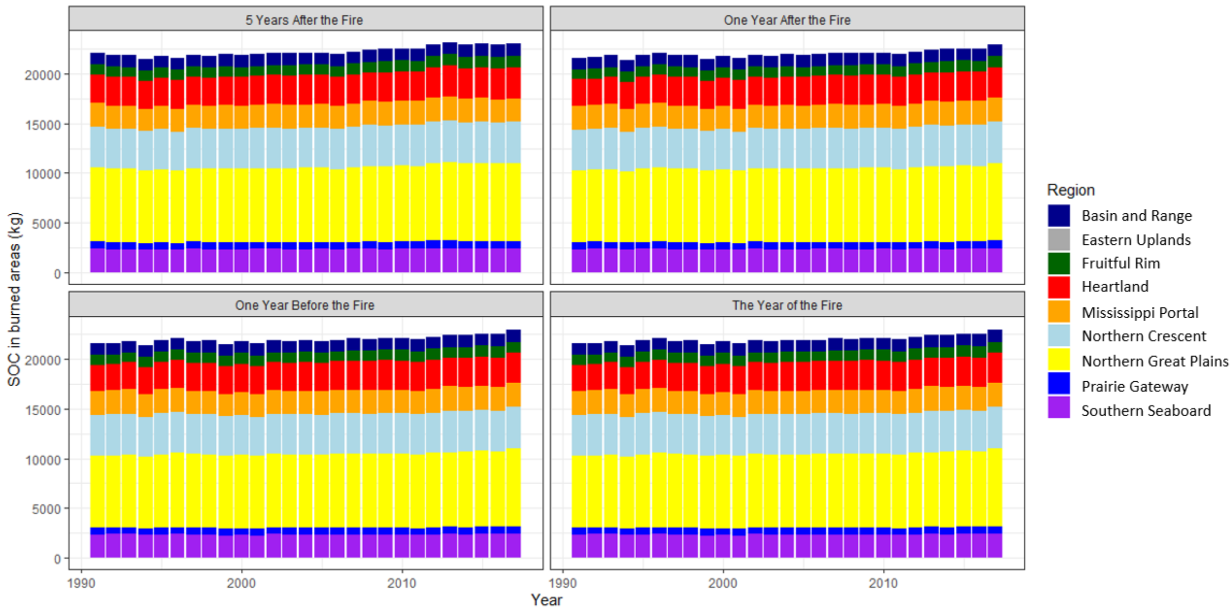

Figure S6.4. The change in annual SOC (kg/m2) in CONUS regions experiencing a wildfire, one year before the fire, one year after the fire, the year of the fire, and 5 years after the fire. Regions experiencing a wildfire were delineated using the USGS's Monitoring Trends in Burn Severity (MTBS) dataset of annual burned area boundaries.

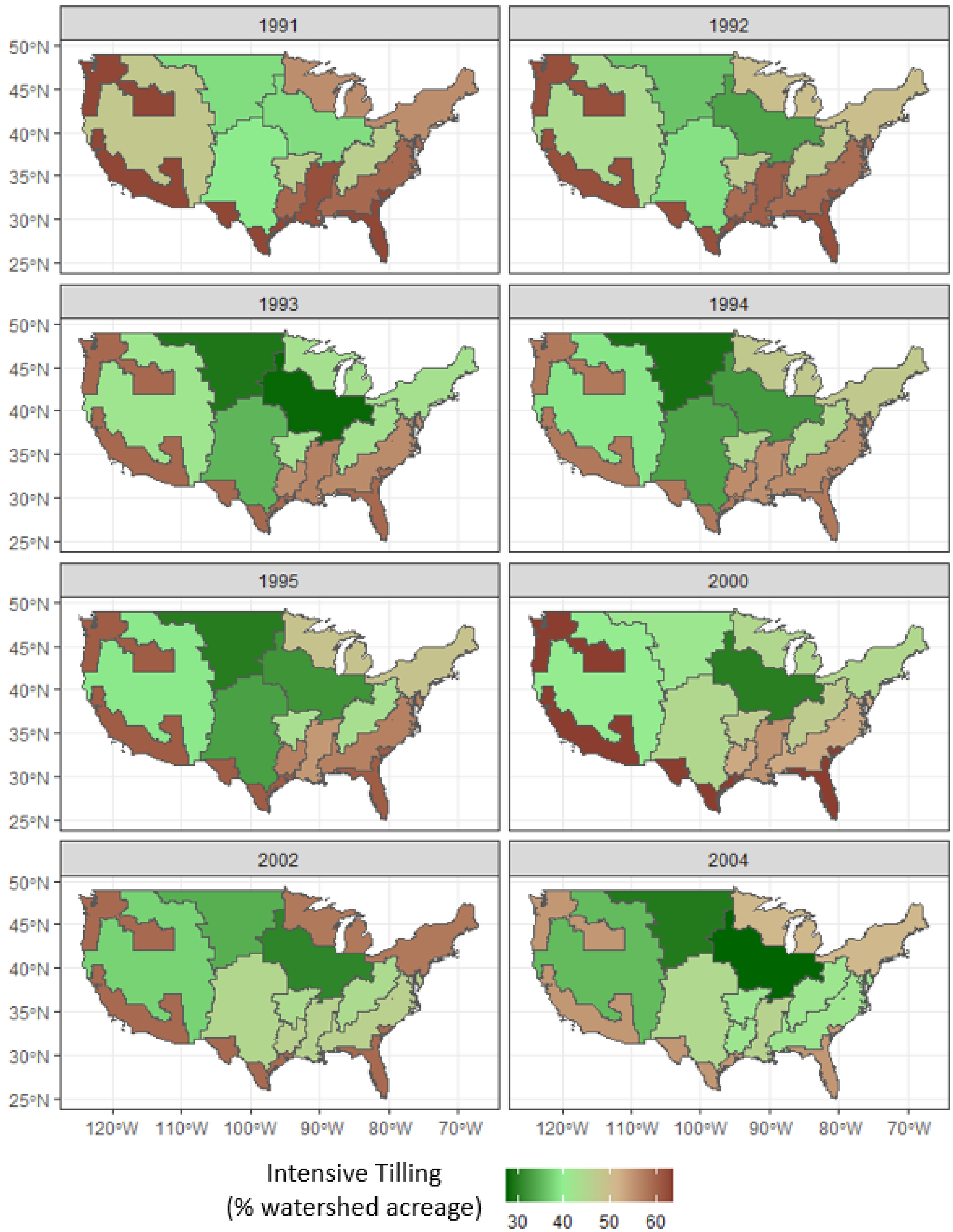

Figure S6.5. The percentage of farmland in each USDA farm resource region under intensive tilling for all crops for 8 select years. Regions not managed with intensive tilling are instead managed with either reduced tillage or conservation tillage which includes no-till, mulch, and ridge tillage.

Vita

Hannah Rubin was born in Knoxville, Tennessee but grew up in Bangor, Maine. She attended Dartmouth College in New Hampshire and graduated with a bachelor's degree in Earth Science and Geography in 2020. She wrote her senior honors thesis on improving remote sensing of lake water clarity with machine learning. She then pursued her interest in human-environment connections by beginning a PhD in Civil and Environmental Engineering at the University of Tennessee in Knoxville. Her research is on mapping climate change and air pollution with machine learning. She now works as an environmental modeler at a midsize environmental consulting firm in Vermont.